Universidad Nacional Autónoma de México

Centro de Nanociencias y Nanotecnología

Theoretical studies of ternary transition metal chalcogenides based on Density Functional Theory

T E S I S

que para obtener el título de:

Licenciado en Nanotecnología

P R E S E N T A :

Etienne Israel Palos

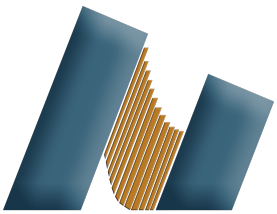

TUTOR

Dr. Jonathan Guerrero Sánchez
CNyN - UNAM, Ensenada. B.C., 2020

Theoretical Studies of Ternary Transition Metal Chalcogenides Based on Density Functional Theory

Hago constar que el trabajo que presento es de mi autoría y que todas las ideas, citas textuales, datos, ilustraciones, gráficas, etc. sacados de cualquier obra o debidas al trabajo de terceros, han sido debidamente identificados y citados en el cuerpo del texto y en la bibliografía y acepto que en caso de no respetar lo anterior puedo ser sujeto de sanciones universitarias.

Afirmo que el material presentado no viola ningún tipo de derechos de autor y me hago responsable de cualquier reclamo relacionado relacionado con ello.

Etienne Israel Palos

To Lucie, Aislynn and Mayela.

Acknowledgements

This thesis is the product of a collective continuous effort by a great deal of people who have demonstrated to care for me. They have proved to be genuinely interested in my success and well-being. Without their support, this work would not exist and I would have not survived in Ensenada. Let it be known that my gratitude towards each and every one of you cannot be expressed writing. I will forever be in debt for all that my family, friends, mentors and life itself have given me.

First off, I would like to begin by acknowledging Jonathan Guerrero Sánchez, my academic advisor, collaborator and friend that I could have asked for. Thank you for mentoring me and at the same time allowing me to explore my interests and lead my research projects in such a bold and independent manner. I am a stubborn pupil, but it means quite a lot to me that you encourage me to dive deeper into electronic structure theory and predict the physical properties of increasingly complex materials. This being said, thank you for not scolding me for spending more time than necessary on my numerical "experiments". Moreover, thank you for celebrating with me not only my academic successes, but my personal achievements as well. It doesn't go unnoticed that before we discuss science, you take the time to always make sure Lucie and Aislynn are alright and you never miss a chance to offer your hand if anything is needed. Without your support, I would not have been able to acquire my current knowledge and skills in materials modeling, developed the ideas presented in this thesis, and have presented some of our work at the national meeting of the American Chemical Society (ACS) last year. As a consequence, I would not be preparing my bags to embark on a doctoral program in Theoretical and Computational Chemistry at the very university where Density Functional Theory was born!

Next, I want to express my gratitude toward Donald H. Galván, who took a chance on me when I was only a sophomore, who had failed classical mechanics, but was very curious about quantum chemistry. Professor Galván, you took time out of your busiest days, to share inspir-

ing anecdotes about theoretical molecular physics, solid-state physics and computational quantum chemistry. You witnessed the birth of computational materials science. You taught me why their differences shouldn't matter or whether you were educated as a physicist or chemist (or neither as is my case), and what the theory and computation can teach us about our material world. You encouraged me to dream big and aspire to become a key player in theoretical chemistry, and to be bold like the great Roald Hoffmann. You lent me your books on molecular and solid-state physics, taught me fundamental quantum chemistry one-on-one and guided me through my first publication. I will forever be grateful for your teachings.

This brings me to Armando Reyes Serrato. You have believed in me since I first enrolled at UNAM. Above my academic successes or failures, you have gone out of your way to support me in my studies. I will never forget everything you have done for me, and to say that without your support I would not be graduating is an understatement. Quite frankly, without your continuous efforts, I would not have been able to continue obtaining a college education after my first semester. Last year, you once again demonstrated your confidence in my potential and work and funded my trip to the ACS meeting. That meeting changed my life and the life of my family forever. When we first met, five years ago, you asked me: "so you're the kid who wants to theory?"

Gabriel Alonso Nuñez, the experimentalist who bet on me as a theoretician. For two years, you supported me through a SNI III Research Assistant CONACyT scholarship and gave me the liberty to focus on the computational modeling and prediction of materials that could potentially be interesting in your field. Here, I disclose that without your support, surviving in Ensenada these past two years would have been impossible. Thanks to you believing in my ideas, I was able to keep a roof over my head and graduate.

I want to thank the professors who were always there for me, to discuss science or talk about the mysteries of life and share a laugh. In this sense, I am especially grateful to Catalina López Bastidas and Carlos Iván Ochoa Guerrero. Aside from discussing solid state theory, parenthood and drinking coffee, Catalina and Carlos have been consistent advocates for me.

To Joel Yuen-Zhou, for being my scientific role model and for supporting me to pursue a graduate degree in theoretical and computational chemistry. To Adrian Jinich and Miguel Magaña Fuentes for inspiring me to become a scientist, and for mentoring me from early on, supporting me to kick-start my way into theoretical chemistry.

Every achievement and dream of mine belongs to each person who has contributed to seeing that

I make it here. At this point, I thank Sra. Angélica Chimal and Don Abel Zaldivar for providing me with a roof over my head when my pockets were empty. To Jesús Ruiz Mata, a Mexican American mathematician who sponsored my return to UNAM in 2016. It will soon be my turn to help a student facing similar circumstances, and I looking forward to it! I thank Armando Reyes Serrato, Arturo Gamietea and Matematiké A.C. for letting me work as a tutor for three semesters in order to support myself. I also want to thank Laura Viana Castrillón for everything she has done for me. Without her support, survival would have also been a bit more difficult. Also, I want to thank her for a wonderful course in Statistical Physics.

Un saludito especial to all the homies out there. I want to thank Genaro Soto-Valle Angulo, Daniel Maldonado López, Axel Gaona Carranza, Luis Ricardo Rodríguez Marino, Christian López Ángeles and Alejandro Noguerón Arámburu, and everybody else for their support and the good times. To all the great people I met at CNyN-UNAM, CICESE, and *CHIZA*. Saludos al Mochis, Chaneli, April-May-June and Moño.

Axel, thank you for literally becoming a part of this journey into the world of materials theory.

Danny, thank you giving me shelter in my last semester, for listening to my melt-downs and helping me see the bigger picture when I lose my mind over the *nano*-details, and for getting me out of work-mode on occasions to keep me sane. Also, thanks for the programming + death metal sessions. Most importantly, thank you for always giving me that extra push!

Alejandro, thank you for believing in me from early on. I felt lost in college at the beginning but you always pushed me to keep moving forward and to stay true to my convictions. Moreover, you always encouraged me to work as hard as I possibly could to become a true theorist. Thank you for all the stimulating conversations about scientific research and research ethics, within and beyond Mexico.

I want to thank my *hermano, carnal and compadre*, Óscar Andrés Ramírez Ramírez (OARR), for showing me that I was not alone at UNAM. I thank OARR for every conversation, for not one was dull. For the countless hours of watching psychological dramas (not thrillers), true crime documentaries, rap battles in English, Spanish, or Spanglish, ritualistic trips to Carls Jr., El Trailero or with "el Sammy" for some tacos, LaTeX all-nighters, unhealthy amounts of coffee or cup ramen, and for making every moment memorable. I am convinced that our friendship revived and strengthened our confidence in ourselves and each other, as scientists and well-intended human beings.

Lastly, I want to thank my *familia* on both sides of the US-MX border. To my Nana Mina, my

Tio Manuel and Tia Rosa, Tia Tere and Tio Víctor, and the *primos*. Also, thanks to my abuelito Oscar.

To Oscar and Aaron, my brothers and dearest fiends. Though thick and thin, my unconditional homies. Together, we're *sticks and stones*. To my father, Oscar Ernesto Rubí, who taught me everything I know about life. If you want something, or care about something, work hard and work tirelessly for it. To my mother, Mayela Guadalupe González, who has showed me that true love is worthy of any sacrifice.

I want to thank my daughter, Lucie Anne Palos, and her mother, Aislynn Elizabeth Silva Reyna, for giving me the strength to complete this thesis. Your love fuels everything I do.

Technical Acknowledgements

The projects presented in this thesis, due to their nature and scope, are collaborative. Therefore, I acknowledge the following researchers for their participation, guidance and/or comments along the way: Axel Gaona Carranza, Armando Reyes Serrato, Gabriel Alonso Nuñez, and my advisor.

The research was partially funded by DGAPA-UNAM projects IN101019, IA100920, and Conacyt grant A1-S-9070 of the Call of Proposals for Basic Scientific Research 2017-2018. The DFT computations were carried out in the DGCTIC-UNAM Supercomputing Center, under projects LANCAD-UNAM-DGTIC-051 and LANCAD-UNAM-DGTIC368. Additionally, JGS acknowledges THUBAT KAAL IPICYT supercomputing center for computational resources. The authors would like to thank A. Rodriguez Guerrero for technical assistance and useful discussions.

Chapter 3 in full is a reprint of the publication titled *"Modeling the ternary chalcogenide Na_2MoSe_4 from first-principles"*, published in *Journal of Physics: Condensed Matter*. The article may be cited as "Palos et al 2020 J. Phys.: Condens. Matter 10.10881364-648X/abaf91". An open-access version of the manuscript has been made available in the form of a preprint on ChemRxiv.

The author of this thesis is the principal investigator of this project and the first and corresponding author of the publication. Chapters 4 and 5 contain material to be published in two independent articles, currently in preparation. EIP is the principal and corresponding author in these.

Abstract

Understanding and exploiting the properties of interacting quantum particles is central to condensed matter physics, physical chemistry and materials science. Computational quantum mechanics has enabled the design of technologically relevant materials from a minimal set of parameters, such as the number of quantum particles conforming a given system and their positions. One methodology in particular, Kohn-Sham Density Functional Theory (DFT), has become the work-horse of theoreticians for its accuracy in describing the ground state properties of systems. In this thesis, we present a series of computational electronic structure studies in which we discuss the ground state properties of sixteen different compounds within the context of solid-state physics. Particularly, we employ DFT to the modeling of ternary transition metal chalcogenides, a class of materials receiving an increasing amount of attention within the physics, chemistry and materials science communities for their high stability and properties suitable for solid-state devices.

We determine the equilibrium structure and electronic properties of Na_2MoSe_4. By combining DFT with a crystal structure prediction method, we identify the stable phase of the selenide, demonstrating that it has a simple orthorhombic (oP) lattice. Moreover, we show that it is a direct bandgap semiconductor with potential applications in high-speed optoelectronics.

Next, we extend our investigation to a family of alkali-ion transition metal chalcogenides. We theoretically investigate twelve systems with with oP symmetry and formula A_2MX_4, where A = K^+, Rb^+, Cs^+ ; M = Mo, W and X = S^-, Se^-. We model the band structures of nine experimentally known compounds, and predict the ground state properties of three new materials. We show that A_2MX_4 is a family of direct bandgap semiconductors with a range of bandgap values that show potential for applications in optoelectronics and photovoltaics.

Finally, we discuss the physical properties of three new two-dimensional materials and their potential for quantum device applications. Using first-principles calculations, we model three ternary

niobium tellurides $NbMTe_2$, where M = Fe, Co, Ni, as monolayers. We show that a monolayer may be obtained for each material via exfoliation, and that they are energetically stable. Furthermore, we demonstrate that $NbFeTe_2$ is predicted to be robustly ferromagnetic with a Curie temperature of 205 K. The band structure of non-magnetic $NbNiTe_2$ shows an interesting anti-crossing exactly at the Fermi level, making it a potential topological material. Overall, our results classify these 2D ternary niobium tellurides as true quantum materials with potential applications in next-generation devices, motivating future theoretical and experimental studies.

The chemistry of transition metal chalcogenides provides a platform to rationalize compounds with diverse and complex electronic structures. Here, a first-principles treatment was applied to the investigation of sixteen different compounds. Of the sixteen materials discussed, four are predicted bulk semiconductors, nine are known, and three are predicted 2D quantum materials. To the best of our knowledge, these are the first theoretical reports of the ground state properties of all of these systems.

Resumen

El poder comprender y explotar las propiedades de las partículas cuánticas que interactúan es fundamental para la física de la materia condensada, la química física y la ciencia de los materiales. La mecánica cuántica computacional ha facilitado el diseño de materiales tecnológicamente relevantes a partir de un conjunto mínimo de parámetros, como el número de partículas cuánticas que conforman un sistema dado y sus posiciones. Una metodología en particular, la Teoría del Funcional de la Densidad de Kohn-Sham (DFT), se ha convertido en el caballo de batalla de los teóricos por su precisión en la descripción de las propiedades del estado fundamental de los sistemas. En esta tesis, presentamos una serie de estudios computacionales de estructura electrónica en los que discutimos las propiedades del estado fundamental de dieciséis compuestos diferentes dentro del contexto de la física del estado sólido. En particular, empleamos DFT para el modelado de calcogenuros de metales de transición ternarios, una clase de materiales que reciben una atención cada vez mayor dentro de las comunidades de física, química y ciencia de los materiales por su alta estabilidad y propiedades adecuadas para dispositivos de estado sólido.

Determinamos la estructura de equilibrio y las propiedades electrónicas de Na_2MoSe_4 combinando DFT con un método de predicción de la estructura cristalina. Determinamos la fase estable del seleniuro, demostrando que tiene una red ortorrómbica simple (oP). Además, mostramos que es un semiconductor de banda prohibida directa con aplicaciones potenciales en optoelectrónica de alta velocidad.

A continuación, ampliamos nuestra investigación a una familia de calcogenuros de metales de transición de iones alcalinos. Teóricamente investigamos doce sistemas con simetría oP y fórmula A_2MX_4, donde A = K^+, Rb^+, Cs^+; M = Mo, W y X = S^-, Se^-. Modelamos las estructuras de bandas de nueve compuestos conocidos experimentalmente y predecimos las propiedades del estado fundamental de tres nuevos materiales. Mostramos que A_2MX_4 es una familia de semiconductores

de banda prohibida directa con un rango de valores de banda prohibida que muestran potencial para aplicaciones en optoelectrónica y fotovoltaica.

Finalmente, discutimos las propiedades físicas de tres nuevos materiales bidimensionales y su potencial para aplicaciones en dispositivos espintrónicos. Usando cálculos de primeros principios, modelamos tres teluros de niobio ternarios 2D $NbMTe_2$, donde M = Fe, Co, Ni. Demostramos que se puede obtener una monocapa para cada material mediante exfoliación, y que son energéticamente estables. Además, se predice que $NbFeTe_2$ será robustamente ferromagnético con una temperatura de Curie de 205 K. La estructura de bandas de $NbNiTe_2$ no magnético muestra un anti-cruce interesante exactamente en el nivel de Fermi, lo que lo hace un material topológico potencial. En general, nuestros resultados clasifican estos telururos de niobio ternarios 2D como verdaderos materiales cuánticos con aplicaciones potenciales en dispositivos de próxima generación, lo que motiva futuros estudios teóricos y experimentales.

La química de los calcogenuros de metales de transición proporciona una plataforma para racionalizar compuestos con estructuras electrónicas diversas y complejas. Aquí, se aplicó un tratamiento *ab-initio* a la investigación de dieciséis compuestos. De estos, cuatro son semiconductores, nueve son conocidos y tres son materiales cuánticos 2D predichos. Hasta donde sabemos, estos son los primeros informes teóricos de las propiedades del estado fundamental de todos estos sistemas.

Contents

List of Figures

List of Tables

Chapter 1

Introduction

"Knowing without seeing is at the heart of Chemistry"

- Roald Hoffmann

Quantum mechanics is undeniably the responsible for the reconciliation of physics and chemistry in the XX century. The theory provides a complete guide to understand the fundamental properties of quantum systems. Thus, the Shrödinger equation can yield useful information about the fundamental properties of quantum particles, atoms, molecules, and without hyperbole, everything in the material world. Alas, there is no way to solve this equation analytically for systems with complexity higher than that of a Hydrogen atom. The theory was developed, but it's limitations quickly became clear.

Paul Adrien Maurice Dirac, one of the fathers of quantum mechanics and a visionaries of the XX century, had foreseen the course that Quantum Mechanics would undertake; developing methods to numerically approximate the Schrödinger equation for complex systems. He stated this explicitly in his seminal work "*Quantum mechanics of many-electron systems*" [**1**]. We quote:

"The general theory of quantum mechanics is now almost complete, the imperfections that still remain being in connection with the exact fitting in of the theory with relativity ideas. These give

rise to difficulties only when high-speed particles are involved, and are therefore of no importance in the consideration of atomic and molecular structure and ordinary chemical reactions, in which it is, indeed, usually sufficiently accurate if one neglects relativity variation of mass with velocity and assumes only Coulomb forces between the various electrons and atomic nuclei.The underlying physical laws necessary for the mathematical theory of a large part of physics and the whole of chemistry are thus completely known, and the difficulty is only that the exact application of these laws leads to equations much too complicated to be soluble. It therefore becomes desirable that approximate practical methods of applying quantum mechanics should be developed, which can lead to an explanation of the main features of complex atomic systems without too much computation."

-P.A.M. Dirac (1929)

Today, these approximate and practical methods are used by scientists to study atomic systems, molecules, materials and complex chemical processes. The development and practice of these methods is what we refer here as Computational Quantum Mechanics (CQM).

The practical common ground for physics and chemistry is found in condensed phases, where the solid state is the protagonist. There, the two sciences join forces on a mission to unravel the microscopic nature of materials and how they provide an understanding of their fundamental macroscopic properties. By microscopic nature, what is referred to is the physical phenomena that occurs within the atomic and molecular length-scales, governed of course by the laws of quantum mechanics. Given the appropriate conditions, atoms, molecules and ions interact in such a way that they form periodic arrangements through space while their physics and chemistry remain invariant. In solid state physics, the minimal arrangement of atoms, molecules or ions that posses the necessary symmetry to build the lattice by its repetition through all of space, is called the unit cell.

The advancement of quantum chemistry, solid state physics and the emergence of computer science gave rise to the *ab-initio* era in the late XX century. This refers to a scientific renaissance in which *ab-initio* (first-principles) methods and high-performance computing are used jointly for the modeling of materials (or molecules) based on a minimal amount of physical parameters (with

no need for adjustable or empirical parameters!), and prediction (or postdiction) of their properties. Hence, using first-principles computational techniques, it is possible to design functional materials before they are synthesized in the laboratory and guide experimental colleagues.

Using quantum chemical methods and computation, it is possible to tackle a variety of problems in materials science, such as:

(i) What are the ground state properties a given material A?

(ii) How will A behave outside equilibrium?

(iii) How does A respond to an external electric field $\mathscr{E}$?

(iv) How does A respond to an external magnetic field H?

(v) How does A respond to heat, i.e. Q?

(vi) What is needed to modify material A with property x to A' with x'?

(vii) If material A has properties $x_1, x_2, ..., x_n$, what other materials $B, C, ..., N$ exist with similar properties?

(viii) If materials A and B have properties x and y respectively, then what properties will characterize C if $C = A + B$?

Alternatively, rational design of materials can be achieved by intentionally controlling the composition and structure of a material as a function of the desired property. Without hyperbole, we state that computational simulations and chemical/materials informatics are the pillars of the "materials by design" paradigm. With first-principles methods, it is feasible to part from chemical induction and use physical rigor to make knowledgeable predictions (or postdictions) of a given system's fundamental properties and therefore its applications. A variety of such techniques exist, however in this thesis we will focus our attention on the application of the many-body theory known as Kohn-Sham Density Functional Theory (DFT) for the quantum mechanical modeling of solid-state materials. It is difficult to overemphasize the importance and power of Kohn-Sham DFT, as it is currently the most accepted and used theory in theoretical materials science. Here, we will use DFT to model

and characterize a selection of ternary transition metal chalcogenides in two and three dimensions. In particular, we employ DFT to (i) theoretically characterize a family of bulk compounds referred to as Alkali-Ion Transition-Metal Chalcogenides and (ii) propose the two-dimensional (monolayer) models of a family of known Niobium Tellurides with first-row magnetic transition-metals.

1.1 Transition metal chalcogenides

Transition metal "chalcogenides" are materials composed of two species of more: transition metals (groups I_B-$VIII_B$) and from the VI_A group. Particularly, the group VI_A elements considered are S, Se and Te (i.e. O is excluded). Transition metal chalcogenides are therefore the sulfides, selenides and tellurides of transition metals with general formula MX_n (M = transition metal , X = chalcogen atom, n is an integer). It is important to note that chalcogenides of transition metals are distinct from oxides due to differences between O and the S,Se,Te atoms themselves [**2**]. The main distinctions between MO and MX systems are that:

(i) The chalcogen atoms are heavier than oxygen.

(ii) The chalcogen atoms are less electronegative than oxygen.

(iii) The chalcogen atoms have ergetically accesible d orbitals (S [$3d$], Se [$4d$], Te [$5d$]) while oxygen does not.

(iv) As a consequence of (ii) and (iii), M-X bonds are largely covalent.

(v) As a consequence of (i) and (iii), chalcogen atoms are more polarizable than oxygen.

The atomic differences between O and the X atoms have deep implications in what defines chalcogenide chemistry. Particularly, whether O or an X atom reacts with M can radically define the composition, structure, chemical and physical properties of the material. For instance, (ii) implies that X atoms covalently bonded to a transition metal may be in oxidation state X^{-1}, while O will be in O^{-2}. In point (iv), it was stated that MX bonds are usually covalent. The origin of covalency here is resides in the strong s, p orbital mixing of the chalcogen (e.g. $3s/3p$ for S, etc.) with the

outer s, p orbitals of the metal (e.g. $4s/4p$ for d transition and post-transition elements, such as Mo [$4d$].). In many MX systems, this gives rize to a broad valence band (VB) and a broad conduction band (CB), where the VB and CB bands are composed of chalcogen bonding and transition-metal antibonding states respectively. Thus, given the composition of the valence and conduction bands, there usually exists an energy gap (bandgap) between the two. In summary, they are generally semiconducting materials.

Recall point (ii); in general, the bandgap in transition-metal chalcogenides is narrower than in oxides. This is due to the fact that since O is more electronegative, the valence band maximum (VBM) lies at a lower energy than in chalcogenides (the CB is usually unaffected, as it is composed of antibonding states). Hence, it is also generalized that the bandgap will decrease as electronegativity decreases. According to the Pauling scale: O ($\chi = 3.44$), S ($\chi = 2.58$), Se ($\chi = 2.55$), Te ($\chi = 2.1$) [**3**]. Thus, larger bandgaps are to be expected from sulphides, followed by selenides and then tellurides, which in cases lead to metallicity [**2**]. Transition-metal chalcogenides provide a large chemical space to explore, containing binary, ternary, quaternary materials with remarkable properties. One interesting trend in transition metal chalcogenides, is the favored crystallization of the compounds in low-dimensional structures. These systems form networks or lattices (sublattices in ternary and quaternary compounds) of MX coordination polyhedra, where the polyhedra edges(faces) are fomred(connected) by X-X bonds. In AMX systems, for instance, the A ions may be situated between infinite quasi-one(two) dimensional chains(sheets) of MX polyhedra. These materials may be understood as A(MX) structures.

In layered two-dimensional transition-metal chalcogenides, particularly in transition-metal dichalcogenides MX_2 (X-M-X sandwich), the difference in oxidation states between the metal and chalcogen (+4 and -2 respectively) lead to strong ionic bonds. This favors the stability of the monolayered structure, which can be exfoliated due to the weak long-range interactions between layers, van der Waals forces [**4**].

Essentially, three types of ternary transition metal chalcogenides exist. The first, which will not

be discussed in this thesis, is the system composed of one transition metal, and two chalcogen species (e.g. MoSeS). Although this type of chalcogenide is beyond the scope of this thesis, we refer the reader to refernces [**5**, **6**].

Second, is the AMX system where A is a main-group element, or a post-transition element. In this category, we will study alkali-metal/transition-metal selenides and sulfides. These are bulk structures hypothesized to be semiconductors, with potential applications in optoelectronics and energy storage devices.

The last type of ternary transition-metal chalcogenide is a metal-rich system, composed of two transition metals and one chalcogen (e.g. Ag_2WSe_4) [**7**]. By controlling the chemical composition of our bimetallic system, it is possible to engineer quantum materials. For instance, first-row transition metals such as V, Cr, Fe, Co and Ni may give rise to chalcogenides with magnetic properties. Here, we aim to model three 2D bimetallic chalcogenides with potential applications in spintronics.

Let us briefly define ferromagnetic, antiferromagnetic and ferrigmagnetic materials. Ferromagentic materials are defined as crystalline systems that undergo spontaenous magnetization resulting from the alignment (parallel) of uncanceled magnetic moments in absence of an external magnetic field H. Materials in which the magnetic moments form two equivalent but oppositely oriented (antiparallel) magnetic sublattices are deemed antiferromagnetic. Lastly, if the magnetic moments forming the magnetic sublattice are antiparallel but inequivalent, spontaneous magnetization occurs and the material is ferrimagnetic [**8**, **9**].

Therefore as part of this thesis, we theoretically model potentially magnetic two-dimensional niobium tellurides.

1.2 Objectives

In this thesis we aim to employ quantum chemical computations based on Density Functional Theory to predict the physical properties of different sets of bulk and two-dimensional ternary transition

model chalcogenides.

First, we will employ a materials informatics approach combined with quantum-chemical computations to determine the stable phase and electronic structure of the sodium molybdenum selenide Na_2MoSe_4.

Second, we will apply Density Functional approximations to comprehensively study the general electronic structure of the A_2MX_4 family of compounds, where A is an alkali cation (K^+, Rb^+, Cs^+), M is a transition metal (Mo or W) and X is a chalcogen anion (S^- or Se^-).

Finally, we propose three new two-dimensional materials, $NbMTe_2$, where M is Fe, Co or Ni. Using Density Functional Theory, we will identify their ground-state structures, asses their stability, and model their electronic structure and magnetic properties.

1.3 Outline

In Chapter 2, the theoretical methods used in this work are outlined. Hence, a description of relevant basic topics in quantum chemistry are provided as well as the development and fundamentals of Density Functional Theory. A few technical concepts are also introduced, such as the form of the exchange-correlation functional, pseudo-potentials, and the loop for self-consistency. Any further and project-specific methods and concepts crucial to the description of the materials will be introduced as deemed necessary throughout this text.

This thesis can be discussed in two parts. In the first, we are concerned with bulk materials; alkali-metal transition metal chalcogenides.

In Chapter 3, the crystal structure, thermodynamics and electronic properties of Na_2MoSe_4 are investigated. The crystal structure of this compound was not known, for which a materials-informatics approach was used to generate and then evaluate chemically sound hypothetical structures. Specifically, we perform first-principles computations on four likely candidates predicted by data-mining combined with ionic substitution. Structural optimization, formation enthalpies, band

structure and density of states are discussed for the candidates.

In Chapter 4, a comprehensive theoretical study was carried out to generalize the physics learnt from Na_2MoSe_4 to the vast A_2MX_4 family. Here, A is a group I element (K^+, Rb^+, Cs^+), M is a transition metal (Mo, W) and X is a chalcogen anion (S^- or Se^-). We discuss the equilibrium geometries and electronic band structures of twelve compounds, of which nine are reported in the ICSD and three are predicted in this work.

In the second part of this thesis, we focus our attention to beyond-graphene two-dimensional materials. Inspired by the recent discovery of ferromagnetism in van der Waals layered materials such as $CrGeTe_3$, and, the increasing interest in topological materials such as $NbTe_2$, we psopsoe a new family of 2D quantum materials.

In Chapter 5, we use DFT to model the monolayers of a family of ternary niobium tellurides, $MNbTe_2$ (M=Fe,Co,Ni). We investigate their relative stability by means of thermodynamics, electronic and magnetic properties and elaborate on their potential applications in spintronic devices. This is the first investigation of $MNbTe_2$ strictly as two-dimensional materials.

Finally, in chapter 6, we present a summary of the systems studied, their discovered properties and potential applications. We also provide perspective to guide future investigations, and we conclude this thesis.

Chapter 2

Theoretical Methods

2.1 Quantum Chemistry

2.1.1 The Many-Body Schrödinger Equation

The central focus of quantum chemistry, is to find approximate solutions to the many-body Schrödinger equation. The many-body Hamiltonian operator $\mathcal{H}$ for a system of N particles, nuclei and electrons at given positions $\mathbf{r}_j$ and $\mathbf{r}_k$ respectively, is given by

$$\mathcal{H} = -\sum_{k=1}^{N} \frac{1}{2}\nabla_k^2 - \sum_{j}^{M} \frac{1}{2M_j}\nabla_j^2 - \sum_{k=1}^{N}\sum_{j}^{M} \frac{Z_j}{r_{kj}} + \sum_{k=1}^{N}\sum_{q>k}^{N} \frac{1}{r_{kk'}} + \sum_{j=1}^{M}\sum_{j'>j}^{M} \frac{Z_j Z_{j'}}{R_{jj'}}. \tag{2.1}$$

Here, in Eq. 2.1 the many-body Schrödinger is written in atomic units for convention ($\hbar = m = e = 1$). Note that M_j is the nucleus(j)-electron mass ratio and Z_j is the atomic number for nucleus (j). The quantities $r_{kk'}$ and $r_{jj'}$ represent electron-electron and nucelus-nucleus distances respectively. This seemingly intimidating and analytically unsolvable equation can be broken down in the following terms: the first operator term describes the kinetic energy of electrons, followed by the kinetic energy operator for the nuclei, the nucleus-electron Coulomb interaction potential (attraction), and finally

the repulsive electron-electron and nucleus-nucleus Coulomb interaction potentials, as under-braced in Eq. 2.2

$$\mathcal{H} = \underbrace{-\sum_{k=1}^{N} \frac{1}{2}\nabla_k^2}_{\mathcal{T}_N} \underbrace{-\sum_{j}^{M} \frac{1}{2M_j}\nabla_j^2}_{\mathcal{T}_M} \underbrace{-\sum_{k=1}^{N}\sum_{j}^{M} \frac{Z_j}{r_{kj}}}_{\mathcal{U}_{Ne}} + \underbrace{\sum_{k=1}^{N}\sum_{q>k}^{N} \frac{1}{r_{kk'}}}_{\mathcal{U}_{ee}} + \underbrace{\sum_{j=1}^{M}\sum_{j'>j}^{M} \frac{Z_j Z_{j'}}{R_{jj'}}}_{\mathcal{U}_{NN}}. \tag{2.2}$$

This many-body Hamiltonian can be re-written in condensed form as a sum of its constituent operators.

2.1.2 The Born-Oppenheimer approximation

Fortunately for us, nuclei are significantly more massive than electrons. Hence, it is possible to treat electron dynamics as if they were independent or separable to nuclear dynamics, i.e. it is possible to treat electrons orbiting around a fixed nucleus. This leads us to neglect terms in equation 2.2, yielding an *electronic* Hamiltonian $\mathcal{H}_{elec}$, acting on the electronic wave-function Ψ_{elec}.

$$\mathcal{H}_{elec} = -\sum_{k=1}^{N} \frac{1}{2}\nabla_k^2 - \sum_{k=1}^{N}\sum_{j}^{M} \frac{Z_j}{r_{kj}} + \sum_{k=1}^{N}\sum_{q>k}^{N} \frac{1}{r_{kk'}}. \tag{2.3}$$

In our electronic Hamiltonian 2.3, we describe the motion of N electrons under the effects of a field of M fixed point charges. It is worth noting that the second term in $\mathcal{H}_{elec}$ that includes electron-nuclei interaction, is usually expressed as an external potential $V_{ext}(r_k)$. Following the same line of thought, it is possible to formulate a nuclear Hamiltonian operator $\mathcal{H}_{nuc}$ and solve for the motion of the nuclei. In conclusion, the Born-Oppenheimer approximation represents a milestone in quantum mechanics and lies at the heart of quantum chemistry.

2.1.3 The Hartree-Fock Approximation

Hartree-Fock (HF) theory is one of the main pillars upon electronic structure theory and computational quantum chemistry are built [**10**]. It is the basis for Molecular Orbital (MO) theory, and lay

the foundations for CQM methods known as post-HF theories. These include molecular methods such as many-body perturbation theory (MBPT), configuration interaction (CI), and the method we focus on in our thesis, DFT.

At a glance, HF theory parts from the idea of the Hartree product (HP), which states that a many-body wavefunction Ψ_{HP} can be seen as the product of the constituent electron wavefuntions $\psi_i(\mathbf{r}_i)$. An important approximation in the HP is that electrons are independent particles, meaning that they do not interact with each other . As a consequence, the HP fails to satisfy the *principle of antisymmetry*, also known as the Pauli exclusion principle. The Pauli exclusion principle states that the electronic wave functions must be antisymmetric with respect to the interchange of space coordinates x_i and spin coordinates χ_j of any two electrons. In other words, two electrons occupying the same orbital *must* have opposite spins $(\uparrow, \downarrow)$.

The solution that Hartree and Fock proposed was to construct the many-body wavefunction in such a manner that the antisymmetry principle is satisfied. This was achieved using an antisymmetrized product, or a *Slater Determinant*, as shown in2.4,

$$\Psi_{HF}(\mathbf{r}_1, \mathbf{r}_2, ..., \mathbf{r}_N) = \frac{1}{\sqrt{N!}} \begin{bmatrix} \chi_1(1) & \chi_2(1) & \chi_3(1) & \dots & \chi_N(1) \\ \chi_1(2) & \chi_2(2) & \chi_3(2) & \dots & \chi_N(2) \\ \vdots & & & \ddots & \\ \chi_1(N) & \chi_2(N) & \chi_3(N) & \dots & \chi_N(N) \end{bmatrix} \tag{2.4}$$

where $\Psi_{HF}(\mathbf{r}_1, \mathbf{r}_2, ..., \mathbf{r}_N)$ is N particle antisymmetric wave function. The fact that we can write our N particle wave function in the form of a Slater determinant has severe implications. One is that this form satisfies the requirement of electron *indistinguishibility* - meaning that from a reference of measurement, one electron is indistinguishible from another. This means that every electron is associated with every spin orbital χ_i. Additionally, writing our wave-function in Slater determinant form is also equivalent to saying that the motion of electron i is independent of the motion of electron j and k. Hence, electron i only feels Coulomb repulsion and undergoes an due

to the average positions of the other $N-1$ electrons. Also, the electrons experience an "exchange" interaction due to antisymmetrization. For this reason, it is said that HF theory is an independent particle model. It is also considered a mean-field theory or as we know it in quantum chemistry and physics, *self consistent field theory.*

Another important concept in quantum chemistry and HF theory is the variational principle. According to the variational principle, we can approximate the ground state energy (lowest energy accessible to the system) E_0 of an N particle system by systematically varying the spin orbitals χ_a (as long as they satisfy the orthonormality condition), $\langle \chi_a \rangle \, \chi_b = \delta_{ab}$. The equation that leads us to the set of χ_a that in return yield E_0, is the HF equation

$$\underbrace{-\sum_{k=1}^{N} \frac{1}{2}\nabla_k^2 - \sum_{k=1}^{N}\sum_{j}^{M} \frac{Z_j}{r_{kj}}}_{\mathcal{H}_{elec}} + \sum_{b\neq a}\left[\int d\mathbf{x}_2 \chi_b(2)^2 r_{12}^{-1}\right]\chi_a(1) - \sum_{b\neq a}\left[\int d\mathbf{x}_2 \chi_b^*(2)\chi_a(2) r_{12}^{-1}\right]\chi_b(1). \tag{2.5}$$

For the sake of brevity, we limit our further discussion of HF theory and the derivation of the HF equations. However, it is important to highlight the importance of the HF equation. Equation 2.5 can be expressed in terms of a set of operators, including $\mathcal{H}_{elec}$, the Coulomb operator $\mathcal{J}_b$, the exchange operator $\mathcal{K}_b$, and the Fock operator $\mathcal{F}$. We write the $\mathcal{F}$ as

$$\mathcal{F} = \mathcal{H}_{elec} + \underbrace{\sum_{b} \mathcal{J}_b(1) - \mathcal{K}_b(1)}_{\mathcal{U}_{HF}} \tag{2.6}$$

where one can easily see that $\mathcal{J}_b$ and $\mathcal{K}_b$ correspond by the second and third terms of Eq.2.6. Their sum is known as the HF potential $\mathcal{U}_{HF}$.

Equation 2.6 can now be re-written as a pseudo-eigenvalue problem,

$$\mathcal{F}(x)_1 \chi(x)_1 = \varepsilon_i \chi_i(x)_i. \tag{2.7}$$

From here, the next step is to introduce basis set, which acts on the HF equations and transforms them into the Roothan equations. Through some cumbersome algebra that is definitely outside the scope of this thesis, we highlight that they can be simplified into an eigenvalue-type equation of the form

$$\mathbf{FC} = \mathbf{SC}\varepsilon_i \tag{2.8}$$

where $\mathbf{F}$ is the Fock matrix, $\mathbf{C}$ is a $k \times k$ matrix of the basis expansion coefficients and $\mathbf{S}$ is the overlap matrix. An orthogonalization of the basis will cause $\mathbf{S}$ to vanish. Also, note that we have not explicitly written $\mathbf{F}$, but The procedure to solve equation 2.8 must be iterative, as $\mathbf{F}$ must be solved through the orbitals.

With the provided information, one can now discuss the Self Consistent Field (SCF) workflow for HF. The SCF workflow is also used in Density Functional Theory.

2.2 Density Functional Theory (DFT)

Until now, quantum chemistry has been treated in terms of quantum particle wavefunctions Ψ. Although wavefunction methods yield information closer to the true solution of the Schrodinger equation, Ψ depends on $3N$ variables, while $\rho(\mathbf{r})$, the electronic density, is only spatially dependent. This electron density for a normalized wavefunction Ψ is

$$\rho(\mathbf{r}) = N \int d^3\mathbf{r} \cdots \int d^3\mathbf{r}_N \Psi^*(\mathbf{r}, \mathbf{r}_2, \ldots, \mathbf{r}_N)\Psi(\mathbf{r}, \mathbf{r}_2, \ldots, \mathbf{r}_N). \tag{2.9}$$

The electronic density $\rho(\mathbf{r})$ represents the probability of finding any of the N electrons within the enclosed volume, while the other $N-1$ electrons have arbitrary positions. For a normalized wavefunction, $\int d\mathbf{r}^3 \rho(\mathbf{r}) = N$. Note that by depending on only 3 coordinates versus the $3N$ in HF, $\rho(\mathbf{r})$ is more computationally efficient than Ψ. Furthermore, what makes using $\rho(\mathbf{r})$ all more appealing to use as our basic variable is that it is a physical observable. This is, $\rho(\mathbf{r})$ may be

determined experimentally via X-Ray Diffraction (XRD).

It is worth mentioning that the first approach to develop a theoretical framework to study the electronic structure of many-body systems in terms of the electron density $\rho(\mathbf{r})$ was developed by Llewellyn Thomas and Enrico Fermi. The Thomas-Fermi (TF) theory was derived semiclassically, and it used a density functional of the form $E[\rho]$ to approximated the kinetic energy through the idealization of a uniform electron gas of non-interacting electrons with equal density at any given point. With the crude approximation of a homogeneous $\rho(\mathbf{r})$ at any point in space and the failure to take into account for electron exchange and correlation, the TF failed to capture the physics of realistic systems. Paul Dirac incorporated electron exchange into the TF method, yielding the Thomas-Fermi-Dirac functional. However, this was not enough to perfect the semiclassicaly derived TF model, and defeat the purpose of a wavefunction-free electronic structure theory as the need to account for $3N$ variables re-emerged. Hence, the TFD approach was not physically feasible - but it lays the foundations for Kohn-Sham Density Functional Theory.

Towards a more accurate approach to DFT, Hohenberg and Kohn derive a purely quantum mechanical theory of many-body systems in terms of $\rho(\mathbf{r})$. Hence, they present a DFT that can be applied to systems of interacting particles moving through an external potential V_{ext}. Moreover, Kohn and Sham developed the self-consistent equations that account for exchange and correlation.

Today, the robust Kohn-Sham DFT holds its position as the most widely used and accepted electronic structure theory in condensed matter and materials physics. It provides sufficient accuracy and computational feasibility to treat extended systems through quantum mechanics. In this section, an introductory description of Kohn-Sham DFT is provided to lay the foundations upon this work was realized [**11**, **12**, **13**].

2.2.1 The Hohenberg-Kohn Theorems

In 1964, Pierre Hohenberg and Walter Kohn began the derivations that would be the bedrock of modern materials physics. They derived an *exact many-body theory* to determine the ground state

of an interacting electron gas described by the Hamiltonian $\mathcal{H} = \mathcal{T} + \mathcal{U} + \mathcal{V}$, using the electronic density as their basic variable. In $\mathcal{H}$, the first two terms are the general kinetic energy and Coulomb interaction terms, and $\mathcal{V}$ depends on an external potential $U_{ext}(\mathbf{r})$.

Theorem I: For any system of interacting particles in an external potential $U_{ext}(\mathbf{r})$, the potential is determined uniquely by the ground state electronic density $\rho(\mathbf{r}) = \rho_0$, except for a constant. This constant can be the difference $\Delta U = U_{ext} - U'_{ext}$ of two particles trapped in potentials U_{ext} and U'_{ext} respectively.

Corollary: This implies that $\mathcal{H}$ is now fully determined, except for a constant shift of the energy. Hence, the U_{ext} and all of the ground state properties of the system, including the many-body wavefunction Ψ_0 are determined by ρ_0. Concretely, the expectation value of any observable $\hat{O}$ is a unique functional of ρ_0 :

$$O_0 = O[\rho_0] = \langle \Psi[\rho_0] | \, \hat{O} \, | \Psi[\rho_0] \rangle \tag{2.10}$$

The importance of this theorem cannot be overemphasized. What Hohenberg and Kohn demonstrated, is that there is a unique correspondence between an N-body system's Ψ_0, ρ_0 and U_{ext}. The theoreticians demostrated that for non-degenerate ground states, if we know the form of U_{ext}, we therefore know ρ_0, and vice versa. This is because the one-to-one correspondence $U_{ext} \Leftrightarrow \rho_0$ indicates that the system's Hamiltonian is now fully known and therefore may be solved for all quantum states (ground and excited), causing the system to be fully characterized, as illustrated by by Eq. 2.10.

In the seminal paper, *"Inhomogenous Electron Gas"*[**14**], the authors provided a simple proof preceeded by *reductio ad adsurdum.* They define an additional system, with ground state Ψ' and $U'_{ext}(\mathbf{r})$, and that $\Psi \rightarrow \rho_0(\mathbf{r})$ and $\Psi' \rightarrow \rho_0(\mathbf{r})$ (i.e. they both yield the same density). Note that unless $U_{ext} - U'_{ext}$ is a constant, $\Psi \neq \Psi'$.

The Schrödinger equations for our two systems are $\mathcal{H}\Psi = E\Psi$ and $\mathcal{H}'\Psi' = E'\Psi'$. Since E and E' are the ground state energies of $\mathcal{H}$ and $\mathcal{H}'$ respectively, they must satisfy the variational principle,

$$E = \langle \Psi | \, \mathcal{H} \, | \Psi \rangle < \langle \Psi' | \, \mathcal{H} \, | \Psi' \rangle \, , \tag{2.11}$$

$$E' = \langle \Psi' | \, \mathcal{H}' \, | \Psi' \rangle < \langle \Psi | \, \mathcal{H}' \, | \Psi \rangle \, . \tag{2.12}$$

Such that

$$E < \langle \Psi' | \, \mathcal{H} \, | \Psi \rangle = E' + \int \Delta U \rho_0(\mathbf{r}) d\mathbf{r}, \tag{2.13}$$

$$E' < \langle \Psi | \, \mathcal{H}' \, | \Psi \rangle = E + \int \Delta U \rho_0(\mathbf{r}) d\mathbf{r}. \tag{2.14}$$

It is said that the proof is done by *reductio ad adsurdum*, since the sum of the two previous expressions yields a contradiction,

$$E + E' < E' + E. \tag{2.15}$$

Therefore, it is shown that two potentials that differ by more than an additive constant cannot and will not yield the same electronic density. It is unique.

Theorem II: For an N particle system acted on by a potential U_{ext}, it is possible to construct an exact functional for the total energy in terms of the electron density $\rho(\mathbf{r})$, yielding $E[\rho]$. Particularly, for a given potential U_{ext}, the global minimum of $E[\rho]$ is the ground state energy E_0 corresponding to and only to the exact ground state density ρ_0.

The universal Hohenberg-Kohn functional, $F[\rho]$, is expressed as

$$F[\rho] = T_i[\rho] + U[\rho]. \tag{2.16}$$

For an N particle system and a given potential U_{ext}, a $F[\rho]$ exists such that

$$E_{(U_{ext},N)}[\rho] = F[\rho] + \int d^3\mathbf{r} U_{ext}(\mathbf{r}) \rho(\mathbf{r}). \tag{2.17}$$

The ground state energy E_0 of the system can be obtained variationally, this is,

$$E_0 = \min_{\rho \to N} E[\rho] \tag{2.18}$$

from the minimizing $\rho(\mathbf{r})$, which is in turn, ρ_0. Therefore,

$$\frac{\delta E[\rho]}{\delta \rho} = 0. \tag{2.19}$$

The second Hohenberg-Kohn theorem has two very important points. First, that $F[\rho]$ is universal, meaning it is valid for (or independent of) any U_{ext}. This means that, in principle, there exists an $F[\rho]$ valid for any system regardless of its size. Furthermore, DFT is a computationally efficient (3 spatial coordinates) framework that minizes $\rho(\mathbf{r})$, minimizing $E[\rho]$.

2.2.2 The Kohn-Sham equations

The Hohenberg-Kohn theorems by themselves do not provide insight into how to solve for E_0. Walter Kohn and Lu Jeu Sham reformulated the many-body problem of Eq. 2.1 as a set of many single-particle problems that are solvable[1]. This is, they take us from an N-particle Schrödinger equation to N one-electron Schrödinger-like equations that may be solved self-consistently [**15**].

First, let us retake the concept behind equation Eq. 2.17 and apply that to an arbitrary energy $E[\rho]$;

$$E[\rho] = \langle \Psi[\rho] | \, \mathcal{T} + \mathcal{U}_{eff} \, | \Psi[\rho] \rangle \tag{2.20}$$

where as a reminder, $\mathcal{T}$ and $\mathcal{U}_{eff}$ are the kinetic energy and effective potential in which the particles are moving, respectively. If we wish to decompose $\mathcal{U}_{eff}$ as a sum of potentials $\mathcal{U}_k$, we rewrite $E[\rho]$

[1] Fun fact: The Kohn-Sham equations were derived in La Jolla, CA! Hopefully, the author of this thesis will also derive new many-body models at UC San Diego.

as:

$$E[\rho] = \mathcal{T}[\rho] + \mathcal{U}_H[\rho] + \mathcal{U}_{Ne}[\rho] + \mathcal{U}_{NN}[\rho] + \mathcal{U}_{xc}[\rho] \tag{2.21}$$

where $\mathcal{U}_H[\rho]$ is the Hartree component of the electron-electron interaction energy, given by

$$\mathcal{U}_H[\rho] = \frac{1}{2}\int d^3\mathbf{r}d^3\mathbf{r}'\frac{\rho(\mathbf{r})\rho(\mathbf{r}')}{|\mathbf{r}-\mathbf{r}'|}. \tag{2.22}$$

The first two terms of $E[\rho]$ are universal as they are valid for any N particle system composed of electrons and nuclei, while there is no exact form of the fifth term, the exchange-correlation potential $\mathcal{U}_{xc}[\rho]$. From here, it is possible to solve for the single particle Schrödinger-like equations, called the Kohn-Sham equations, given by

$$\left(\frac{1}{2}\nabla^2 + \mathcal{U}_{\uparrow\{\{}(\mathbf{r})\right)\phi_i(\mathbf{r}) = \varepsilon_i\phi_i(\mathbf{r}). \tag{2.23}$$

As seen in equation 2.23, solving the Kohn-Sham equations for the non-ineracting system yields orbitals ϕ_i which can reproduce ρ of the original N-particle system. As usual, there is a variational relationship between $\mathcal{U}_{xc}[\rho]$ and $\mathcal{E}_{xc}[\rho]$, given by

$$\mathcal{U}_{xc}(\mathbf{r}) = \frac{\delta\mathcal{E}_{xc}[\rho]}{\delta\rho(\mathbf{r})}. \tag{2.24}$$

2.2.3 Exchange and correlation functionals

Density Functional Theory is a rigorous and precise theory for ground state quantum mechanics. However, since we do not know the exact form of $\mathcal{U}_{xc}$, we are obliged to approach it through approximations, known as Density Functional Approximations (DFAs). Keeping this in mind, the accuracy of our ground state is determined by the accuracy of our DFA. Fortunately, $\mathcal{E}_{xc}$ represents only a fraction of $E[\rho]$, making Kohn-Sham DFT an overall robust theory. The most common formulations of $\mathcal{U}_{xc}[\rho]$ are defined below.

Local Density Approximation (LDA)

The simplest formulation of $\mathcal{U}_{xc}[\rho]$ is the Local Density Approximation (LDA), written as

$$\mathcal{U}_{xc}^{LDA}[\rho] = \int d^3\mathbf{r}\rho(\mathbf{r})\mathcal{E}_{xc}(\rho(\nabla)). \tag{2.25}$$

Within the LDA, the exchange and correlation energy $\mathcal{E}_{xc}(\rho(\mathbf{r}))$ is approximated as a local function of the spatially-dependent density that reproduces the known exchange-correlation energy per electron in a uniform or homogeneous electron gas (HEG). As a result of the simplicity of the LDA, irregularities caused by neighboring particle interactions are neglected.

Built upon the local density approximation, is the local spin-density approximation (LSDA). It is used to model spin-polarized systems.

$$\mathcal{U}_{xc}^{LSDA}[\rho_\uparrow, \rho_\downarrow] = \int d^3\mathbf{r}\rho(\mathbf{r})\mathcal{E}_{xc}(\rho_\uparrow, \rho_\downarrow) \tag{2.26}$$

A note: in the LDA, $\mathcal{E}_{xc}$ is approximated as $\mathcal{E}_{xc} = \mathcal{E}_x + \mathcal{E}_c$, where $\mathcal{E}_x$ and $\mathcal{E}_c$ are the exchange and correlation energies respectively. This is important, as these quantities are usually missed by the LDA due to the definition of ρ as a constant throughout every point in space. Particularly, LDA underestimates $\mathcal{E}_x$ and overestimates $\mathcal{E}_c$. This systemic error can be overcome by the General Gradient Approximation.

General Gradient Approximation (GGA)

As mentioned above, the LDA fails to quantify $\mathcal{E}_{xc}$ due to its treatment of ρ as that of a uniform electron gas. In order to account for the inhomogenities of a more realistic electron density, the gradient of the density $\nabla\rho$ is expanded at each point, yielding:

$$\mathcal{U}_{xc}^{GGA}[\rho_\uparrow, \rho_\downarrow] = \int d^3\mathbf{r}\rho(\mathbf{r})\mathcal{E}_{xc}(\rho_\uparrow, \rho_\downarrow, \nabla\rho_\uparrow, \nabla\rho_\downarrow,). \tag{2.27}$$

This approximation is known as the General Gradient Approximation (GGA), and is widely used due to its proven capabilities of yielding accurate lattice constants and ground state energies when compared to experiments. Today, the GGA remains the work-horse approximation for DFT-based condensed matter physics. Although GGA is widely used in modeling periodic systems, it is often convenient to incorporate potentials to numerically correct for exchange, correlation (meta-GGA, GGA+U) or both (hybrid functionals).

2.3 Periodic Density Functional Theory

In the previous section, we have layed out the fundamental concepts in Density Functional Theory. Here, we briefly explain how DFT is used to describe the physics of a system containing an infinite number of atoms, ions or molecules, and in principle, an infinite number of electrons. The main distinction between molecular (finite) and solid-state DFT, is that here we use periodic boundary conditions and a planewave basis set. First, let us turn to the central concept of the quantum theory of solids: the problem of a periodic potential.

2.3.1 Bloch's theorem

Here, it is necessary to turn to the Bloch theorem, which states that the crystal momentum k is a conserved quantum number and provides the boundary condition $V(\mathbf{r}) = \mathbf{V}(\mathbf{r} + \mathbf{T})$ for the single particle wavefunction ϕ_k. This is, the single particle wavefunctions satisfy periodicity as does the crystal lattice itself [**16**]. Hence,

$$\phi_{n\mathbf{k}}(\mathbf{r} + \mathbf{T}) = \exp\left[i\mathbf{k} \cdot \mathbf{T}\right]\phi_{\mathbf{k}}(\mathbf{r}) \tag{2.28}$$

where $\mathbf{T}$ is a direct lattice translation vector. The general solution for $\phi_{\mathbf{k}}(\mathbf{r})$ that satisfies the boundary condition reads

$$\phi_{n\mathbf{k}}(\mathbf{r}) = \exp\left[i\mathbf{k}\cdot\mathbf{r}\right] \underbrace{\sum_{\mathbf{G}} c_{n\mathbf{k}}(\mathbf{G}) \exp[i(\mathbf{k}+\mathbf{G})\cdot r]}_{U(\mathbf{k},\mathbf{r})} \tag{2.29}$$

Here, n is the band-index, and $\mathbf{G}$ are reciprocal lattice vectors from which the periodic function $U(\mathbf{k},\mathbf{r})$ may be infinitely through $\mathbf{k}$. The reciprocal lattice vectors $\mathbf{G}$ are defined as

$$\mathbf{G} = m_1\mathbf{b_1} + m_2\mathbf{b_2} + m_3\mathbf{b_3}. \tag{2.30}$$

In essence, equation 2.29 expresses the Bloch theorem, and $\phi_{n\mathbf{k}}(\mathbf{r})$ is called a Bloch function.

Theorem: The eigenvalues of the wave equation for a periodic potential are the product of a plane wave $\exp[i(\mathbf{k}+\mathbf{G})]$ times a function $U(\mathbf{k},\mathbf{r})$ which contains the periodicity of the crystal lattice.

The Bloch theorem allows us to take advantage of the periodicity and avoid the explicit calculation of an infinite amount of wavefunctions for an infinite amount of electrons (in an infinitely extended structure). As lower-order kinetic energy terms will have greater influence on the calculation of ϕ_k, we determine a cut-off for the expansion (i.e. define a finite set of plane-waves).

2.3.2 The Pseudopotential Approximation

Solids are made up of electrons and nuclei interacting strongly through the Coulomb potential. However, we distinguish between two types of electrons in electronic structure calculations; the valence and core electrons. In most cases, the core electrons are strongly bound and are essentially fixed with respect to the (exterior) valence electrons. Furthermore, these core electrons due not in general participate in bonding, and are energetically positioned at deep levels i.e. $E << E_F$, where E_F is the Fermi energy (the highest occupied state at zero temperature). Hence, it is reasonable to replace

the strong core potential Ze^2/r with a pseudopotential V^{PS}, whose ground state wavefunction ϕ^{PS} mimics the all electron valence wavefunction beyond a determined core-radius r_c.

The use of V^{PS} rather than the actual crystal potential is called the pseudopotential approximation, or the frozen-core approximation, as the core states are fixed in an atomic reference configuration [**17**].

Norm-Conserving Pseudopotentials (NCPP)

The development of pseudopotential methods, and pseudopotentials themselves was fueld by three criteria:

- *Softness:* Soft pseudopotentials were desirable, as this would allow using as few planewaves as possible (i.e. low kinetic energy cutoff).
- *Transferability:* The pseudopotentials should be as transferable as possible. This refers to (i) that a pseudopotential generated at a given atomic configuration should reproduce others at reasonable accuracy and (ii) that a pseudopotential for element A in the solid state should be valid in other chemical environments, such as AB, AC, ABC, etc.
- *Accuracy:* The pseudo-charge density should reproduce the valence charge density as accurately as possible.

In norm-conserving pseudopotentials, introduced by G. B. Bachelet, D. R. Hamann, and M. Schlüter, these criteria are (to an extent) met [**18**] The norm-conserving pseudopotentials are generated in such a way that the pseudo- wavefunctions are equal to the all-electron wavefunctions outside r_c. Inside the core radius, the pseudo-wavefunctions may differ from the all-electron wavefunctions, as long as the norm is constrained to remain unchanged. textcolorredNorm-conserving pseudopotentials are often called semi-local potentials, similar to that of the Augmented Planewave (APW) method., tambien esta de mas eliminar

Ultrasoft Pseudopotentials (USP)

Ultrasoft pseudopotentials, introduced by D. Vanderbilt [**18**], posed a radical departure from the concept of norm-conservation. As with norm-conserving pseudopotentials, ultrasoft pseudopotentials must satisfy the condition that for $r > r_c$, the pseudo-wavefunctions must be equal to the all-electron wavefunction. However, for $r < r_c$, the constraint of norm-conservation is removed, thus the pseudo-wavefunctions are allowed to be "as soft as possible". In this scheme, it is possible to use large values of r_c, leading to a dramatic decrease in the required planewaves cutoff. Although ultrasoft pseudopotentials may represent faster convergence, removal of norm-conservation introduces some complications and can lead to poor transferability. Additionally, a larger kinetic energy cutoff for charge density is needed with respect to the kinetic energy cutoff for the wavefunctions, when compared to norm-conserving pseudopotentials. This is, the charge-density:wavefunction cutoff ratio is larger for ultrasoft pseudopotentials.

2.4 Relativistic Density Functional Theory

As we have discussed, in Kohn-Sham Density Functional Theory we do not solve for the ground state wavefunction ψ_0, but rather the ground state charge density ρ_0. Furthermore, let us recall that Kohn-Sham Density Functional Theory is an *ab-initio* theory for determining the ground state properties of non-relativistic many-particle systems. However, relativistic effects can be determining factor for much of the physics of high Z. Therefore, a relativistic formulation of DFT is required for such systems that can only be treated by relativistic quantum mechanics (RQM).

Relativistic Effects

Relativity can play an important role in the electronic structure of a many-body system composed of atoms with high Z. These differences due to relativistic effects are:

- Differences in the electron dynamics due to the velocity-dependence of the electron mass m_e.

- Magnetic interactions in the Hamiltonian operator due to the electron spin.
- By introducing relativistic terms in our Hamiltonian, we also introduce a "small" component of the wavefunction, which leads to a change in the shape of the orbitals.
- Modification of the potential operator due to c, which is finite.

The Dirac equation

The central theme in relativity is that c, the speed of light, is constant in all inertia frames. Additionally, the requirement that physical laws be identical in such frames, has as a consequence that space and time coordinates become "equivalent". A relativistic description of a particle requires, therefore, four coordinates.

For a free electron, Dirac proposed that the time-dependent Shcrödinger equation should be replaced by

$$\left(c\alpha \cdot \mathbf{p} + \beta mc^2\right)\Psi = i\frac{\partial \Psi}{\partial t} \tag{2.31}$$

where $c\alpha \cdot \mathbf{p} + \beta mc^2$ is the Dirac Hamiltonian, α and β are 4×4 matrices, $c\alpha$ is the relativistic velocity operator and α can be written in terms of the three Pauli spin matrices, and β in terms of the unit matrix $\mathbf{I}$. This is,

$$\alpha = \begin{pmatrix} 0 & \sigma_{x,y,z} \\ \sigma_{x,y,z} & 0 \end{pmatrix}, \beta = \begin{pmatrix} \mathbf{I} & 0 \\ 0 & -\mathbf{I} \end{pmatrix}$$
$$\sigma_x = \begin{pmatrix} 0 & 1 \\ 1 & 0 \end{pmatrix}, \sigma_y = \begin{pmatrix} 0 & -i \\ i & 0 \end{pmatrix}, \sigma_z = \begin{pmatrix} 1 & 0 \\ 0 & -1 \end{pmatrix}, \mathbf{I} = \begin{pmatrix} 1 & 0 \\ 0 & 1 \end{pmatrix} \tag{2.32}$$

Dirac-Kohn-Sham Equations

Relativistic Density Functional Theory (RDFT) is the formulation of DFT in which relativistic effects are taken into account via the Dirac equation shown in Eq 2.32. The central equations in RDFT are known as the Relativistic Kohn-Sham (RKS) or Dirac-Kohn-Sham equations [**19**],

$$\Big(ic\alpha + \beta mc^2 + \alpha_\mu \nu_s^\mu(\mathbf{r})\Big)\phi_k(\mathbf{r}) = \mathcal{E}_k\phi_k(\mathbf{r}). \tag{2.33}$$

Here, the multiplicative KS potential ν_s^μ consisting of the sum V^μ, the Hartree potential ν_H^ν and the xc-potential ν_{xc}^μ are

$$\begin{aligned} \nu_s^\mu(\mathbf{r}) &= eV^\mu(\mathbf{r}) + v_H^\mu(\mathbf{r}) + v_{xc}^\mu(\mathbf{r}) \\ \nu_H^\mu(\mathbf{r}) &= e^2 \int d^3r' \frac{j^\mu(\mathbf{r}')}{|\mathbf{r}' - \mathbf{r}'|} \\ \nu_{xc}^\mu(\mathbf{r}) &= \frac{\delta \mathcal{E}_{xc}[j]}{\delta j_\mu(\mathbf{r})}. \end{aligned} \tag{2.34}$$

The resemblance with the nonrelativistic KS equations is easy to see, however the derivations of the RKS equations is far but trivial. The extension of the HK theorem was achieved by Ragagopal and Callaway using Quantum Electrodynamics (QED). The authors used a QED-based Hamiltonian and the four-component density current j, and applied the *reductio ad absurdum* of the original HK theorem to demonstrate that the E_0 is a unique functional of the ground state four current density j_0 (i.e. $E[j]$). Aside from this, a rigorous treatment and renormalization is required to ensure that $E[j]$ contains the physics of QED. Like in DFT, The relativistic variant of the HK theorem guarantees the formal existence of a density functional description of relativistic systems but does not give any hint how to construct the crucial functional $E[j]$. Following the reasoning behind the derivation of the KS equations, and with the appropriate treatment, RDFT is constructed for the local density approximation of a relativistic non-interacting electron gas. In RDFT, the exchange-correlation functional is strictly defined by the four-component current-density j^μ dependence. Lastly, this

formulation is also used to generate j-dependent pseudopotentials, which we call "fully relativistic pseudopotentials" in planewave (or periodic) DFT [**20**, **21**] (thanks to this, we can model accurate band structues and study magnetic materials!).

2.4.1 Self-consistency in DFT

At this point, we shall focus on *how* we determine the ground states of materials using DFT, in practice. We describe what is known as the Self-consistent field (SCF) computation (also called SCF-cycle). Let us recall that the problem at hand is to solve the Kohn-Sham equations 2.23. The KS equations are solved iterative, beginning with an initial "guess" electron density $\rho_i(\mathbf{r})$, constructed from N and the spatial occupancies of the involved particles. This density is used then to construct $\mathcal{U}_{eff}$ (also known as the Kohn-Sham potential V_{KS}). Once the Kohn-Sham potential is constructed, the single-particle Kohn-Sham equations 2.23 are solved. Their solutions yield the Kohn-Sham orbitals $\phi_i(r)$, which are in turn summed through $\sum^N \phi_i n_i \phi*_i$ to obtain $\rho_f(\mathbf{r})$, the final electron density. Finally, if $\rho_f - \rho_i$ does not satisfy a given threshold, the two densities are mixed to create a new ρ_i , constructing a new $\mathcal{U}_{eff}$ and solve the KS equations. This process is repeated until $\rho_f - \rho_i \leq q$, where q is the SCF threshold. Once $\rho_f - \rho_i \leq q$ is met, the calcuation has converged and the ground state has been determined. We provide a schematic of the SCF cycle in Figure 2.1.

The typical default value for q is 1×10^{-6} for ground state calculations. Also, depending on the nature of a computation, the flowchart may be more complex. For example, for structural optimization, ions may be displaced and lattice vectors may change in magnitude at the end of each SCF cycle until the n and $n-1$ structures meet a given threshold. In this case, the total energy as well as the forces acting upon the atoms are calculated. The forces are calculated through the Hellman-Feynman theorem.

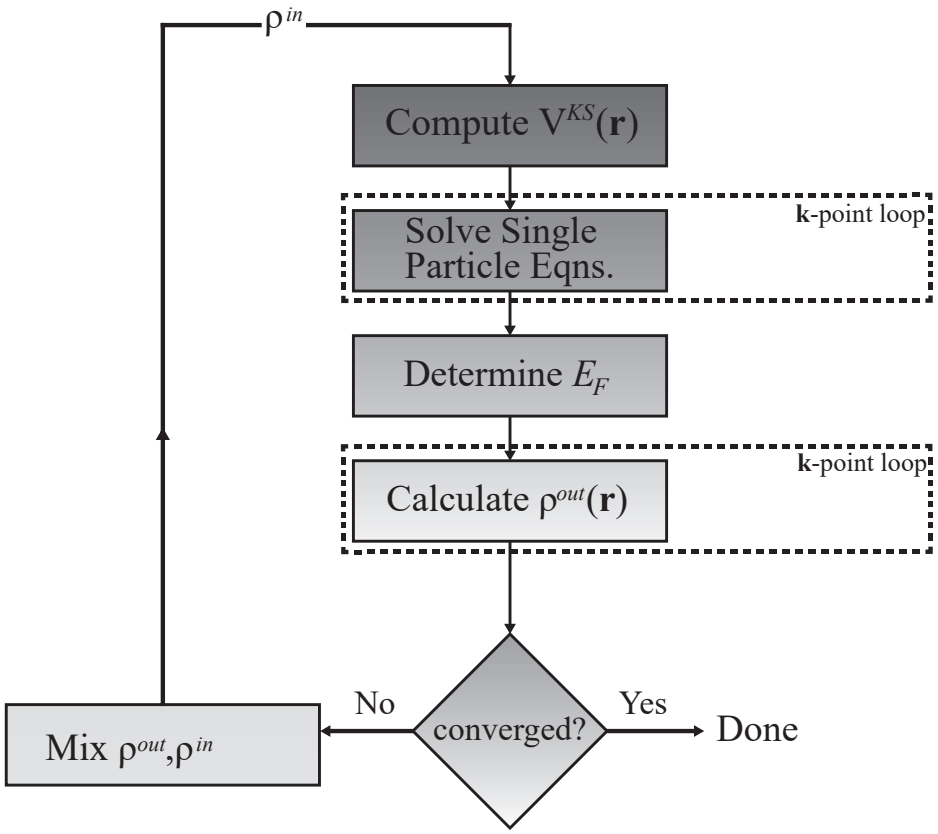

Figure 2.1: Schematic flow-chart for self-consistent density functional computations. Image credit: A. Rubí-González

Chapter 3

Modeling the ternary chalcogenide Na_2MoSe_4 from first-principles

3.1 Introduction

In recent years, a class of ternary chalcogenides known as alkali-metal(ion) transition-metal (and post transition metal) chalcogenides have presented a new landscape of opportunities in solid-state physics and chemistry. These materials, with general composition AMX_n where A is an alkali metal, can be obtained by facile solid-state reactions or by intercalation of a A^+ in a MX_n lattice [**22**]. This, and the fact that they are well known ionic conductors, make them an attractive class of inorganic compounds [**23**, **24**]. In this scene, Kanatzadis and coworkers have shone light on the fundamental chemistry of these compounds, discovering systems as different as semi- and superconductors [**25**, **26**]. Regarding alkali metal transition selenides, partirularly, we highlight the discovery of the layered metal $NaCu_6Se_4$ with mixed valency [**27**], the mixed-valent two-dimensional metal $NaCu_4Se_3$ [**28**] and the two-dimensional metal $NaCu_4Se_4$, which presents high hole mobility and giant magnetoresistence [**29**].

On another note, AMX_n semiconductors are also gaining traction. In 2018, Z. Xia *et al* [**30**] have discussed the chemistry of a new alakali-transition metal chalcogenide, $CsCu_5Se_3$. This caesium copper selenide, grown via the solvothermal method, is a pseudo-direct bandgap semiconductor with a bandgap of 1 eV. It crystallizes in the *oP* lattice, space group *Pmma* (No. 51). Authors also explored the complete family of materials by synthesizing and characterizing $CsCu_5S_3$ and proposing $CsCu_5Te_3$. Since then, α-$CsCu_5Se_3$ has been achieved and proposed as a high-performance thermoelectric [**31**] and an *ab-initio* study treats the defect physics in $CsCu_5Se_3$ and its potential in optoelectronics [**32**]. In a recent review on chalcogenides for photovoltaic applications, $CsCu_5Se_3$ and other new chalcogenides are compared to their oxide analogs [**33**], to highlight opportunities for new materials.

Recent advances worth highlighting the emergence of a new class of transition metal chalcogenide pervoksites. The interplay between alkali-metal (A^+) and MX chemistry promises solar-cell absorbers with electronic properties on a par with those of Hybrid perovskites [**34**, **35**, **36**]. One of the major advantages of TMC perovskites is its high resistance to decomposition [**37**, **38**, **39**], as well as their malleable compositional, structural and electrical and optical properties.

Here, we aim to model Na_2MoSe_4 (See Fig. S1), a molecule chemically analogous to the well known sodium molybdate (Na_2MoO_4) [**40**], in the solid state. The following question arises: what will be the crystal structure of Na_2MoSe_4? The answer is not obvious, as molecular Na_2MoSe_4 is as related to Na_2MoO_4 as it is to Cs_2WS_4 [**41**]. Upon modeling Na_2MoSe_4, we will gain insight into the physics of its crystalline relatives. To this end, we employ a crystal structure (CS) prediction method combined with Kohn-Sham Density Functional Theory (DFT) to determine the ground state properties of this alkali metal transition metal chalcogenide. Our CS prediction is based on the generation of hypothetical candidates through the ionic substitution of experimentally known analogs of Na-Mo-Se compounds. We demonstrate that Na_2MoSe_4 is a direct bandgap semiconductor with simple orthorhombic (*oP*) CS, *Pnma* space group.

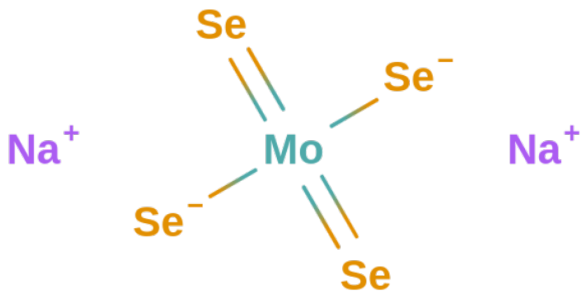

Figure 3.1: Illustration of the Na_2MoSe_4 molecule. Image generated with MolView.

3.2 Objectives

- Generate a set of hypothetical crystal structures (candidates) based on compounds chemically analogous to Na_2MoSe_4 registered in the ICSD.
- Approximate the ground state volume of the selected candidates through isotropic expansion(compression).
- Identify the energetically favored crystal structure for Na_2MoSe_4 through DFT-based thermodynamics.
- Model the electronic band structure of Na_2MoSe_4 at a predictive level.

3.3 Computational Methods

3.3.1 Crystal Structure Prediction

To address the issue of structure determination, we followed the crystal structure prediction method of Hautier *et al* [**42**, **43**] based on data mined ionic substitutions. It has been demonstrated that the method of data mined ionic substitutions can generate likely crystal structures at a fraction of the computational cost of evolutionary algorithms [**44**], due to the fact that the substitutions are

generated posterior to the analysis of existing crystal structures listed in the ICSD. Here, we briefly summarize the DM+IS methodology:

(i) In Eq. (3.1) systems of ions X_i $(i = 1, 2, 3, ..., n)$ are represented as a component vectors of n elements,

$$\mathbf{X} = (X_1, X_2, X_3, ..., X_n). \tag{3.1}$$

(ii) Once a given number of candidate structures is generated, the probability function P_n for two compounds existing in the same crystal structure is expressed as

$$P_n(\mathbf{X}, \mathbf{X'}) = P_n(X_1, ..., X_1', ..., X_n'). \tag{3.2}$$

(iii) p_n is approximated by using the feature function $f(\mathbf{X},\ \mathbf{X'})$, as shown in Eq. (3.2)

$$P_n(\mathbf{X},\ \mathbf{X'}) \approx \frac{\exp[\sum_i \lambda_i f_i(\mathbf{X},\mathbf{X'})]}{\Xi} \tag{3.3}$$

(iv) In Eq. (3.3), Ξ is analogous to a partition function that ensures normalization of P_n, and λ_i is the weight corresponding to $f_i(\mathbf{X},\mathbf{X'})$. It is noteworthy that only binary feature functions $f_i(\mathbf{X},\mathbf{X'})$ are assigned to pairs of ions (α, β),

$$f_k^{\alpha,\beta}(\mathbf{X},\mathbf{X'}) = \begin{cases} 1, & X_k = \alpha, X_k' = \beta. \\ 0, & else. \end{cases} \tag{3.4}$$

(v) The likelihood of the binary α to β substitution is determined by λ_i, obtained from ionic compounds in the ICSD. For a detailed description of DM+IS method and its reach, we refer the reader to the paper by Ceder and coworkers [**42**].

Our DM+IS search generated over sixty-five hypothetical sodium molybdenum selenide structures, of which twenty-one present our hypothesized stoichiometry. The list of Na_2MoSe_4 candidates

is found in Table S1 along with other hypothetical Na-Mo-Se structures have been made public in the Materials Project Database [**45**] and can be downloaded directly from our repository [**46**]. Here, we focus our attention to the four candidates with highest likelihood of existing in their predicted space groups.

3.3.2 Density Functional Theory Computations

Our first-principles computations based on Kohn-Sham Density Functional Theory (DFT) were carried out in the Quantum ESPRESSO package [**47**, **48**]. We employ the Generalized Gradient Approximation (GGA) functional with corrected-for-solids Perdew-Burke-Ernzerhof (PBEsol) parametrization for the exchange-correlation interactions [**49**]. It has been shown that the PBEsol is better suited to approximate lattice constants and surface energies when compared to PBE and LDA [**50**, **51**, **52**]. The ground state structures were determined by varying the volume isotropically, to control symmetry while fully relaxing atomic positions under a tolerance of 13.605×10^{-5} eV/atom for total energy and net forces of 0.025 eV$\cdot$Å^{-1} per atom. These computations were performed using ultrasoft pseudopotentials (USP)[**53**] with a plane-wave kinetic energy cutoff of 40 Ry (544 eV), charge density cutoff of 320 Ry (4,354 eV) and a convergence threshold of 1×10^{-8} eV for self-consistency. Longe-range Grimme D2 Van der Waals interactions were included [**54**]. Monkhorst-Pack Γ-centered integration grids were used to sample the first Brillouin Zone [**55**]. For structural optimization computations of the cF, oF, oP and mC phases, integration grids of $6\times6\times4$, $8 \times 6 \times 5$, $6 \times 8 \times 4$, $5 \times 5 \times 4$ were used, respectively. To model the electronic structure we then increased the density of the k-points integration grids to $24 \times 28 \times 20$ (cF), $32 \times 24 \times 20$ (oF), $24 \times 32 \times 18$ (oP) and $30 \times 30 \times 24$ (mC). The USP used in all pw-DFT computations were generated with the following valence configurations: Na ($2s^1$, $3s^2$, $2p^2$), Mo ($4s^1$, $5s^2$, $5p^2$, $4d^5$) and Se ($4s^1$, $4p^2$, $3d^3$).

The Generalized Gradient Approximation fails to predict the fundamental bandgap of semiconductors. Therefore, we then model the electronic band structure of the favored phase by performing

meta GGA calculations using the Trahn-Blaha modified Becke-Johnson (TB-mBJ) exchange potential [**56**, **57**, **58**]. In order to obtain optimal results, our TB-mBJ computations were carried out in the framework of the Augmetnted Planewave plus Local Orbital (APW+lo) method as implemented in the all-electron code Wien2k [**58**]. The TB-mBJ exchange potential reads

$$\mathbf{v}_{x,\sigma}^{TB-mBJ}(\mathbf{r}) = c\mathbf{v}_{x,\sigma}^{BR}(\mathbf{r}) + (3c-2)\frac{1}{\pi}\sqrt{\frac{5}{12}}\sqrt{\frac{2t_\sigma(\mathbf{r})}{\rho_\sigma(\mathbf{r})}} \tag{3.5}$$

where ρ_σ is the electronic density, t_σ is the kinetic energy density and $\mathbf{v}_{x,\sigma}^{BR}(\mathbf{r})$ is the Becke-Roussel potential.

3.4 Results

3.4.1 Candidate structures

Table 3.1: Predicted and optimized lattice parameters for the Na_2MoSe_4 candidate structures computed at the GGA-(PBEsol) level of theory.

System	**a** (Å)	**b** (Å)	**c** (Å)	V (Å^3)	α	β	γ
cF: *Fd-3m* (227)							
DM+IS	6.44	6.44	9.11	188.89	45	45	90
This work	8.14	8.14	11.51	238.76	45	45	90
oF: *Fddd* (70)							
DM+IS	6.31	8.39	10.85	223.77	130	149	56
This work	7.71	10.24	13.26	273.38	130	149	56
oP: *Pnma* (62)							
DM+IS	9.32	6.84	12.08	770.49	90	90	90
This work	9.12	6.69	11.81	753.92	90	90	90
mC: *C2/m* (12)							
DM+IS	6.88	6.08	7.54	254.92	90	67	63
This work	7.78	6.88	8.52	368.58	90	67	63

The structures considered in detail are: a face centered cubic (cF) phase with space group *Fd-3m* (227), a face centered orthorhombic (oF) with space group *Fddd* (70), a primitive orthorhombic (oP) with space group *Pnma* (62) and a base centered monoclinic (mC) with space group *C2/m* (12). The unit cells are sketched in Fig. 3.2 (a)-(d). The structural details for the evaluated systems are shown in Table 3.1, which includes the raw (generated) DM+IS and the computed

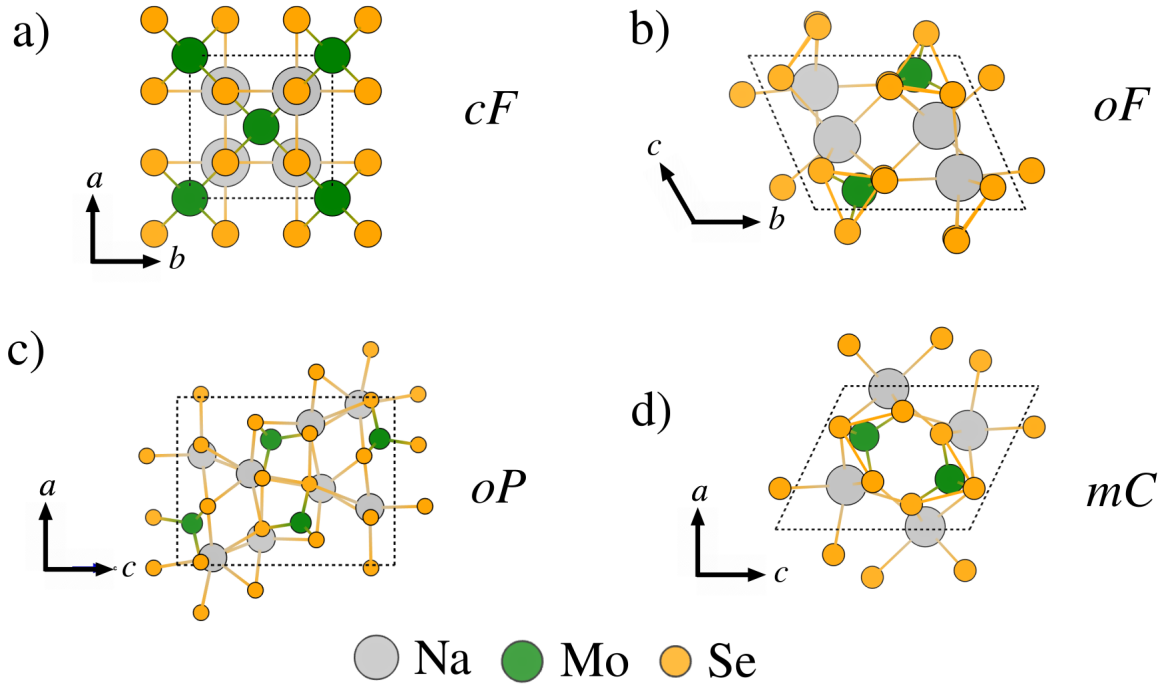

Figure 3.2: Sketch of the candidate structure unit cells under this study for Na_2MoSe_4. The candidates are labeled by their lattice type (a) face centered cubic cF, (b) face centered orthorhombic oF, (c) simple orthorhombic oP and (d) base centered monoclinic mC. The colors corresponding to Na, Mo and Se are grey, green and orange respectively.

(equilibrium) parameters. From the obtained results it is clear that the equilibrium volume changes significantly with respect to the DM+IS volume, with the exception of the oP structure. For example, $\Delta V^{oP} = 2\%$ versus $\Delta V^{cF} = 26\%$. Since we have unit cells with different number of atoms, to formally asses which of the candidates is the favored ground state phase of Na_2MoSe_4, we proceed to calculate the formation enthalpy $\Delta H^s_{f(AMX)}$. Thus, Eq. (3.6) reads

$$\Delta H^s_{f(AMX)} = U^s_{(AMX)} - \sum_i^3 N_i \mu^s_i, \tag{3.6}$$

where $U^s_{(AMX)}$ is the total energy of our ternary compound, N_i is the number of atoms of a constituent i with chemical potential μ_i in solid phase.

Explicitly for Na_2MoSe_4, this is:

$$\Delta H^s_{f(Na_2MoSe_4)} = U^s_{(Na_2MoSe_4)} - \left(2\mu_{Na} + \mu_{Mo} + 4\mu_{Se}\right) \tag{3.7}$$

The chemical potentials μ for the constituent species were calculated based on DFT energies of their equilibrium crystal structures under the same relaxation criteria and convergence thresholds as the Na_2MoSe_4 candidates. Additionally, analysis was cross-checked by fully relaxing all candidate structures at the PBE level. No significant changes on the lattice parameters were found. The values for $\Delta H^s_{f(AMX)}$ are shown in Table 3.2. Note that oP is the favored phase of the selenide with ΔH^s_f values of -5.14 (PBEsol) and -5.11 (PBE) eV per formula unit (eV/f.u.). We find these relative formation enthalpies to be in good agreement, as the relative error between the PBE/PBEsol calculations is less than 2% for all phases with the exception of the least stable cF, in which a larger discrepancy is observed. This is reminiscent of the Cs pervoskite $CsPbBr_3$, where through cooling, it undergoes a transition from a cubic to an orthorhombic lattice [**59**]. We encourage further studies to calculate the phonon band structure for the meta-stable phases, as we recognize the importance of these calculations to assess its dynamical stability. Here, our scope is to determine the most energetically stable structure for the already synthesized Na_2MoSe_4 compound [**60**], and calculate its electronic properties. Once the most stable phase is determined, we focus our attention only to the oP phase with $Pnma$ space group. To further cross check the ground state of the $Pnma$ candidate, we take the initial (DM+IS) structure and optimize it at the APW+lo/PBEsol level of theory.

The calculated lattice parameter is $a = 9.21$ Å, which is in agreement with our pseudopotential computed lattice constant $a = 9.12$, with an absolute error $e_a =\leq 1\%$. At V_0, the bulk modulus for Na_2MoSe_4 is $B_0 = 56.07$ GPa with a numerical derivative of $B'_0 = 4.41$.

Due to the fact that the hypothetical crystal structures were generated from chemical analogs, it is reasonable to infer that the true equilibrium structure of our material (oP) should result

Table 3.2: Formation enthalpies ΔH_f for Na_2MoSe_4 candidate structures calculated from GGA(PBEsol) and GGA(PBE) computations. ΔH_f si shown in eV per formula unit (eV/f.u.) and eV/atom.

System	ΔH_f (eV/f.u.)	ΔH_f (eV/atom)
cF		
PBEsol	-4.39	-0.63
PBE	-4.02	-0.57
oF		
PBEsol	-4.90	-0.70
PBE	-4.83	-0.69
oP		
PBEsol	-5.14	-0.73
PBE	-5.11	-0.73
mC		
PBEsol	-5.03	-0.72
PBE	-4.91	-0.70

isostructural to other materials governed by same chemical principles (e.g. valency, electronegativity, position within the periodic table etc.). Furthermore, it is inferred that compounds governed by the same chemical principles as Na_2MoSe_4 will also be favored in the oP lattice. This is in fact the reasoning and strength behind probabilistic models for crystal structure prediction [**61**, **62**, **63**]. Therefore, the probability P of a material to exist in a specific crystal system (e.g. oP ($Pnma$)) will be influenced by the size of the known isostructural family [**64**, **65**, **66**, **67**, **68**, **69**]. We match our evaluated structures to their analogs. First, we found our least stable candidate $cF(Fd-3m)$ to be isostructural to the stable phase of Na_2MoO_4 [ICSD No. 44523]. The metastable phase of Na_2MoO_4 [ICSD No. 151971] is characterized by the $Fddd$ space group and isotructural to our oF candidate. The mC candidate is isostructural to the molecular crystal K_2MoO_4 [ICSD No. 16154]. Lastly, our most stable oP phase is isostructural to (or based on) K_2MoS_4 [ICSD No. 409563]. Notably, the following isostructures have been synthesized: Na_2MoSe_4 with $oP(Pnma)$ symmetry: K_2MoS_4, Cs_2MoSe_4, Rb_2MoSe_4, Cs_2MoS_4, Rb_2MoS_4, K_2WSe_4 and Rb_2WS_4 [**64**, **65**, **66**, **67**, **68**, **69**] and could potentially be intrinsic semiconductors. Additionally, hybrid organic/inorganic members of the family R_2MX_4 (e.g. R = CH_3NH_3 ; M = Mo,W ; X = S, Se) have also been reported [**68**, **69**]. Note, throughout the A_2/R_2MX_4 family, X is either S or Se. To the best of our knowledge, no

theoretical studies of these materials are available in the literature. Given the electronic structure of Na_2MoSe_4 and τ_4 (see section VI), it results of interest to the broader community to understand the physics and chemistry of the oP A/R_2MX_4 compounds and their potential applications. Hence, we intend for our work to serve as a premier for future theoretical and experimental studies on the structural and electronic properties of both the inorganic and hybrid organic-inorganic analogs of Na_2MoSe_4. With respect to the question posed in the introduction; in the solid-state, the stable phase of Na_2MoSe_4 is isostructural to Cs_2WS_4 (oP) and not Na_2MoO_4 (cF).

3.4.2 Structure and symmetry of orthorhombic sodium molybdenum selenide

The disodium molybdenum tetraselenide, which can be written as $Na[MoSe_4]$, is a molecular crystal favored to grow in the simple orthorhombic (oP) crystal system with space group *Pnma* (No. 62), as shown in Fig. 3.3. It has inversion symmetry, with eight symmetry operations. In Figure 2-a, an illustration of the frontal and isometric views are shown. The Na_2MoSe_4 structure is three-dimensional, (i.e. there are no van der Waals gaps) with two equivalent Na^{1+} sites. Note that Mo^{6+} is in tetrahedral coordination τ_4 (i.e. $\tau_4 = 1$), bonded to four Se^{2-}atoms at each vertex. There is no Mo-Na bond, and the Na cations are intercalated throughout the lattice. This promotes the one-dimensional (directional) growth of the $[MoSe_4]^-$ tetrahedrons. Hence, $MoSe_4$-terminated slabs can be achieved for Na conduction. Additionally, the electronic charge of Na induces a distortion in the tetrahedron (distortion index $t_4^{'} = 0.006$) yielding a slightly elongated Mo-Se bond ($d = 2.33$ Å) versus the other three ($d = 2.30$ Å), and a broadening of Se-Mo-Se bond angle ϕ from $\phi = 109.55°$ to $\phi = 115°$ as shown in Figure 2-b. The average Mo-Se bond length is $\bar{l} = 2.31$ Å. This distortion is caused by electronic charge effects of a Na^{1+} atom in proximity to one Se vertex ($r = 2.98$ Å). The distortion can be also measured by the tetrahedron edges, conformed by Se-Se inter-atomic distances. The tetrahedron edge lengths are $l = 3.778$, 3.576 and 3.793 Å respectively. The omitted length values are redundant in nature. A spread of Na-Se bond distances can be found in the two Na

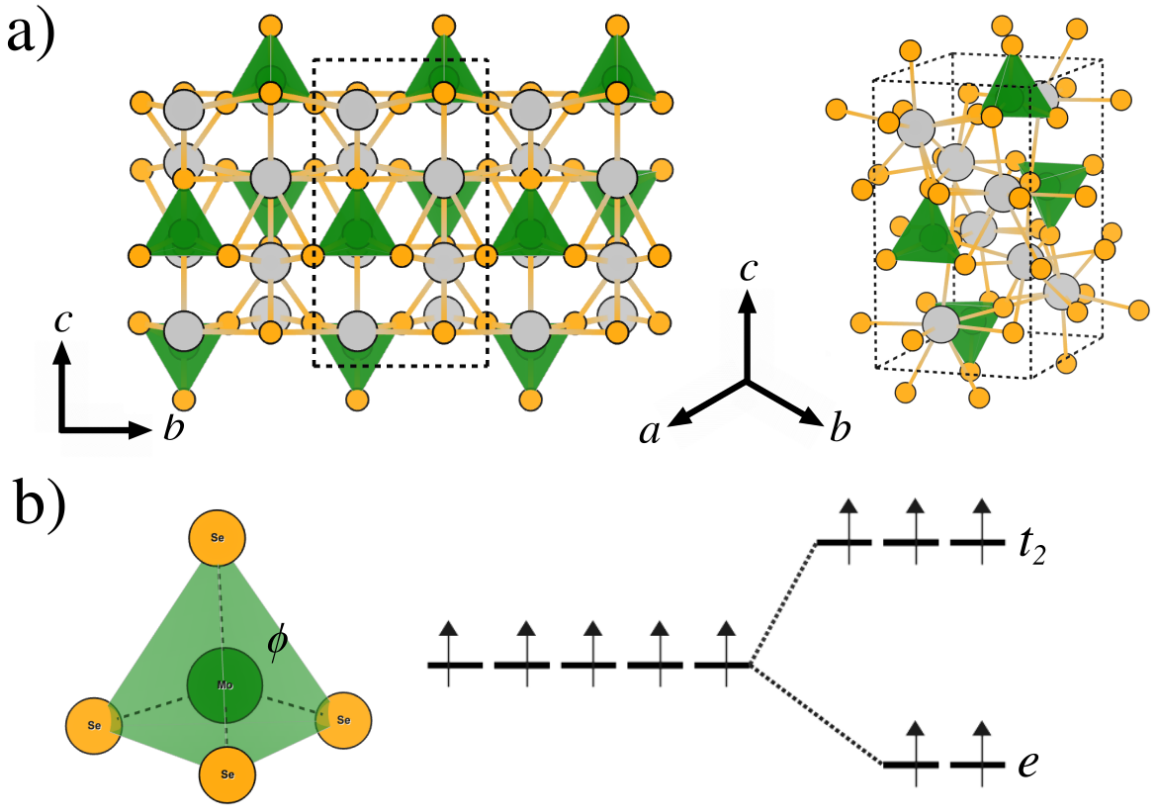

Figure 3.3: Illustration of (a) isometric and front views of *oP* (*Pnma*) phase of Na_2MoSe_4 and (b) the $[MoSe_4]^-$ tetrahedron with a schematic illustration of the tetrahedral crystal field that splits the Mo $4d_5$ orbitals into two groups, namely t_2 and e. As seen in (a) Na^+ ions are intercalated through the $MoSe_4$ tetrahedral layers.

sites, with values ranging between 2.98 – 3.48 Å. In one Na^{1+} site, Na^{1+} is bonded in a 8-coordinate geometry to eight Se^{2-} atoms. In the other, our sodium cation is bonded in a 9-coordinate geometry to 9 Se anions. There are three nonequivalent Se^{2-} sites. In the first Se site, Se^{2-} is bonded in a single coordinate geometry to four Na^{1+} and one Mo^{6+} atom. In the second site, Se^{2-} is bonded in a 6-coordinate geometry to five Na^{1+} and one Mo^{6+} atom. In the third Se site, Se^{2-} is bonded in a 5-coordinate geometry to four Na^{1+} and one Mo^{6+} atom. Our structural analysis is in agreement with the available information for its reported analogs [**64**, **65**, **66**, **67**, **68**, **69**]. Note, the intercalation of Na atoms could favor an energetically low-cost substitution (or displacement) of cations, enabling the tunability of these materials' properties. Lastly, due to the structure of $Na^+[MoSe_4]^-$, it can be

safely inferred that the crystal is a typical ionic conductor [**65**].

3.4.3 Electronic structure

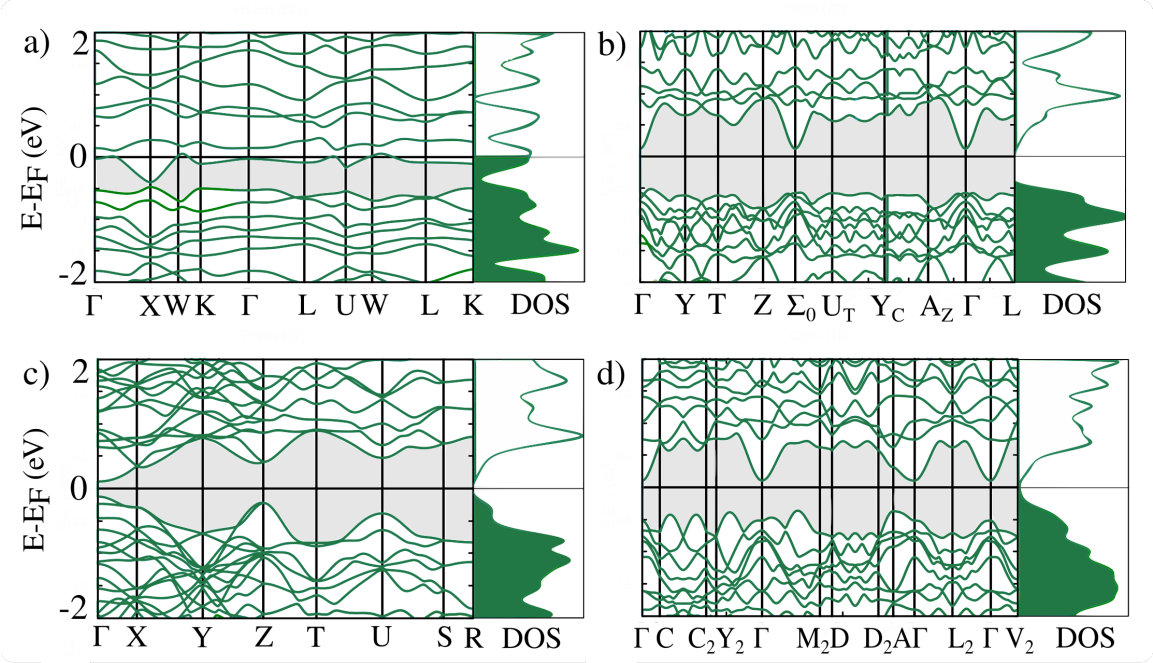

Figure 3.4: The electronic band structure and total density of states is shown for the (a) cF, (b) oF, (c) oP and (d) mC candidate phases of Na_2MoSe_4. The Fermi energy E_F is set to 0.

The electronic structure of all candidates was investigated. Fig. 3.4 depicts the electronic band structure of the candidate phases of Na_2MoSe_4. Conventional k paths were used [**70**, **71**]. In all plots, the Fermi energy (E_F) is set to zero. From the band structure plots, it is clear that one of four phases is semi-metallic; cF (Figure 3(a)), where the valence band slightly crosses the Fermi level. The remaining three are intrinsic semiconductors. The oF phase is a direct bandgap semicondutor (Figure 3 (b)), with a bandgap $E_g = 0.62$ eV at Γ, while the mC phase is an indirect bandgap ($A - \Gamma$) semiconductor with $E_g = 0.45$ eV (Figure 3(d)). Lastly, our GGA calculations show that oP Na_2MoSe_4, the stable phase, has a fundamental bandgap of $E_g^{GGA} = 0.24$ eV at Γ (Figure 3 (c)). A summary of the electronic properties computed at the GGA level is displayed in table 3.3

Since the oP structure is energetically favored, we focus only on this phase from here in and shall

Table 3.3: Band structure summary with E_g values at the GGA level of theory. To classify the phases, metals are identified by M, while D and I are employed to label direct and indirect semidoncutors. The labels k_c and k_v correspond to the points at the CBM and CVM respectively.

System	E_g^{GGA} (eV)	E_g Type	$k_c - k_v$
cF	0.00	M	$---$
oF	0.62	D	$\Gamma - \Gamma$
oP	0.24	D	$\Gamma - \Gamma$
mC	0.45	I	$A - \Gamma$

refer to this phase simply as "Na_2MoSe_4".

In order to better understand the electronic band structure of Na_2MoSe_4, we adopt an alternative k path from the work of Xia *et al*[**30**] on *oP* $CsCu_5Se_3$. Note that its band dispersion is highly isotropic with clear parabolic topology at the VBM and CBM around the Γ point. Moreover, as an ionic conductor [**23**], it can be considered as a mixed conductor.

At this point, we analyze the nature of the Na_2MoSe_4 band structure. Let us recall that the Mo $[d^5]$ is in coordination τ_4 with Se $[4s^2 4p^4]$ atoms at each vertex. Given the electronic nature of our species, it is inferred that the valence bands that contribute to the E_F are composed of Se p orbitals, with mild hybridization with the Mo d orbitals. The s, p hybridization of the Mo-Se bond is common in high-spin τ_4 compounds (see Fig. 3.3. Therefore, it can be said that the electronic (semiconducting) properties of the material arise mainly from the $[MoSe_4]$ sub-unit and that the effects of Na s, p electrons are negligible. However, although Na doesn't influence the band structure of the selenide, it is reasonable to believe that the displacement of Na throughout the lattice or its substitution by another ion (or molecule) could have an effect on the value of E_g. We further investigate the τ_4 sub-unit by treating the Se atoms as point charges around the Mo central ion, to study their bonding strength in terms of Coulombic interactions. In this sense, Crystal Field Theory (CFT) qualitatively predicts how the electrons in the Mo $4d$ orbitals respond to the effective electrostatic potential imposed by its neighboring Se atoms. In τ_4, the initial five-fold degeneracy of the $4d$ orbitals will break. This will give rise to the the orbital groups t_2 orbitals (d_{xy}, d_{yz}, d_{yz}) and the e orbitals $(d_{x^2-y^2}, d_{z^2})$. A schematic illustration of an idealized τ_4 CF is shown in the right

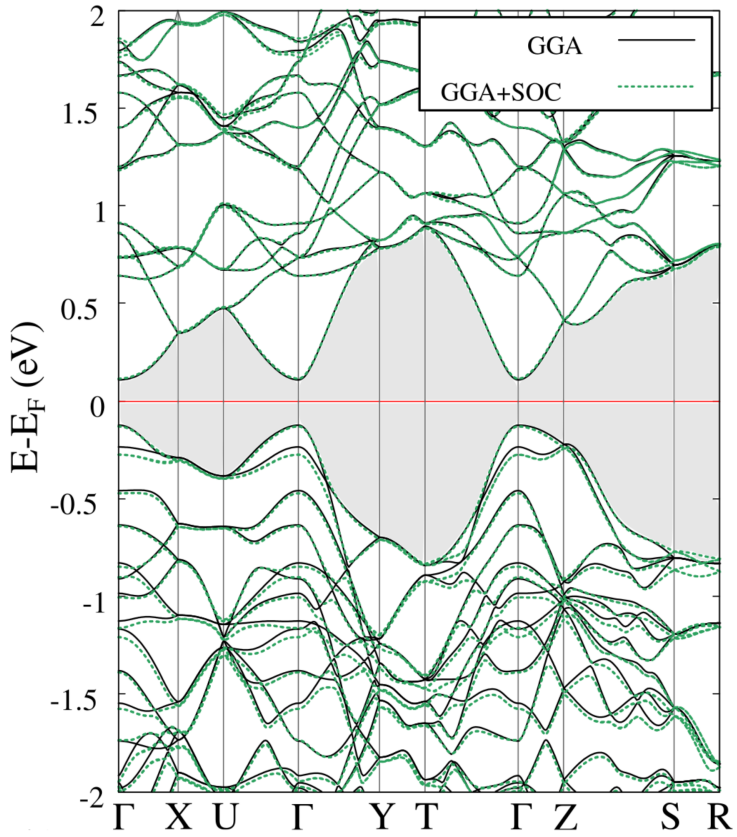

Figure 3.5: Electronic band structure is shown in (a) modeled at the GGA (black - solid) and GGA+SOC (green - dashed) levels with $E_g = 0.24$ eV. The irreducible Brillouin zone and k-path for the oP lattice is shown in (b). The CVM-VBM region is shown along the $U - \Gamma - Y$ path computed with the TB-mBJ potential in (c). Note that at the TB-mBJ level, $E_g = 0.53eV$.

hand side of Figure 2(b). The qualitative CFT analysis indicates that spin orbit coupling (SOC) effects in Na_2MoSe_4 are weak [**72**].

Considering the electronic configuration of Mo ($[Kr]4d_5 5s_1$), there is only one unpaired electron occupying each d orbital. As a consequence, this along with weak overlap between the Mo d and Se p orbitals leads to high-spin behaviour. We then perform full-relativistic calculations to model the band structure. To see effects of SOC effect on the band structure, we adopt an alternative path of integration along the FBZ. The band structure of Na_2MoSe_4 with and without SOC $\Gamma \rightarrow X \rightarrow U \rightarrow \Gamma \rightarrow Y \rightarrow T \rightarrow \Gamma \rightarrow Z \rightarrow S \rightarrow R$ k-path (Figure 3.5). The FBZ is shown in Figure 4

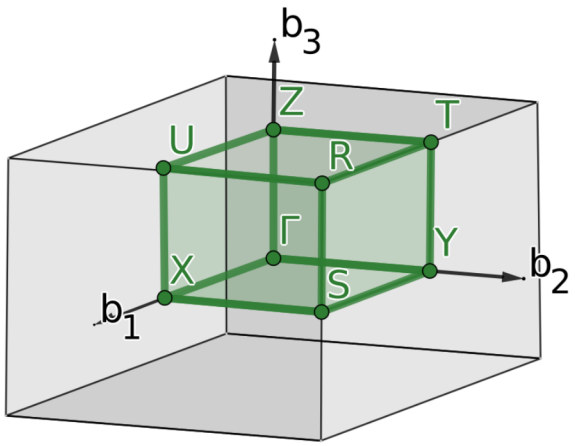

Figure 3.6: Illustration of the Brillouin zone of the *oP* lattice.

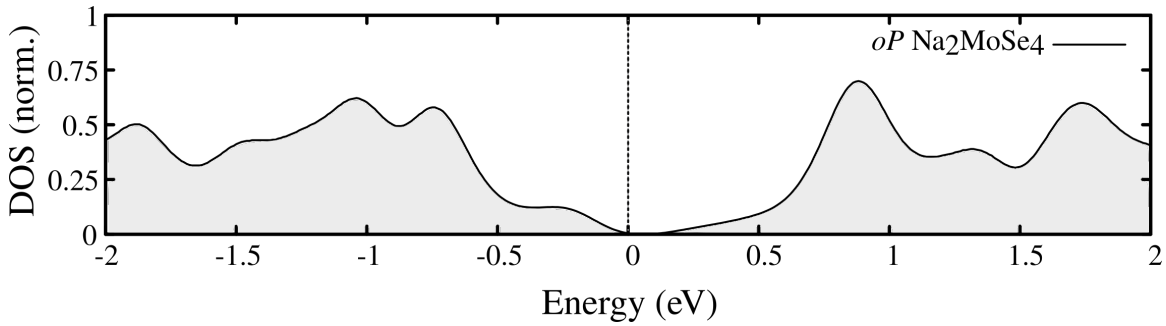

Figure 3.7: Total density of states of *oP* Na_2MoSe_4 near the Fermi level; E_F is set to zero.

(b). As expected, no change was observed in E_g upon calculating the band structure confirming the weak (essentially null) SOC effect. As we have seen, Na_2MoSe_4 has relatives where the A^+ cation is either Rb or Cs. Therefore, although SOC is weak in the Na member of the family, it is necessary to account for relativistic effects when modeling the band structure [**59**].

For completeness, we also plot the band structure by introducing an empirical Hubbard potential (GGA+U ; $U = U_{eff} = 3.5$ eV [**73**]) to test for Coulomb effects in Mo d electrons (see Supplementary Information, Fig. S3.). No significant change was found as well, so there is not an apparent strong electronic correlation in the Na_2MoSe_4 structure.

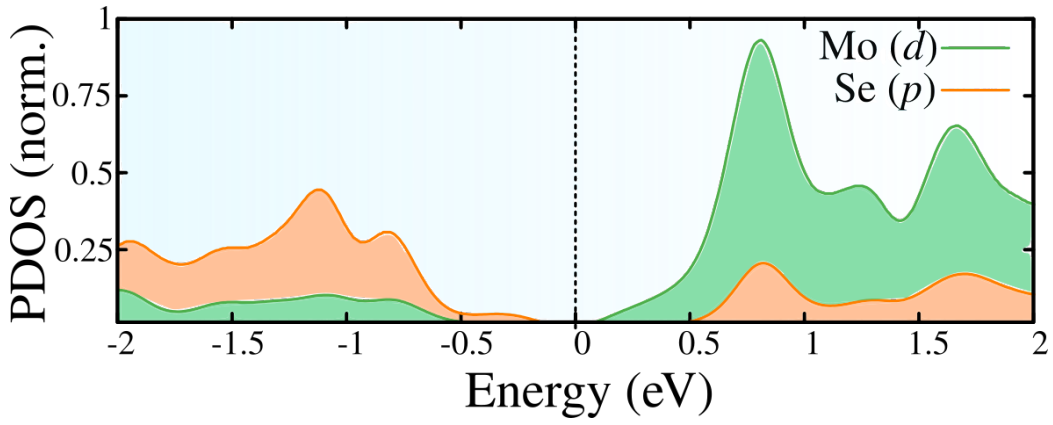

Figure 3.8: Projected density of states of *oP* Na_2MoSe_4 decomposed into Mo *d* orbitals and Se *p* orbitals. From the figure, it is clear that *p* states (bonding states) compose the majority of the valence band while the *d* (antibonding) states compose the conduction band. E_F is set to zero.

In Fig. 3.8, the projected DOS (PDOS) is shown for the Mo *d*, Se *p* and Na *s* electrons. Clearly the Na *s* states do not contribute near the Fermi level. The hybridized *d*/*p* orbitals; Mo *d* states (note $0 \leq E_F \leq 2$ eV) and the Se *p* states are the ones dominating the contributions around the Fermi level. In other words, in the vicinity of E_F, the orbital composition of the conduction bands are Mo *d* while the valence bands are Se *p*. Note that higher PDOS is observed above the Fermi level, due to the unoccupied states in the shells. A decomposition of the summed Mo *d* orbitals can be found in the supplemental material.

Although ground state GGA computations can provide a reasonable first approximation to model the electronic structure of a material, they systemically fail to predict the fundamental value of E_g. Hence, a precise approach such as the use of meta-GGA, hybrid functionals or the many-body perturbation theory method *GW* is desired. To achieve a predictive level, we have opted for the Meta-GGA, Trahn-Blaha modified version of the Becke-Johnson potential (TB-mBJ), designed and proven to yield robust results comparable to experimental results [**56**, **74**, **75**, **76**, **77**]. In the present scenario, the use of TB-mBJ is considered adequate as no further corrections for correlation or spin-orbit coupling are are needed (since the band topology and E_g do not change).

The band structure of *oP* Na_2MoSe_4 calculated with the semilocal potential TB-mBJ is shown

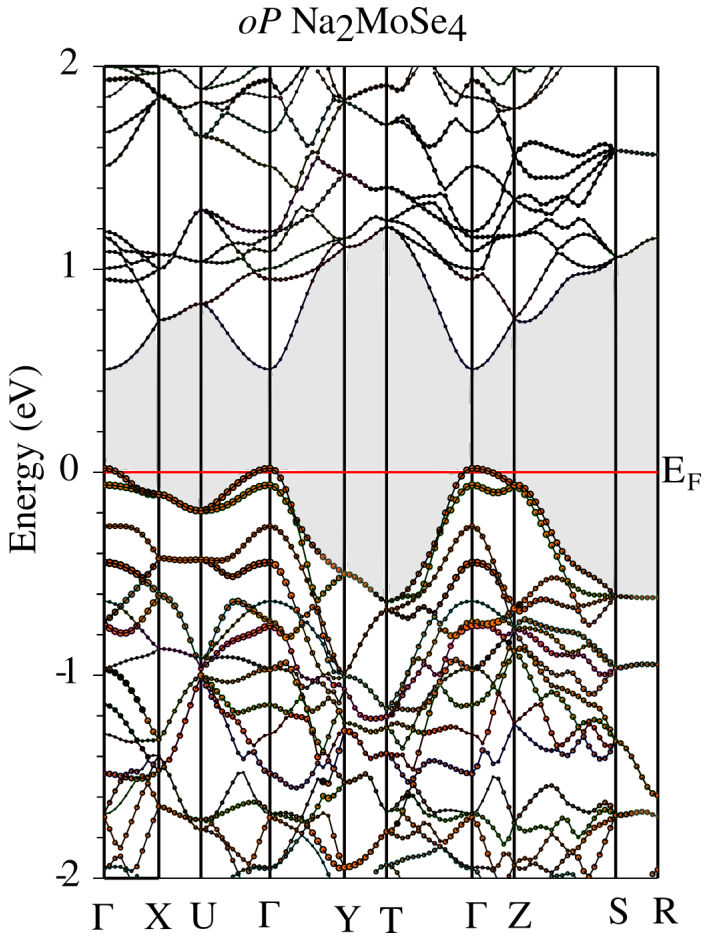

Figure 3.9: Electronic band structure of Na_2MoSe_4 modeled with TB-mBJ. Band composition is distinguished between Se p bands (valence) and Mo d bands (conduction) by point-size. Note that the band-topology is preserved with respect to GGA.

in Fig. 3.9. Note that the band topology is invariant and located at Γ (Figure 3.5), but a widening of the bandgap is observed. When modeling the electronic band structure of Na_2MoSe_4 with the modified Becke-Johnson potential through an all-electron treatment, $E_g^{TB-mBJ} = 0.53$ eV at Γ. The CBs are composed mainly of Mo d states whereas the Se p states dominate the VB contributions, in agreement with the pDOS in Figure 3.8.

Note that the topology of the bands near the CBM and VBM is clearly parabolic (e.g. $U \rightarrow \Gamma \rightarrow Y$) $E(k)$. This indicates that there could potentially be high carrier mobility, with constant effective electron and hole masses, m_e^* and m_h^*, respectively. Therefore, near the CVM / VBM, the dispersion

relation is of quadratic form, i.e. $E = \hbar v_F \mathbf{q} + O[(\mathbf{q}/k^2)]$, where $\mathbf{q} = \Gamma - k$ (finite displacement near Γ) and v_F corresponds to dE/dk, i.e. the Fermi velocity. The effective mass can thus be determined by the second derivative, as

$$m_{ij}^{*-1} = \frac{1}{\hbar}\frac{\partial^2 E(k)}{\partial k_i k_j} \tag{3.8}$$

in units of electron mass m_0. Here, in order to gain insight into the potential transport properties of Na_2MoSe_4, we calculate the electron and hole masses, m_e^* and m_h^*, along the $\Gamma \to X$ (m_{xx}^*), $\Gamma \to Y$ (m_{yy}^*) and $\Gamma \to Z$ (m_{zz}^*) directions. The direction-dependent values are summarized in 3.4.

Table 3.4: Carrier effective masses m_e^* and m_h^* for Na_2MoSe_4 along $\Gamma \to X$, $\Gamma \to X$ and $\Gamma \to X$ ortientations. Calculated from TB-mBJ band structure. Units are per electron mass m_0.

Direction ($\mathbf{q}$)	m_e^* (m_0)	m_h^* (m_0)
$\Gamma \to X$	0.92	0.63
$\Gamma \to Y$	0.16	0.17
$\Gamma \to Z$	0.41	1.32

The expected values for the effective masses are $m_e^* = 0.50m_0$ and $m_h^* = 0.71m_0$, where m_0 is the mass of an electron in SI units, 9.11×10^{-31} kg. In Na_2MoSe_4, highFor your info, the console log starts with:er electron mobility is to be expeceted rather than hole mobility, as evident by the mean effective masses. Also note that the effective masses are anisotropic, with ligther and faster electron quasi-particles moving along the the y direction resulting from the high curvature of the band in this direction. Here, the electron-hole ratio is approximately 1:1, with $m_{e:yy}^* = 0.16m_0$ and $m_{h:yy}^* = 0.17m_0$. Hence, carrier mobility is favored along the y direction. This indicates p-type doping in Na_2MoSe_4 could promote hole mobility along y. Similar electronic anisotropy has been observed in other oP chalcogenides, such as $CsCu_5Se_3$ [**27**].

It is important to point out that TB-mBJ semilocal potential enables the modeling the electronic structures of large and chemically complex semiconducting materials as well as insulators with predictive accuracy [**78**, **79**], and is currently considered the most accurate semilocal potential for semiconductor modeling [**80**, **81**].

Although the bandgap isn't yet "ideal" for applications in traditional optoelectronic devices or

photovoltaics, Na_2MoSe_4 with an intrinsic direct bandgap of 0.53 eV holds potential for applications in infrared optoelectronics and high-speed electronic heterostructures and devices. Since the bandgap is tunable via ionic displacement and/or substitution, a natural interest in studying these effects throughout the lattice rises. More importantly, it will be interesting to build upon the work presented and investigate the interplay between chemical composition, thermodynamic stability and electronic structure in the inorganic and hybrid relatives of Na_2MoSe_4. Expanding on the physics studied here to related systems will be the subject of a forthcoming publication.

3.5 Conclusions

We have presented a theoretical investigation on the alkali-ion transition metal chalcogenide Na_2MoSe_4. First-principles computations based on periodic Density Functional Theory were systematically performed on a set of data-mined hypothetical crystal structures to determine their stability and model their electronic properties. The face centered cubic, face centered orthorhombic, simple orthorhombic and base centered monoclinic phases were studied in detail. The stability analysis reveals that the simple orthorhombic is the favored phase, with space group $Pnma$, therefore Na_2MoSe_4 is isostructural to Cs_2WS_4 and $(CH_3NH_3)_2MoS_4$.

Additionally, electronic structure calculations reveal the semiconducting behaviour for three candidates, while the cubic phase is semi-metallic. The band structure of orthorhombic Na_2MoSe_4 is modeled at the Meta-GGA level of theory with the Trahn-Blaha modified Becke-Johnson exchange, yielding a direct fundamental bandgap of 0.53 eV at Γ. This bandgap makes Na_2MoSe_4 suitable for applications in infrared optoelectronics and high speed electronics, with anisotropic electron mobility in the y direction. Our analysis indicates that the qualitative physics of Na_2MoSe_4 may be transferable to oP chemical analogs, and raises questions regarding the interplay between the composition, energetics and band structure of similar compounds.

Chapter 4

On the band structures of alkali-ion transition metal chalcogenides with *oP* symmetry

4.1 Introduction

Alkali-ion transition-metal chalcogenides are a class of ionic conductors [**22**, **23**] that have recently been classified as suitable candidates for a variety of solid-state devices, both for their physicochemcial properties and their high synthesizability [**21**, **22**, **23**]. The work of Kanatzadis and coworkers in this scence has accelerated the field through the discoveries of Rb^+ and Cs^+ transition and *post*-trantision metal chalcogenide semi- and superconductors [**24**, **25**]. Additionally, Na^+ metal-rich chalcogenides such as $NaCu_6Se_4$ [**26**], $NaCu_4Se_3$ [**27**] and $NaCu_4Se_4$ [**28**] have been obtained and characterized. In 2019, Chen *et al* report that two-dimensional $NaCu_4Se_4$ presents high hole mobility and giant magnetoresistence [**28**].

On par, alkali-ion transition metal chalcogenides have been proposed for applications in optoelec-

tronics, photovoltaics and thermoelectrics. In 2018, Z. Xia *et al* [**29**] have discussed the chemistry of a new alakali-transition metal chalcogenide, $CsCu_5Se_3$. This caesium copper selenide, grown via the solvothermal method, is a pseudo-direct bandgap semiconductor with a bandgap of 1 eV. It crystallizes in the *oP* lattice, space group *Pmma* (No. 51). The authors went beyond the characterization of $CsCu_5Se_3$ and by studying the "missing members" of the family, synthesizing $CsCu_5S_3$ and modeling $CsCu_5Te_3$ using periodic Density Functional Theory. Shortly after, the α-$CsCu_5Se_3$ was proposed as a high-performance thermoelectric material [**30**] and a theoretical study provides insight into the tunability of the optoelectronic response of $CsCu_5Se_3$ through defect physics [**31**]. In a recent review on chalcogenides for photovoltaic applications, there is substantial discussion on the lessons that can be learned and directions that can be sought in the study of chalcogenides like $CsCu_5Se_3$ based on their analogs [**32**].

In our preceding work [**82**], we drew inspiration from the sodium molybdate compound (Na_2MoO_4) and systematically studied it's Selenide analog Na_2MoSe_4. Parting from the $Na_2^+(MoSe_4)^-$ building block, we combined the data-mining ioinic substitution method (DM+IS) with periodic Density Functional Theory (DFT) to determine it's ground state crystal structure and model it's electronic properties. To our surprise, we learned that in the solid state, Na_2MoSe_4 is not isostructural to sodium molybdate which is a face-centered cubic but instead is isostructural to Cs_2WS_4, with a simple orthorhombic structure and *Pnma* space group. By employing the modified version of the Becke-Johnson exchange potential introduced by Tran and Blaha [**56**, **81**], we demonstrated that Na_2MoSe_4 has a direct bandgap of 0.53 eV at Γ. Upon the realization that multiple inorganic compounds of the A_2MX_4 family (A = K^+, Rb^+, Cs^+ ; M = Mo, W ; X = S, Se) and hybrid organic/inorganic (A = CH_3NH_3) crystals have been synthesized and deposited in the ICSD, we became motivated to understand at a theoretical level their fundamental physical properties.

We present a systematic theoretical study of the inorganic members of the A_2MX_4 family. By using first-principles computations based on DFT, we aim to assess the theoretical requirements to accurately reproduce the experimental structures. Additionally, we analyze in detail the interplay

between the chemical composition, stability, band structure and relativistic effects in the compounds.

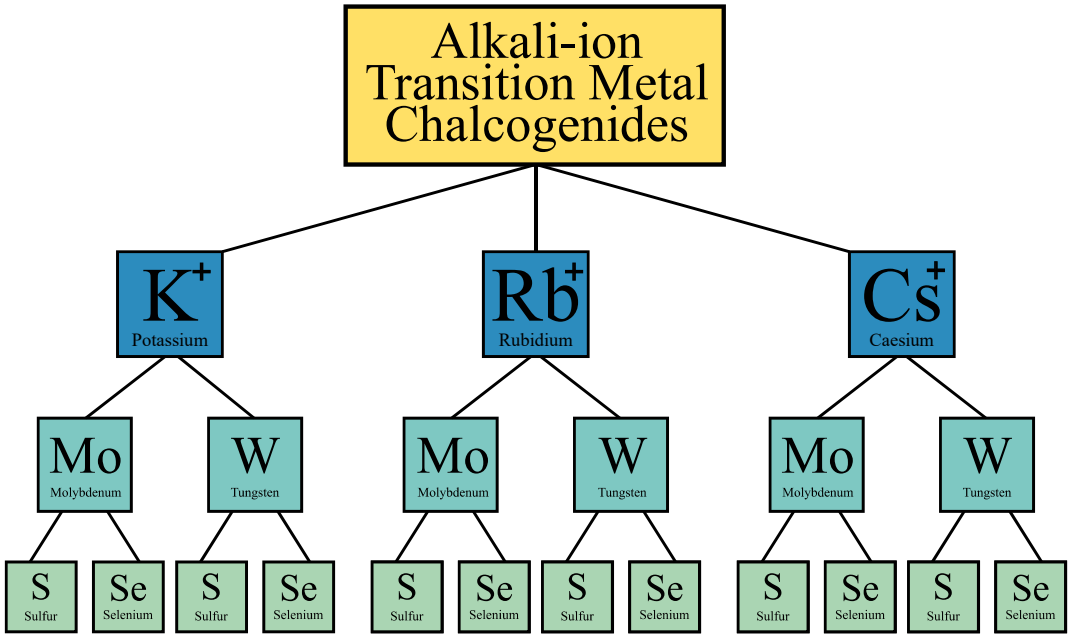

Figure 4.1: Schematics concept map of the alkali-ion transition metal chalcogenides with *oP* symmetry and general composition A_2MX_4. Image credit: A. Rubí-González.

4.2 Objectives

- Identify a suitable theoretical approximation to reproduce the experimental structures of the inorganic A_2MX_4 compounds, then complete the family by predicting the structures of new compounds.

- Model the band structures of the twelve A_2MX_4 compounds.

4.3 Computational Methods

Our computations were carried out within the framework of Kohn-Sham DFT. For our structural analysis, we employ different density functional and pseudopotential approximations. The Local Density Approximation (LDA) and General Gradient Approximation (GGA) functionals were employed. In the case of GGA, the PBE and PBEsol functionals were assessed. These computations were performed using scalar-relativistic (SR) and full-relativistic (FR) optimized norm-conserving Vanderbilt pseudopotentials (ONCVPSP) [**83**, **84**] with a plane-wave kinetic energy cutoff of 90 Ry ($\approx$ 1225 eV), charge density cutoff of 360 Ry ($\approx$ 4900 eV) and a convergence threshold of 1×10^{-8} eV for self-consistency. Long-range Van der Waals interactions were included with the Grimme-D2 method [**54**, **85**]. All computations were carried out in Quantum ESPRESSO [**47**, **48**]. The ground state structures were determined by varying the volume isotropically and atomic positions were relaxed under a tolerance of 13.605×10^{-5} eV/atom for total energy and net forces of 0.025 eV$\cdot$Å^{-1} per atom. Additionally, an alternative approach was taken for structural optimization. Using ultrasoft pseudopotentials (USP) [**53**] to optimize geometries through full-dimensional variation of lattice constants and atomic positions. For these computations, the kinetic energy cutoff was set to 40 Ry ($\approx$ 544 eV). All other parameters remained unchanged. Monkhorst-Pack (MP) k-point integration grids with the origin a Γ were used to sample the first Brillouin Zone [**55**]. The dimensions of the MP integration grids used were $6 \times 8 \times 4$ and $18 \times 24 \times 12$, for geometry optimization and band structure computations respectively.

4.4 Structure and symmetry of alkali-ion transition metal chalcogenides

In general, the A_2MX_4 compounds crystallize in the primitive orthorhombic lattice, with *Pnma* (62) space group. The generic structure is three-dimensional, with two inequivalent A^{1+} sites, coordinated

to nine and eight X^{2-} sites, respectively. The transition metal is in oxidation state M^{6+}, and is bonded in a tetrahedral geometry to four X^{2-} atoms ($\tau = 4$). The A_2MX_4 compound can be seen as two sub-lattices, the main one formed by chains of $[MX_4]$ tetrahedra, with intercalated A atoms. As we have seen with Na_2MoSe_4, there is no direct AM bond, and therefore the $[MX_4]$ sub-unit contributes dominantly to the electronic structure of A_2MX_4. The crystal structure of Cs_2MoS_4 is presented in 4.2 as a prototype of the *Pnma* A_2MX_4.

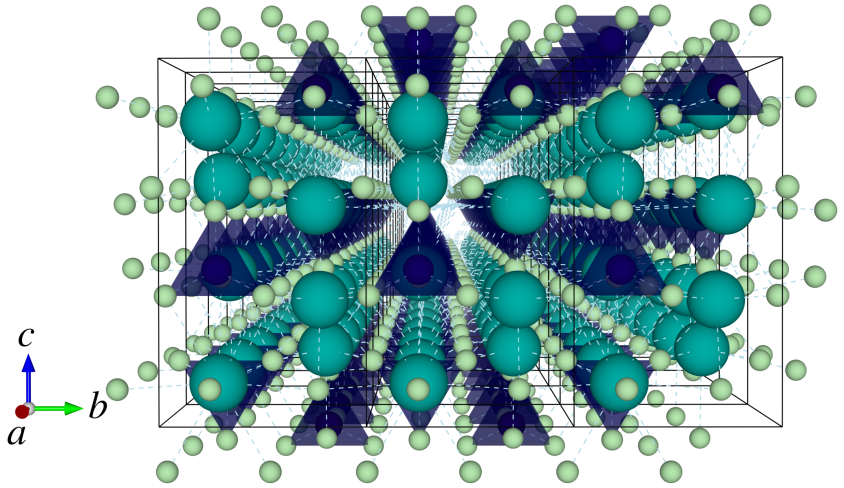

Figure 4.2: Illustration of front view of the extended crystal structure of Cs_2MoS_4 and the *oP* (*Pnma*) A_2MX_4 compounds. The transition metal (navy blue) is in tetrahedral coordination with chalcogen anions at each vertex (pale green). The alkali ion (teal) is in a 10-coordinate geometry with chalcogen. Unit cells are illustrated by a solid black, bonds are indicated by white dotted lines.

The space group *Pnma* is defined by eight general symmetry operations. The corresponding Brillouin zone for the *oP* lattice is shown in 4.3.

4.5 Results

In this work, we employ DFT to compute the electronic structure of the A_2MX_4 compounds, summarized in figure 4.1. In order to characterize the ground state properties of a dozen compounds, standardization of simulation conditions is necessary while guaranteeing that each material is being

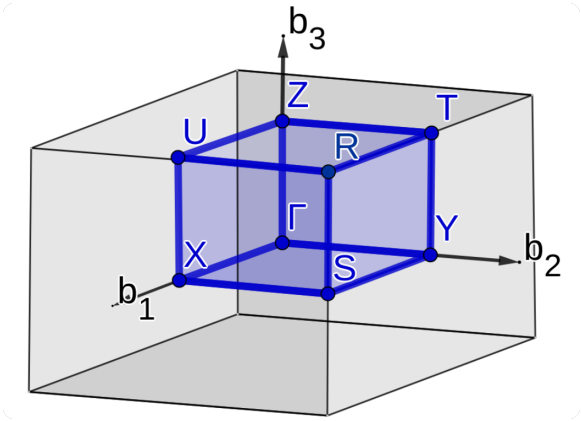

Figure 4.3: Brillouin zone of the *oP* lattice, with irreducible volume shaded in blue with high symmetry points at each vertex. The origin is taken at Γ.

properly modeled. As High-Throughput studies rise in popularity, physical rigor and precision is often sacrificed to compensate (lower) computational cost. One of the most common computational tasks that is often discussed is geometry optimization. In an ideal case, the lattice constants as well as the atomic positions of a system are optimized - i.e. varied in an iterative manner until a global energy and force minima are reached. This task alone can be computationally expensive. Also, taking into account that there is no "perfect" or universal functional, and recalling that DFT computations are athermal (i.e. at $T = 0$ K) and in a vacuum environment, the theoretical ground state may differ from the experimental data.

Table 4.1: Lattice constants for the known A_2MX_4 compounds. The computed structures were obtained by varying the volume isotropically using ONCVPSP for LDA, PBE, PBEsol, PBE-D2 and PBE-D2-SO. We also performed a full-dimensional optimization for PBE-D2 using USP.

Compound	ICSD No.	a (Å) Exp.	a (Å) LDA	a (Å) PBE	a (Å) PBEsol	a (Å) PBE-D2	a (Å) PBE-D2-SO	a (Å) PBE-D2/USP
K_2MoS_4	409563	9.32	9.22	9.39	9.38	9.44	9.27	9.28
K_2WSe_4	59242	9.73	9.83	10.09	9.80	9.88	9.84	9.68
Rb_2MoS_4	644177	9.72	9.59	9.79	9.51	9.58	9.56	9.68
Rb_2MoSe_4	644182	9.86	9.26	9.49	9.21	9.38	9.36	9.99
Rb_2WS_4	281586	9.62	9.22	9.79	9.51	9.60	9.80	9.71
Rb_2WSe_4	650057	10.10	9.80	10.09	9.80	9.82	9.97	10.10
Cs_2MoS_4	402076	10.04	10.14	9.56	9.51	9.912	9.90	10.12
Cs_2MoSe_4	627043	10.33	9.93	10.40	10.40	10.21	10.20	10.42
Cs_2WS_4	249347	10.05	9.85	9.81	9.80	9.52	9.81	9.59

Furthermore, let us recall that the computed properties are a local minimum in the potential

energy surface at the level of theory used. This strictly dictates that, within a theoretical approximation, the properties should be computed for the geometries equilibrated within that level of theory. However, if this theoretical ground state differs from the experimental data, depending on a given interest, this problem may be overcome by restricting certain degrees of freedom. One particular example of this, which is of interest to us, is in band gap calculations. It is quite common in the literature for theoreticians to use experimentally determined crystal structures without further relaxation [**85**], allowing the use of more accurate approximations for a given property.

We are not advertising for or against any of the multiple available approximations for first-principles materials modeling. Here, we aim to determine the most appropriate conditions to model and compute the physical properties of the A_2MX_4 compounds and relatives. First, we evaluate whether a standardized-condition approach (similar to those employed in high-throughput studies) is suitable for the modeling of the compounds.

Here, we took on the following approach. First, the atomic positions within the experimental volume were fully relaxed. These are our reference structures for our band structure calculations. On par, as we seek to determine the most appropriate conditions for posterior simulations of these materials - we perform an assessment of different density functional approximations to reproduce the experimental structure. For this, convergence tests were performed for the minimal amount of materials that covered all involved species (K, Rb, Cs, Mo, W, S, Se), with the LDA, PBE, PBEsol exchange-correlation functionals. Additionally, the effect of long-range interactions was probed through the Grimme-D2 (DFT-D2) with PBE. Finally, as chemical complexity increases, i.e. the number of electrons involved, relativistic effects may pose an effect on the accuracy of our simulations. Hence, we also perform structural optimization including spin-orbit coupling (SOC) for the known compounds.

As mentioned above, different density functional approximations were used to determine the theoretical ground state structures. Within the approximations, the kinetic energy cutoff was standardized.

First, following the methodology for the optimization of Na_2MoSe_4, we varied the volume isotropically (i.e. we varied a, and fixed $b = b/|a|$, $c = c/|a|$) for the nine compounds and identified the theoretical minimum within the LDA, PBE, PBEsol, PBE-D2 and PBE-SOC levels of theory. The obtained values are summarized in Table 4.1. Independently, a full-dimensional optimization was performed (i.e. varying a, b, c and atomic positions) at the PBE-D2 level of theory. These values are summarized in in table 4.1.

We compare our dual approach to the experimental values graphically in Fig 4.4. In the left panel, we compare the equilibrium volumes obtained through an isotropic variation in the volumes, maintaining fractional atomic positions fixed within the unit cell. A computationally cheap approximation associated with a high price in accuracy. Note that, for compounds with small volumes, the results are fairly comparable to the experiment. However, as volume increases, so does our error. This indicates that our computations have clearly led us to reach false ground states, and that such an approximation (variation of volume, atomic positions fixed) is inappropriate for such materials.

The emergence of these false ground states can be understood from the following perspective. First, these computations were performed using ONCVPSP. Planewave DFT computations on periodic systems be performed on a complete basis set, this is, the basis set should contain all plane waves with energies below the kinetic energy cutoff (In reciprocal space, this corresponds to all points on the lattice that lie within a sphere of radius r_c, as mentioned in chapter 2). During geometry optimization, varying the volume while fixing atomic positions will have an impact on the size and shape of the basis set, causing the sphere to "deform" into an ellipsoid. If this occurs, it is said that the basis set is incomplete. This results in the errors in the diagonal elements of the Jacobian matrix during self-consistent calculations, which physically is the stress tensor. These errors, correspond to resulting stress between particles known as Pulay stress σ_P.

Pulay stress typically affects total energy calculations in such a manner that it typically leads to an underestimation of the equilibrium volume. Without going into further detail regarding Pulay stress and forces, we mention the possible solutions.

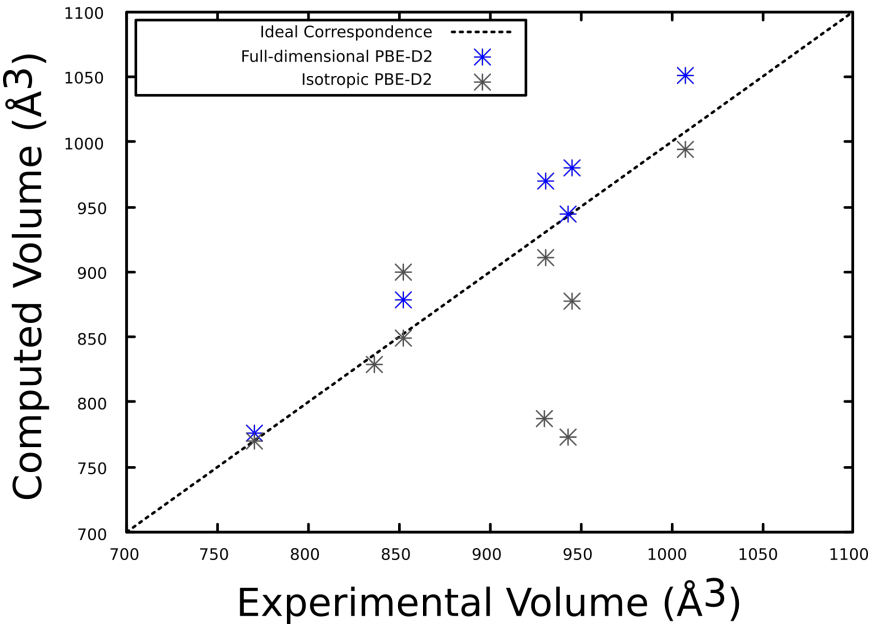

Figure 4.4: Computed versus experimental values in $Å^3$. The computed equilibrium volumes were obtained through a full-dimensional optimization (blue), varying lattice constants as well as atomic positions. We compare the Full-dimensional PBE-D2/USP with the isotropic PBE-D2/ONCVPSP volumes (grey).

First, if the basis set is incomplete, a logical solution would be to add more planewaves - this is, increase the kinetic energy cutoff. This is the most straightforward solution, and can often be the cheapest. Alternatively, if the used energy cuttoff was deemed appropriate for the system, another possible solution would be to use different integration grids ; add more k-points or use larger FFT (Fast Fourier Transform) grids. When a basis set is incomplete and Pulay forces are present, the $E(V)$ curve is somewhat "jagged", as the total energy integrations are non-continuous. Increasing the dimensions of the integration grids will therefore smoothen the $E(V)$ curve.

However, let us recall that these computations were performed using ONCVPSP with a kinetic energy cutoff of 90 Ry, and medium-sized k-point and FFT grids. Increasing the energy cutoff for close to a dozen materials defeats the purpose of our approximations, and using stringent k-point grid for geometry optimization is outweighed by the increase in computer time. An ideal solution would be to use a complete basis set while at the same time, reducing computer resource consumption.

At this point, we take on a second approach to finding the equilibrium geometries. This time, we replace the ONCVPSP for USP (ultrasoft pseudopotentials), with an optimized energy cutoff of 40 Ry. Additionally, to further mitigate the effects of Pulay forces, we remove all restrictions imposed on the degrees of freedom in our previous approximation. Essentially, this means that we performed a full-dimensional optimization of the structures, varying lattice vectors and atomic positions in an iterative manner until the theoretical global minimum was reached. For the full-dimensional optimization, only the PBE-D2 approximation was probed. As seen in the right side of 4.4, the accuracy increases dramatically. The full-dimensional PBE-D2 data points are plotted in blue points, which are clearly in general closer to the experimental volumes ($R^2 = 0.10$) than the false equilibrium volumes obtained through the isotropic PBE-D2 approximation, depicted by dark grey points ($R^2 = 0.29$).

4.5.1 Band structures

For our preliminary electronic structure investigation, we limit our scope to the GGA level of theory. As mentioned above, we take the fully relaxed experimental structures as our control set. This is justified and motivated by (i) band structures are generally insensitive to small variations in the volume, which account for the possibility of not being at the global minimum, (ii) in order to truly understand the electronic properties of these *Pnma* alkali-ion transition metal chalcogenides, we must forcibly go beyond the GGA and employ predictive methods. Hence, as a preliminary analysis, these band structures will provide insight into the qualitative electronic structure of the compounds. One note to keep in mind is that the obtained values for the bandgap, E_g, will be underestimated.

In figure 4.5, we show the electronic band structures for the nine experimentally known compounds. These band structures were computed using the PBE-D2 computed structures with k-point grids of dimensions $18 \times 24 \times 12$, and an energy tolerance of 1×10^{-6} eV. From our previous work on Na_2MoSe_4 [**82**], we learnt that the general electronic structure of the A_2MX_4 system is governed by the MX chemistry. The partial hybridization between valence shells of the M and X species gives

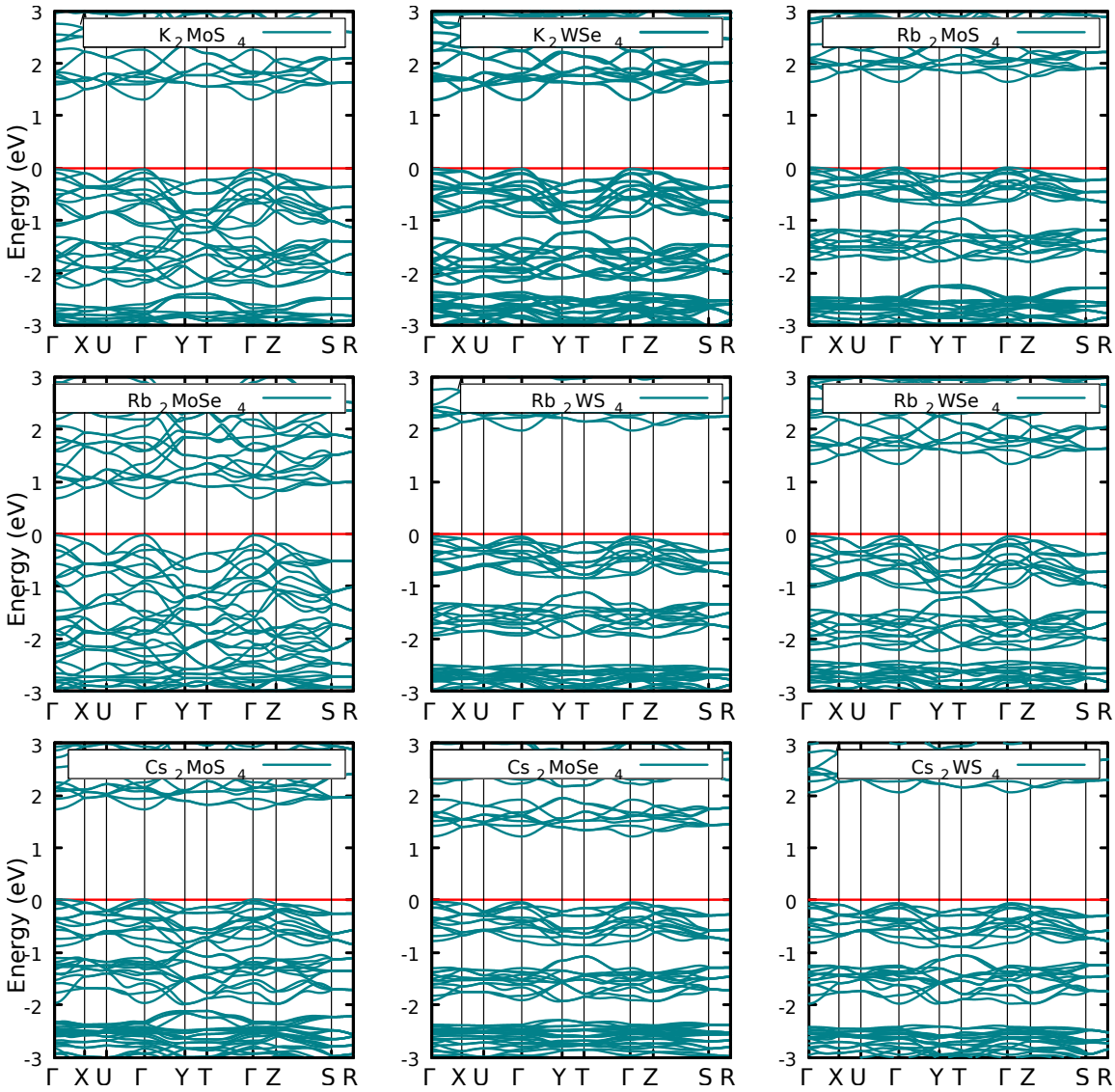

Figure 4.5: Electronic band structure of the known alkali-ion metal chalcogenides A_2MX_4 computed with PBE exchange-correlation. The E_F is located at the highest occupied valence band and indicated by a red line.

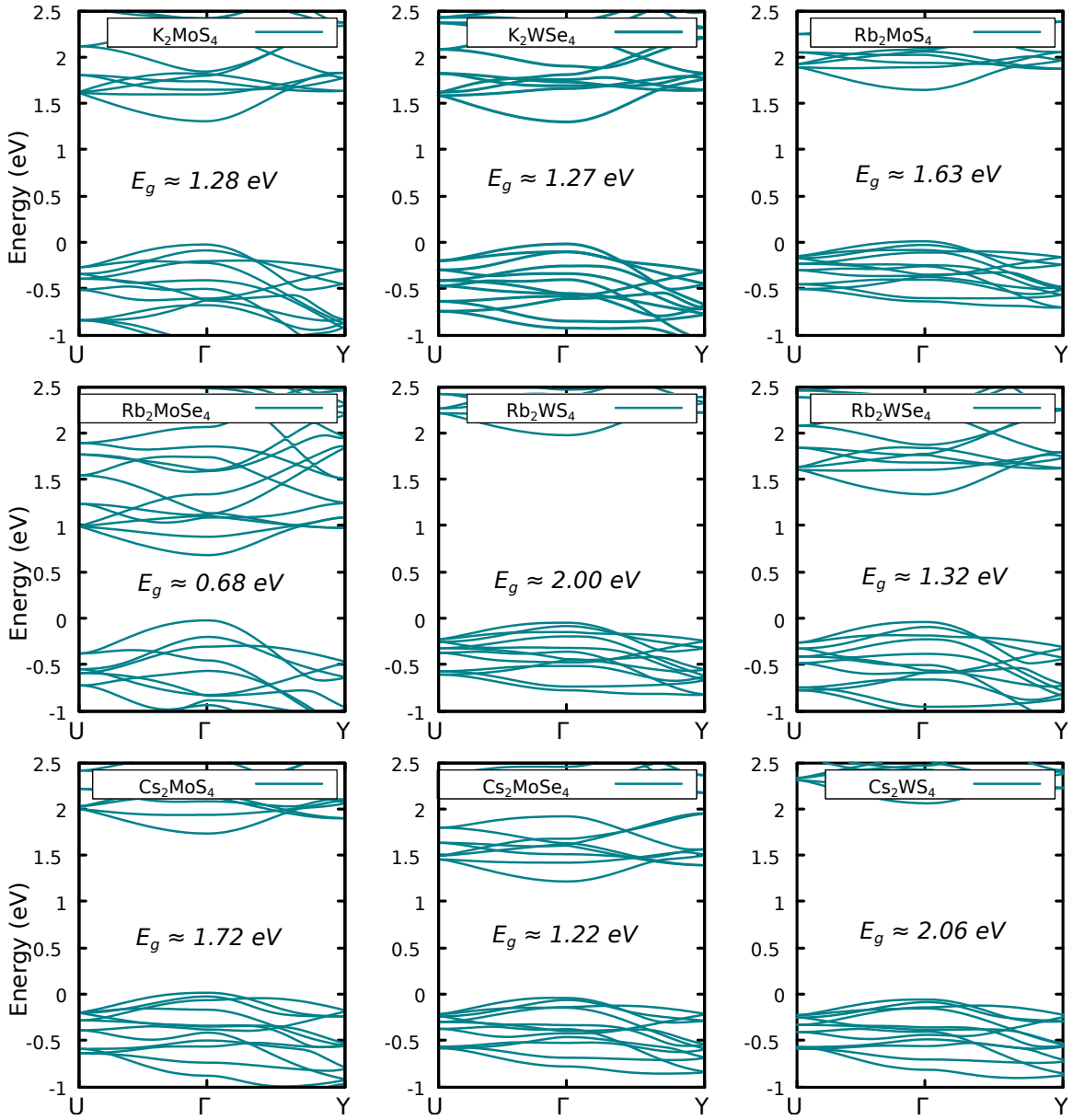

Figure 4.6: Electronic band structures of the known alkali-ion metal chalcogenides obtained via PBE. Energy is shown between $E = -1$ and $E = 2.5$ eV, to better visualize the bandgap.

rise to an energy gap between the valence and conduction bands, which are composed primarily of X p and M d orbitals, respectively. Since the protoypical structure and symmetry is unchanged, a similar band topology is to be expected. Here, the open question is how the changes in composition will affect the electronic structure of the AMX compounds. Particularly, will the transition from VBM→CBM remain direct, will it change, and how will the Fermi energy change as a function of composition?

As expected, the electronic band topology is similar and consistent throughout the family of compounds and resembles that of their sodium relative. Note, in all nine compounds, there exists a direct gap exactly at Γ. This is seen in Figure 4.5.

The band gap values are varied, within $0.6 \leq E_g 2.1$ eV, as illustrated in Figure 4.6. The smallest computed value of E_g is 0.68 eV, and corresponds to Rb_2MoSe_4. According to this gap value, the rubidium molybdenum selenide is a medium-gap semiconductor. On the other limit, the largest value of E_g obtained is equal to 2.06 eV, making Cs_2WS_4 a wide-gap semiconductor. Given that these values of E_g are underestimated due to systemic pitfalls of GGA, with a well-documented mean error of $30\% \leq e \leq 40\%$, we expect these two bandgaps to incease to the orders of 1 and 3 eV respectively. Although the gap for Cs_2WS_4 is wide, it is not expected that the material is an insulator, but rather a wide-gap semiconductor. Proportional increase should be seen for the rest of the compounds as well. Thus, it is reasonable to expect that the compounds could be suitable for applications in high-voltage or high-temperature optoelectronics. In this case, it would be the materials with smaller bandgaps that would be potential candidates for photovoltaic applications.

By means of ionic substitution and full-dimensional dispersion-corrected optimization, we have determined for the first time the crystal structures of the three missing (i.e. not yet synthesized) compounds. These are namely, K_2MoSe_4, K_2WS_4, and Cs_2WSe_4. As expected, these are semiconductors with E_g at Γ, with E_g values of approximately 1, 1.8 and 1.55 eV.

To better illustrate the general electronic properties of the A_2MX_4 family and to validate our computations to E_g values recently obtained by high-throughput PBE(PAW) computations, we

Table 4.2: Electronic bandgaps computed at the PBE level using the PBE-computed geometries. We compare our obtained values for E_g with those predicted by the Materials Project database (MP).

Compound	Bandgap type	$k_i - k_{i'}$	E_g (eV) This work	E_g (eV) MP
K_2MoS_4	D	Γ	1.28	1.43
K_2WSe_4	D	Γ	1.28	1.43
Rb_2MoS_4	D	Γ	1.63	1.58
Rb_2MoSe_4	D	Γ	0.68	1.03
Rb_2WS_4	D	Γ	2.00	1.99
Rb_2WSe_4	D	Γ	1.31	1.49
Cs_2MoS_4	D	Γ	1.72	1.77
Cs_2MoSe_4	D	Γ	1.22	1.22
Cs_2WS_4	D	Γ	2.06	2.15

Table 4.3: Predicted and optimized lattice parameters for the missing A_2MX_4 compounds computed at the PBE-D2(USP) level of theory.

Compound	**a** (Å)	**b** (Å)	**c** (Å)	V (Å^3)	E_g
K_2MoSe_4	9.627	7.089	12.449	847.79	1.0
K_2WS_4	9.32	6.96	12.22	792.53	1.8
Cs_2WSe_4	9.84	7.09	12.63	880.59	1.5

include Table 4.2. Note that a general agreement if observed between our PBE(USP) and the reference PBE(PAW) data, including the gap being at Γ. However, a significant difference in the E_g values is seen for Rb_2MoSe_4, where the MP predicts a gap of 1.03, counter to our value of 0.68. One possible explanation for the differences in bandgap values is that while our computations were carried out with a high number of k-points, the reference data was obtained with a loose k-point mesh of dimensions $3 \times 2 \times 2$, which is typically not stringent enough to yield predictive results. The use of such a loose k-point grid, as mentioned before, can also lead to false equilibrium volumes which in turn yield false computed properties. It should be noted, that while our equilibrated geometries were approximated with including long-range dispersion, the MP volumes are overestimated (often times exceeding a tolerance of 5%) as they are obtained with PBE with no further corrections.

Chalcogenide chemistry can influence on the value of the bandgap. In Fig4.8, we directly compare the computed bandgaps of twelve A_2MX_4 compounds. The compounds are numbered such that we increase the number of complexity beginning with the chalcogenide anion, then the transition metal and finally, the alkali-metal. Therefore, $K_2MoS_4 = 1$ on the x axis, $K_2MoSe_4 = 2$, K_2WS_4=3, ... , $Cs_2WSe_4 = 12$ on the x-axis. By this logic, we also note that all sulfides correspond to odd numbers

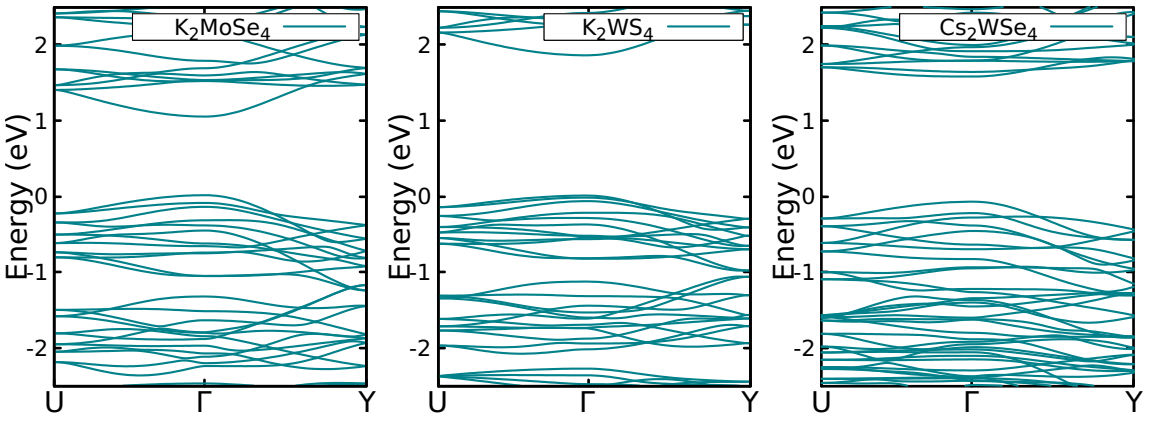

Figure 4.7: Electronic band structures of the predicted or "missing" alkali-ion metal chalcogenides obtained via PBE. Energy is shown between $E = -2.5$ and $E = 2.5$ eV.

(teal) while selenides are evens (blue). Note that., Sulfides have larger bandgaps.

In order to better understand the electronic structure of the presented alkali-ion transition metal chalcogenides, beyond-GGA calculations must be carried out to obtain predictive values of E_g. Within the APW+lo approximation, the TB09 MGGA functional has been known to yield E_g values comparable to those of HSE06 [**78**, **79**, **80**, **81**] GW. These calculations are currently under preparation. Additionally, partial density of states (PDOS) should be computed in order to understand the VBM band shifts as a function of orbital hybridization, individually for each compound. Finally, electron localization functions may be determined to gain insight into the indirect interactions between the A and M species, or the A cations with the MX tetrahedra, as this can have an effect on structural properties and charge density.

4.6 Conclusions

We have presented a theoretical investigation of twelve alkali-ion transition metal chalcogenides with oP symmetry, and general formula A_2MX_4. Computations based on Density Functional Theory were systematically performed on nine known and three proposed materials to model their equilibrium geometries and electronic band structures. We have discovered that the entirety of the A_2MX_4

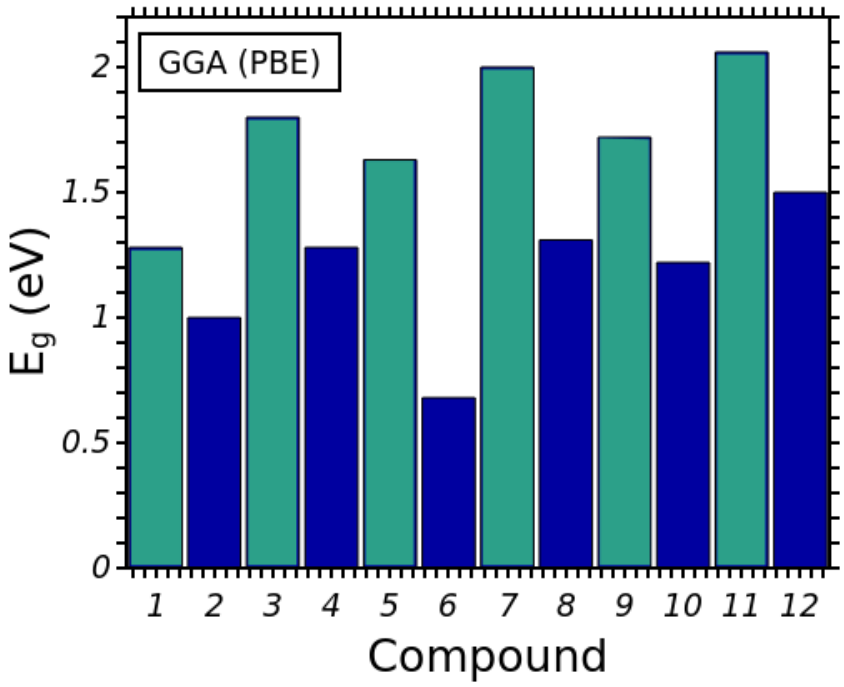

Figure 4.8: Bandgaps versus composition is shown for the twelve compounds studied. Note that the E_g for sulfides (teal) are greater than those of selenides (blue) in all cases.

compounds are semiconductors, with a direct bandgap at Γ. Preliminary GGA computations reveal that these materials have medium to wide bandgaps, ranging between the orders of 0.7 and 2.0 eV. While GGA underestimates the bandgap, these results are promising as they provide qualitative insight into the materials' physics. Furthermore, we note that all sulfides have larger bandgaps than the selenides in the family. Currently, all-electron meta-GGA calculations are being prepared to obtain bandgaps with predictive accuracy. Based on their electronic structure, these alkali-ion metal chalcogenides show potential for applications in optoelectronic, photovoltaic, high-power and high-temperature devices.

Chapter 5

Quantum-mechanical modeling of two-dimensional ternary niobium tellurides

5.1 Introduction

Harnessing the power of quantum materials is one of the core interests of condensed matter and materials physics. Understanding the origin of genuinely quantum phenomena in these materials at a fundamental level will play a crucial role in the development of next-generation technologies, such as quantum information, spin electronics (spintronics), magnonics and spin-orbitronics [**85**, **86**, **87**, **88**, **89**]. The discovery of graphene [**90**], a one-atom-thick allotrope of carbon, was a welcoming to novel and exciting physics in the following years. Notable members of the 2D materials realm are other allotropes such as phosphorene [**91**] and silicene [**92**, **93**], among others [**94**, **95**, **96**, **97**], and transition metal dichalcogenides (TMDs) [**98**, **99**, **100**, **101**, **102**] such as $NbTe_2$ [**102**, **103**] a large family of monolayers with a wide spectrum of properties and applications. In a general sense,

the ever growing catalog of predicted and discovered 2D materials includes metals, semiconductors, superconductors, photo-catalysts, topological insulators, Mott insulators, Weyl semimetals [**104**, **105**] and the recently incorporated (and long awaited) family of magnetic 2D materials. In 2017, ferromagnetism - a pure and genuine quantum effect [**106**] - was discovered in ultrathin layers of vdW crystals CrI_3 [**107**] and $CrGeTe_3$ [**108**]. Huang and colleagues demonstrate that the magnetic chromium triiodide can be well descibed with the two-dimensional Ising model, with magentic moments (spins) lying perpendicular to the lattice-plane. Regarding the vdW chromium germaniun telluride $CrGeTe_3$, Gong and colleagues show that the magnetic nature of the material is consistent with the Heisenberg model, this is, with magnetic moments oriented without restriction [**106**, **107**, **108**]. This breakthough catalyzed an intensive increase in experimental and theoretical research, quickly followed by the discovery of ferromagnetism in monolayer VSe_2 [**109**]. Although the vdW tri-telluride $CrGeTe_3$ had been investigated in the past [**110**, **111**, **112**, **113**, **114**], it wasn't until 2014 that it was predicted to be ferromagnetic as a 2D crystal along with $CrSiTe_3$ by Li and Yang in 2014 [**110**]. Shortly after, $CrSnTe_3$ is predicted to be a ferromagnetic semiconductor as a single layer, and with a higher Curie temperature T_c than its -Ge- and -Si- siblings[**111**]. Both the CrI_3 and $CrGeTe_3$ systems have been studied extensively. Another interesting 2D ferromagnet is the the metallic Fe_3GeTe2 [**111**, **112**, **113**, **114**, **115**], in which the strong spin-orbit coupling effects result in perpendicular magneto-crystalline anisotropy [**102**]. Interest in magnetic 2D vdW materials relies on the desire to build feasible next-generation spintronic devices, as summarized in two recent reviews Gong and Xiang, and the other by K.S. Novoselov and co-workers [**89**, **116**]. In figure 5.1, we display a tabular summary of the *state of the art* of 2D magnetism. The table summarizes the materials known up until late 2019. As the field is currently growing, the literature is being updated nearly on a daily basis.

As mentioned above, transition metal chalcogenides are well known quantum materials. It has been shown that layered MX_n systems where M is a first row transition metal, can lead to charge density waves (CDW) and superconductivity [**117**], magnetic and topological properties [**102**, **103**].

<table>
<tr><td>Chalcogenides</td><td>$Cr_2Ge_2Te_6$, $Cr_2Si_2Te_6$, Fe_3GeTe_2, VSe_2*, $MnSe_x$*</td><td colspan="2">$Fe_2P_2S_6$, $Fe_2P_2Se_6$, $Mn_2P_2S_6$, $Mn_2P_2Se_6$, $Ni_2P_2S_6$, $Ni_2P_2Se_6$, $CuCrP_2Se_6$*, $AgVP_2S_6$, $AgCrP_2S_6$, $CrSe_2$, $CrTe_3$, $Ni_3Cr_2P_2S_9$, $MnBi_2Te_4$*, $MnBi_2Se_4$*</td><td>$CuCrP_2S_6$</td></tr>
<tr><td rowspan="2">Halides</td><td rowspan="2">CrI_3*, $CrBr_3$, GdI_2</td><td rowspan="2">$CrCl_3$, $FeCl_2$, $FeBr_2$, FeI_2, $MnBr_2$, $CoCl_2$, $CoBr_2$, $NiCl_2$, VCl_2, VBr_2, VI_2, $FeCl_3$, $FeBr_3$, CrOCl, CrOBr, CrSBr, $MnCl_2$*, VCl_3*, VBr_3*</td><td colspan="2">$CuCl_2$, $CuBr_2$, $NiBr_2$, NiI_2, CoI_2, MnI_2</td></tr>
<tr><td colspan="2">α-$RuCl_3$</td></tr>
<tr><td>Others</td><td>VS_2, InP_3, GaSe, GaS</td><td>MnX_3 (X = F, Cl, Br, I), FeX_2 (X = Cl, Br, I), MnSSe, $TiCl_3$, VCl_3</td><td colspan="2">SnO, GeS, GeSe, SnS, SnSe, GaTeCl, CrN, CrB_2</td></tr>
</table>

Figure 5.1: Table summary of the current status (2019) of reported 2D magentic materials. Color code: Green, bulk ferromagnetic vdW crystals; orange, bulk antiferromagnets; yellow, bulk multiferroics; gray, theoretically predicted vdW ferromagnets (left), half metals (center), and multiferroics (right), which have not yet been experimentally confirmed. Image taken from [**89**].

Tellurides in particular have drawn interest for the exotic physical phenomena they display. For example, WTe_2 and $MoTe_2$ show non-trivial topology both in the bulk and as monolayers. Recently, experimental evidence demonstrates that $NbTe_2$ is a topological superconductor [**103**].

On another note, ternary niobium tellurides have been gaining attention due to their properties originated from quantum confinement. Many of these materials are being "revisited", such as Nb_3SiTe_6, whose structure was determined via XRD in 1991 [**118**], it's quantum properties (electron - phonon coupling, magnetotransport) were not determined until 2015, published in Nature Physics [**119**].

Motivated by the re-emergence of metal-rich layered transition metal chalcogenides into the spotlight of condensed matter physics, we investigate three compounds as new 2D materials : $NbMTe_2$, where M is a magnetic element Fe, Co, or Ni. These materials' bulk structures were determined in the late 90's [**120**], and recent studies have revealed their quantum properties. Particularly, we highlight that $NbFeTe_2$ is the first vdW material to be observed with intrinsic magnetoresistence [**121**]. Additionally, $NbNiTe_2$ was recently used as a prototype to model how phonon-induced transitions can lead to topological quantum states [**122**]. In search for these properties, a high-temperature phase transitions was reported in 2019 [**123**]. These materials display remarkable properties, but are yet to be analyzed as isolated monolayers.

5.2 Objectives

- Model and determine the ground state structures for monolayers of $NbMTe_2$, where M = Fe, Co or Ni.
- Evaluate the stability of the three monolayers of the $NbMTe_2$ family.
- Investigate the quantum-mechanical (electronic and magnetic) properties of the three two-dimensional materials.

5.3 Computational Methods

We performed first-principles calculations based on Kohn-Sham Density Functional Theory (DFT) within the general gradient approximation (GGA), employing the Perdew-Burke-Ernzerhof (PBE) functional for exchange-correlation as implemented in Quantum ESPRESSO [**47**, **48**]. The bulk and monolayer structures were fully relaxed using scalar-relativistic ultra-soft pseudo-potentials, with a kinetic energy cutoff of 40 Ry to expand the Khon-Sham states in plane waves and a charge density cutoff of 320 Ry. Structure optimization calculations were performed with a convergence threshold for self-consistency of 1×10^{-6} Ry. To model the 2D structures, a vacuum of 15 Å was used to simulate surface effects and to avoid any inter-layer interactions, and a Monkhorst-Pack k-point mesh of $4 \times 1 \times 6$ centered on Γ was used to sample the firsFigure 5.1: Monolayer figt Brillouin zone (FBZ). The electronic structure calculations were performed using a Γ-centered $20 \times 1 \times 30$ k-point mesh to sample the FBZ.

The effect of spin-orbit coupling on band structure was computed by employing a fully-relativistic pseudopotentials.

5.4 Results

We have carried out a DFT-based investigation on three compounds, namely, iron-, cobalt-, and nickel- niubium tellurides. The three tellurides are layered compounds, making them ideal to study as free-standing monolayers. In the bulk, $NbFeTe_2$ and $NbNiTe_2$ crystallize in the orthorhombic *Pmna* space group, and $NbCoTe_2$ crystallizes in the orthorhombic *Cmce* space group. All three compounds hold two-dimensional structures and consisting of $NbMTe_2$ sheets oriented in the (0, 1, 0) direction. Nb^{2+} are bonded in a 4-coordinate geometry to four Te^{2-} atoms. The transition metal is in its M^{2+} state, in tetrahedral coordination with Te^{2-} atoms, and bonds with its nearest M atom.

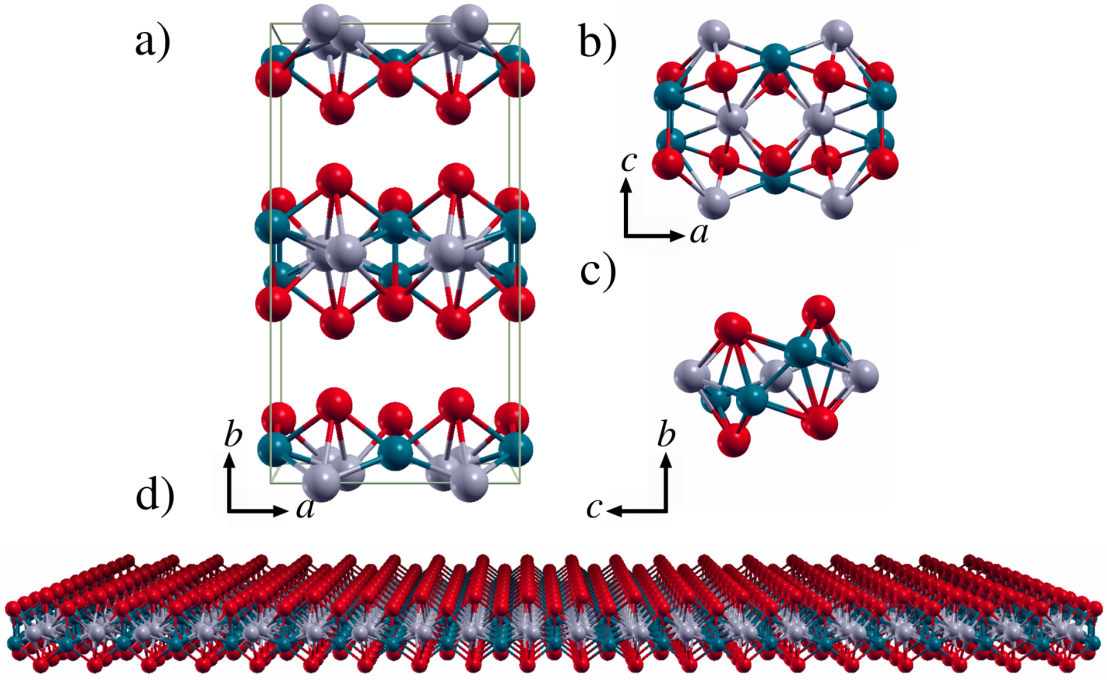

Figure 5.2: Prototypical crystal structure of $NbMTe_2$ (M = Fe, Co, Ni). The unit cell of the layered (bulk) structure is shown in (a), a top view is shown in (b), a side view in (c) and a perspective of the nanosheet is shown in (d). The grey, cyan and red balls represent Nb, M and Te atoms respectively.

A perspective frontal view of the prototypical crystal structure of bulk $NbMTe_2$ is shown in Figure 5.2 (a). In Figure 5.2 (b) and (c), we show the top and side views of the monolayer, and an

extended (super-cell) view of the two-dimensional structure is shown in Figure 5.2 (d).

To demonstrate that these materials could be treated as single-layer systems, we simulated exfoliation by investigating the change in the system's energy $\Delta E = E - E_0$ as a function of inter-layer distance $\Delta d = d - d_0$ (Å), where E_0 is the energy of the ground state structure, at $\Delta d = 0$. In 5.3, we show that as Δd increases, the system is taken out of equilibrium. The energy dispersion of

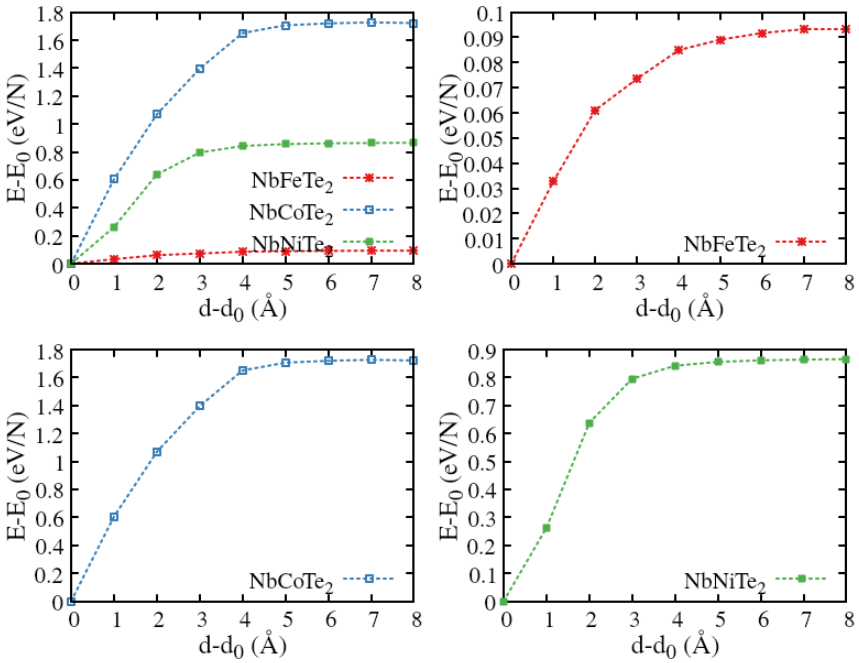

Figure 5.3: Here, the change in energy $\Delta E = E_0$ is plotted as a function of cleavage, i.e. as $\Delta d = d - d_0$ (Å) increases. The units shown are electron-volt per atom (eV/N).

the simulation box adopts the form of an asymptote, a limit at which the system's energy becomes independent of increases Δd, and long-range attraction vanishes. For all three compounds, this inter-layer interaction tends to vanish at $\Delta d5$ Å, and at this point we consider them monolayer structures. To further guarantee null interaction between layers, our computations from this point forward were performed in a 15 Åvacuum along the b vector.

The ground state structures were determined by investigating the change in the monolayers' energy as a function of lattice constants, a and c, while simultaneously relaxing atomic position.

The obtained lattice constants were $a = 8.072, c = 6.343$ for M = Fe ; $a = 7.940, c = 6.237$ for M = Co; and $a = 8.023, c = 6.306$ M = Ni. Note that the a is smaller for $NbCoTe_2$ than it is for $NbFeTe_2$, although $Z_{Co} > Z_{Fe}$. This can be understood through the effect that spin-states and coordination environments have on effective ionic radii in halides and chalcogenides, leading to a highly reduced ionic radius for Co^{2+} [**124**].

Furthermore, the magnetic ground state was determined by computing the system's total energy as a function of the magnetic ordering. Each unit cell contains four M^{2+} atoms, and each spin can be in either of two states, $\langle\uparrow|\,|\downarrow\rangle$. Therefore, there are a total of 16 possible spin-states, which can be reduced to 8 computations due to their symmetry. The initial spin-states and final energies are listed in Table 6.3, in Appendix B.

According to our computations, two of our three systems have notable magnetic properties as two-dimensional materials. First, let us note that in the bulk, $NbFeTe_2$ is ferrimagnetic (FiM), $NbCoTe_2$ is ferromagnetic (FM) and $NbNiTe_2$ is non-magnetic (NM). Reducing dimensionality does not only affect the layer's equilibrium geometries, but also their equilibium spin-states. Of the magnetic orderings probed, what is observed for $NbFeTe_2$ is that it transitions from FiM to FM. This can be explained by inter-layer interactons (or the lack of) in the compound. In the bulk, intra-layer ineteractions are strongly FM while there is antiferromagnetic (AFM) coupling between layers. Upon exfoliation, inter-layer coupling vanishes and FM coupling dominates. However, 2D-$NbCoTe_2$ is most stable in an antiferromagentic state, ($\uparrow\uparrow\downarrow\downarrow$), AFM4 in our list. From the magnetic standpoint, $NbNiTe_2$ is not interesting as it is non-magnetic. As a matter of fact, the initial FM configuration leads to a peak in total energy (the system is taken far out of equilibrium), and all other states are degenerate. In all cases, the final magnetic moment is zero. For support, we provide a plot E versus magnetic ordering in Apprendix B "Supplemental information for Chapter 5".

The final magnetic moments, along with the other important physical quantities, including those relevant for stability are summarized in Table 5.1.

The relative stability was assessed by calculating the formation enthalpy of the monolayers, this

Table 5.1: Summary of structural and physical properties of $NbMTe_2$ structures in the bulk and as monolayers.

System	**a** (Å)	**b** (Å)	c (Å)	M.O.	**M** (μ_B / N)	H_f (eV/atom)
$NbFeTe_2$						
Bulk	6.243	7.239	7.922	FiM		0.344
Monolayer	8.072	—	6.343	FM	2.02	0.343
$NbCoTe_2$						
Bulk	6.237	7.840	8.212	FM		0.297
Monolayer	7.940	—	6.237	FiM	0.80	0.295
$NbNiTe_2$						
Bulk	6.258	7.202	7.955	NM		0.437
Monolayer	8.023	—	6.306	NM	0.00	0.436

is, difference between the energy per atom of the conforming species (reactants), and the total energy of the system of interest (product). The formation enthalpy energy H_f per atom was calculated as

$$H_f = \frac{1}{N}\Big(\sum_i^k \alpha_i \mu_i - U\Big) \tag{5.1}$$

where N is the number of atoms within the conventional unit cell, α is the number of atoms of constituent element i with chemical potential μ_i in the solid phase ($\mu_i = U_i/N_i$), and k is the number of species involved in the reaction. Lastly, E is simply the total energy of the ternary compound monolayer. Thus, the formation enthalpy for a $NbMTe_2$ monolayer is explicitly given as

$$H_f^{2D}(NbMTe_2) = \frac{1}{16}\Big(4\mu_{Nb} + 4\mu_M + 8\mu_{Te} - U^{2D}_{NbMTe_2}\Big). \tag{5.2}$$

Here, we define our formation enthalpy in such a way that a positive value for H_f^{2D} is an indicator of stability. This is simply taken as a convention in the literature. For comparison, we also calculate the true H_f, for the compound as

$$H_f^{bk}(NbMTe_2) = \frac{1}{N}(\mu_{Nb} + \mu_M + 2\mu_{Te} - U^{bk}_{NbMTe_2}), \tag{5.3}$$

where $N = 16$ when M = Fe, Ni, and $N = 32$ in the case of M = Co. All total energies used in H_f calculations were obtained self-consistently. As seen in Table 5.1, the formation of all three

compounds are favored with respect to their separated reactants in the solid state.

To further understand the quantum-mechanical properties of the $NbMTe_2$ monolayers, we turn our attention to their electronic structures. For these computations, stringent integration grids were used. For k-points, we used MP grids of dimensions of $24\times1\times18$ for scalar-relativistic computations, and $18 \times 1 \times 12$ for full-relativistic computations.

First, we compute orbital-projected density of states (PDOS) for the three monolayers at their total equilibrium (i.e. structural and magnetic ground states). In 5.4, we plot PDOS as a function of E for values $-4 : 4$ eV, with the Fermi level set at 0. Note in 5.4 (a), higher DOS is observed for Fe atoms. Thus, the iron contributions to the electronic structure are dominant. It is here where we want to focus, on the Fe d electrons. Remarkably, clear FM behaviour is illustrated by the asymmetry of occupied in the spin-state $\uparrow$ (Fe d α) at $-4 \leq E \leq -1$ eV, and $\downarrow$ (Fe d β), which dominate between $-1 \leq E \leq -2$ eV. Lesser contributions cab be noticed from the Nb d electrons. The highest occupied valence electrons are in spin-down, with a magnetic moment $\mathbf{M}$ of 2.02 μ_B per Fe atom.

Next, we focus on the Co and Ni structures. Note that in our Cobalt monolayer, we have a more symmetric PDOS versus E plot, with minuscule - but noticeable local asymmetries near the Fermi level. Particularly, in 5.4 (b) it can be seen that spin-down states are dominant near E_F. The final contribution per Co atom is of 0.80 μ_B. In 5.4 (c), we can see that there is complete cancellation of the atomic magnetic moments, i.e. each Ni atom contributes with 0 μ_B.

Now, let us focus on the electronic properties of the materials. For these calculations, we consider a two-dimensional integration path within the oP Brillouin (same BZ as in Chapters 3 and 4). Since the materials are periodic in the xz-plane, we integrate along $\Gamma(0,0,0)$, $X(1/2,0,0)$, $U(1/2,0,1/2)$, $Z(0,0,1/2)$ and $\Gamma(0,0,0)$, scaled in units of $2\pi/|a|$. In Fig 5.5, we show the band structure of $NbMTe_2$ with and without spin-orbit coupling. To better appreciate the effect of spin-orbit coupling on $E(\mathbf{k})$, we plot scalar-relativistic and full-relativistic bands in the second and third rows. The band structures are consistent with the clear metallic character displayed in Fig 5.4, even when

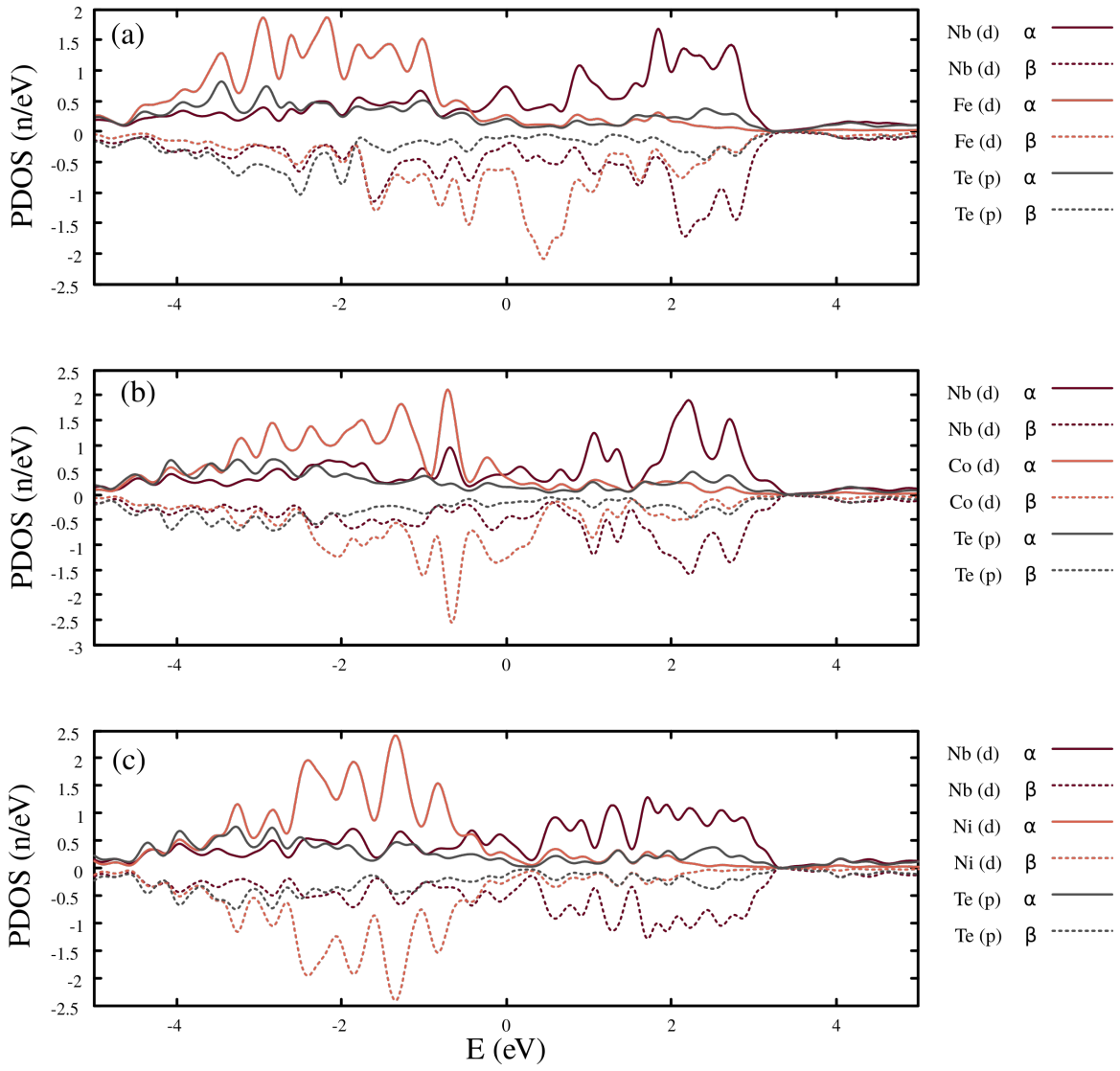

Figure 5.4: Atomic orbital projected density of states (PDOS) of the $NbMTe_2$ compounds. The iron, cobalt and nickel compounds are shown in (a), (b), and (c) respectively. As in the total DOS plots, spin-up is designated by α, spin-down states are β. The Fermi level is set to zero.

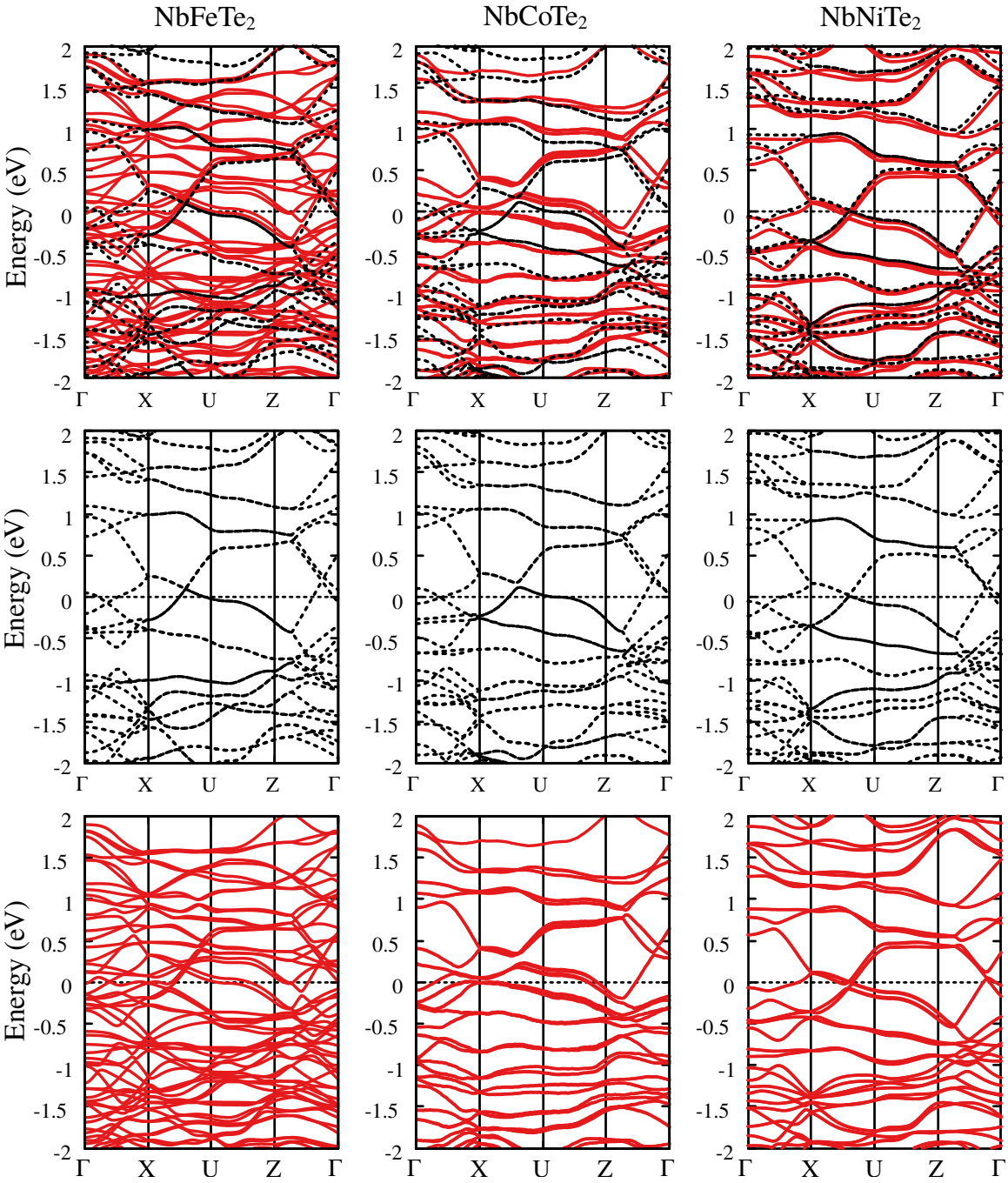

Figure 5.5: Electronic band structures of the $NbMTe_2$ (M = Fe, Co, Ni) monolayers. In the top row, bands are shown with and without spin-orbit coupling effects, in solid red and dashed black lines respectively. The GGA and GGA+SOC bands are plotted separately rows 2 and three, respectively. The Fermi energy E_F is set to zero in all cases.

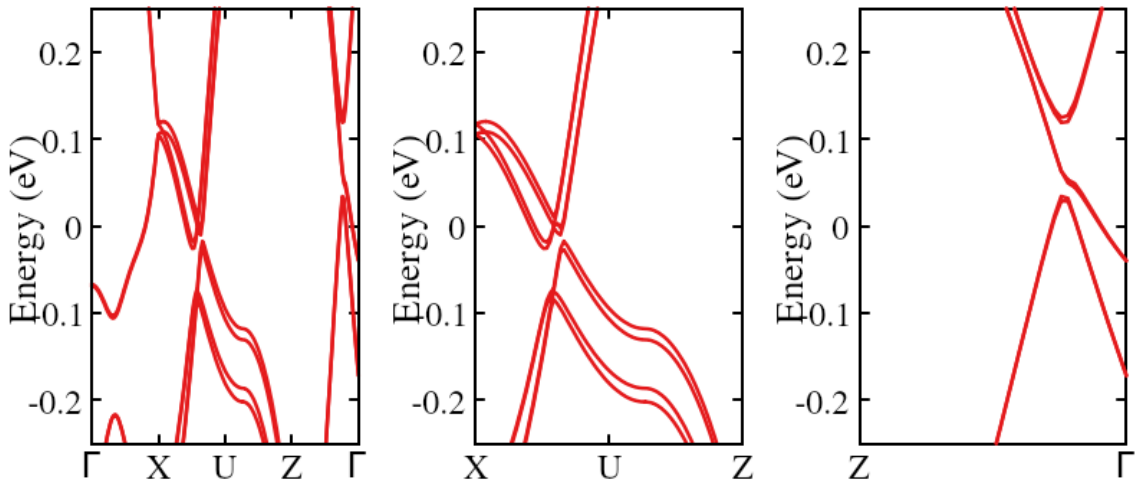

Figure 5.6: Amplified full-relativistic band structure of the 2D $NbNiTe_2$. Energy is plotted between $-0.25 \leq E \leq -0.25$ eV. The full path is shown in the left panel, center and right panels illustrate the $X - U$ and $Z - \Gamma$ avoided band crossings, respectively.

relativistic effects are included. The band topology is similar throughout the three compounds, and they all are characteristic of metals.

Interestingly, there are three noticeable $E(\mathbf{k})$ anti-crossings near the Fermi level. These avoided (or anti) crossings resemble Dirac Cones, characteristic of so-called quantum materials with massless fermions and ultra-high conductivity. This conductivity can be expected due to the linear $E(\mathbf{k})$ dispersion between regions $\Gamma \to X$, $X \to U$, and $Z \to \Gamma$. The most "pronounced" and prototypical potential Dirac Cone is that found from $Z \to \Gamma$, however, in all cases it is energetically shifted upward with respect to E_F. Hence, band-structure engineering may be a route worth entailing, via disorder of defect engineering. Also, these band structures reanimate the potential of $NbNiTe_2$ as a quantum material. Although it has been determined to be non-magnetic, it is the only of the three to have the anti-crossed bands exactly at the Fermi level. Here, we see that $NbNiTe_2$ has an avoided crossing at $X \to U$, and the $Z \to \Gamma$ is at a lower energy, i.e. closer to E_F than in its relatives. While it does not seem like an ideal Dirac Cone, this anti-crossing can be identified in Fig 5.4 (c), where there is a "dip" of occupied states near E_F.

Note also that for $NbNiTe_2$ the fully relativistic band structure essentially reproduces the scalar-

relativistic one, maintaining the Dirac-point at E_F between $X \rightarrow U$. In Fig 5.6, we show an amplification of the band structure of $NbNiTe_2$ in range $-0.25 \leq E \leq -0.25$ eV. Note that SOC splits the bands, producing two "peaks" or VBM-CBM pairs, illustrated in the center panel in $X - U - Z$. Along $G - Z$, note that although there is an avoided crossing, one band runs from the valence to the conduction states. This may be due to the bi-metallic nature of the behaviour, dominated by Nb d electrons, which in essence are interacting with Ni d electrons near E_F. The values for $E_g^{SOC}(k_1k_2)$ are $E_g^{SOC}(XZ) = 6.6$ meV and $E_g^{SOC}(Z\Gamma) = 0.0927$ eV (92.7 meV). The band structure of $NbNiTe_2$, and it's non-magnetic nature makes it a potential Topological Insulator. Although we do not in this study infer or conclude that $NbNiTe_2$ is a topological material, there is a clear resemblence with the bulk band structures shown in [**122**, **123**], especially the emergence of exactly two band anti-crossings near the Fermi level (See regions $Y - \Gamma$ and $T - Z$). In this study, we have limited ourselves to the isolated monolayer and it 's fundamental band structure. However, various reports can be found in the literature in which the Dirac cone of graphene or silicene is demonstrated to be tunable via intercalation between layers [**125**, **126**, **127**], or doping [**128**]. Furthermore, the bi-metallic nature of these materials are reason enough to encourage future studies involving electron-correlation effects.

Although electronic structure computations reveal the magnetic ground state properties of a given material, there is much more to be investigated to conclusively determine whether these materials could be suitable for quantum devices. One key property to consider in the design of 2D Ferromagnets, is the Curie temperature T_C. Here, we take on a phenomenological approximation to calculate T_C for $NbFeTe_2$, using Weiss Mean Field Theory (MFT), also known as Molecular Field Theory. In the MFT model, T_C is calculated as

$$T_C = \frac{1}{3k_B}\left[2zJS(S+1)\right] \tag{5.4}$$

where z is the number of nearest neighbor Fe atoms to a given Fe atom in the unit cell ($z = 1$),

S is the spin of each Fe atom, which is in our case the spin of Fe^{2+} (High-Spin) and k_B is the Bolztmann constant. To obtain S, we simply apply Hund's rules, recalling that the spin multiplicity of Fe is $n_e + 1$ where n_e is the number of unoccupied electrons in the outermost shell. This is also equal to defining spin multiplicity as $2S+1$, where $S = \sum_i S_i$, the sum of the spin magnetic moment of every electron in an orbital shell, with values $S_i = \pm\frac{1}{2}$. Iron has an electron configuration $3d^6 4s^2$. Since the $4s$ shell is filled, it is lower in energy than the $3d$ shells, of which one sub-shell is filled, and we are left with $n_e = 4$ (i.e. four electrons in spin $\uparrow$). Therefore, the spin multiplicity is 5 and finally $S = 2$. This value of S is consistent with the magnetic moment of $M = 2.02\mu_B$ per Fe atom in Table 5.1.

Next, we need to find J. Following the MFT methodlody in refs [**111**] and [**128**], and caculate the exchange energy between the Fe atoms a unit cell of $NbFeTe_2$ as

$$E_{ex} = -2zJS^2. \tag{5.5}$$

The energies of 2D-$NbFeTe_2$ in FM and AFM configurations read $E_{FM/AFM} = E_0 \pm E_{ex}$, where E_0 is the total energy of the system independent of the magnetic ordering, and E_{ex} is the exchange energy. One can easily see that $E_{FM} - E_{AFM} = 2E_{ex}$. At this point, we can solve for J and estimate T_C. As a result, we obtain $J = 4.4$ meV and $T_C = 205$ K. According to our prediction, $NbFeTe_2$ has a T_C comparable to that of bulk Fe_3GeTe_2, which was measured to be 205 K in [**129**]. The monolyer on the other hand, has a T_C of 20 K, but it was demonstrated increase up to room temperature by placing the Fe_3GeTe_2 nano-slakes in ionic gates. Our findings are comparable to the Curie temperatures of other 2D chalcogenides predicted by MFT, such as $CrSiTe_3$, $CrSnTe_3$, MnS_2 and $MnSe_2$, with T_C values of 294, 330, 253, and 286 K respectively. In these studies, it was shown that the level of DFT may influence in the predicted T_C.

It should be noted, however, that MFT is coarsely approximate and could yield T_C values that deviate from the experiment. We are very much aware of the limitations of our study, and there-

fore deeply encourage further investigation combining Monte Carlo simulations with the 2D Ising Hamiltonian, $\mathcal{H} = -2J \sum_{i>j} S_{iz} S_{jz}$ where the spins are aligned in the z axis and $S_{iz} = \pm 1/2$. This method has proved to yield more accurate exchange integrals and Curie temperatures. In our estimation, $\sum_j J_{ij}$ is simplified to zJ, for short-range interactions among first neighbors. In summary, $NbFeTe_2$ is a 2D metal with intrinsic ferromagnetism, with a reasonably high Curie temperature. Our results will serve as a foundation for future theoretical studies of this low-dimensional system and its relatives.

5.5 Conclusions

In summary, we have employed first-principles computations to predict the ground state electronic and magnetic properties of three new two-dimensional materials. The equilibrium structures, formation energies, magnetic ground states and electronic band structures are discussed for iron, cobalt and nickel niobium telluride monolayers $NbMTe_2$ (M = Fe, Co, Ni). We have demonstrated that monolayer structures may be obtained from the bulk through exfoliation, and that van der Waals interactions vanish for layers separated by a distance greater than 5 Å. Furthermore, we predict through DFT-based thermodynamics that that the three monolayers are stable. The three 2D materials are metallic in nature with notable spin-orbit coupling contributions. Avoided band crossings are observed near the Fermi level in the iron and cobalt compounds, and one anti-crossing exactly at E_F is seen in $NbNiTe_2$. The band structure of the materials indicates a possibility of Dirac-cone tuning via defect physics, and in this spirit we encourage future studies to investigate these materials through the lens of topological quantum chemistry, particularly $NbNiTe_2$, as it is non-magnetic. On another note, we demonstrate that that $NbFeTe_2$ is a robust ferromagnet, with a net magnetic moment of 2.02 μ_B per Fe(II) atom, and Curie temperature of 205 K predicted by Weiss Mean Field Theory. The central physical properties of these materials are quantum-mechanical in nature, making them potential candidates for next-generation technologies. This is the first theoretical study

of these three compounds as purely 2D materials, and is aimed to serve as a reference point for future studies focusing on the topological, electronic and magnetic properties of the monolayers or in heterostructures.

Chapter 6

Conclusions and Future Directions

In this thesis we have explored how computational quantum mechanics may be employed to predict the physical properties of functional materials. Particularly, this work has been dedicated to employing Kohn-Sham Density Functional Theory (DFT) for modeling materials that are of core interest in condensed matter physics, chemistry and materials science. We present computational studies of different ternary transition metal chalcogenides with potential applications in solid-state devices. Concretely, we studied a family of bulk chalcogenide semiconductors, with promising properties for optoelectronic and photovoltaics, and we provided a theoretical perspective on the physics of a family of niobium telluride monolayers with potential applications in quantum devices.

We began with a systematic investigation of the sodium molybdenum selenide, Na_2MoSe_4. At the molecular level, Na_2MoSe_4 is isotypical to the well-known compound sodium molybdate (Na_2MoO_4), however it's extended structure remained undisclosed. Through the joint use of DFT with the data-mining + ionic substitution method, we identified the energetically stable phase of the compound in the solid state. At equilibrium, Na_2MoSe_4 crystallizes in a primitive orthorhombic lattice (oP) and satisfies the symmetry of the $Pnma$ space group. This is evidenced by thermodynamics based on DFT total energies, which further reveals that crystalline Na_2MoSe_4 is isotructural to a dozen chemically analogous compounds that have been experiemtally realized. Furthermore, we demon-

strated through the performance of Meta-GGA calculations that Na_2MoSe_4 is a direct bandgap semiconuctor, with an E_g of 0.53 eV located exactly at Γ. Additional to it's moderately narrow bandgap, the effective masses for the electron quasi-particles around Γ indicate that it is a suitable candidate for infrared or high-speed optoelectronics. Finally, Na_2MoSe_4 can be seen as a protoypical A_2MX_4 material, meaning that the fundamental properties of the sodium compound can provide qualitative insight into the general electronic structure of it's inorganic isostructures.

Being ours the first report on the ground state properties of Na_2MoSe_4, we highlight some opportunities for future research. First, Density Functional Perturbation Theory may be used to characterize the semiconductor's vibrational spectra, such as Raman or Infrared. Furthermore, finite-temperature simulations of Na_2MoSe_4 via *ab-initio* Molecular Dynamics could provide insight into the compound's ionic-transport properties as well as it's thermal stability.

To further understand the ground state properties of alkali-ion transition metal chalcogenides, we go beyond the case of Na_2MoSe_4 and begin a preliminary theoretical investigation of related materials. From a first-principles standpoint, we investigate the ground state properties of a family of inorganic compounds with $oP(Pnma)$ symmetry and formula A_2MX_4, where A = K^+, Rb^+, Mo^+ ; M = Mo, W ; and X = S^-, Se^-. We study a total of a dozen compounds, of which nine have been synthesized and three are predicted in this work. Here, our objectives were to determine suitable simulation conditions as well as disclosing their electronic properties. First, we discussed why standardizing simulation conditions is challenging for sets of different compounds, and how imposing a "one size fits all" approximation will have a significant effect in the rigor and accuracy of the calculated properties. Particularly, this can lead to false theoretical ground states, which can be identified by volumes that deviate from the experimental values. We have determined that the PBE-D2 approximation using ultra-soft pseudopotentials is reasonably successful at reproducing the experimental volumes of the nine synthesized compounds.

Second and most importantly, we demonstrate that A_2MX_4 is a family of direct bandgap semiconductors, with values of E_g suitable for applications in photovoltaics and optoelectronics. The

predicted bandgaps at the GGA level of theory are between the orders of $0.7 \leq E_g \leq 2$ eV, meaning that the compounds have moderate to wide bandgaps. It is important to realize that the values for E_g presented here are underestimated, for which Meta-GGA computations are in preparation to obtain predictive values. Also, we encourage further studies to investigate thermal stability by means of AIMD and compute the absorbance coefficients. Our work is intended to serve as a catalogue for experimentalists who may find these compounds interesting, and a starting point for future studies focused on defect physics.

On the other limit, we have taken a predictive approach to propose novel two-dimensional materials for potential applications in quantum devices. Inspired by the recent emergence of 2D magnetism and the increasing attention to Dirac materials, we combine chemical induction with physical rigor to model $NbMTe_2$ monolayers, where M is a magnetic element - Fe, Co or Ni. Starting with the experimental bulk structures, we simulate the effect of mechanical exfoliation by studying the change in energy as a function of interlayer distance. We discover that van der Waals inter-layer attraction vanishes for separations larger than 5 Å. The formation of the three monolayers is energetically favored, with formation enthalpies comparable to those of their bulk structures. Furthermore, a combinatorial investigation of spin-states reveals that 2D-$NbFeTe_2$ is a identified as a robust ferromagnet, with a magnetic moment of 2 μ_B per Fe atom and a Curie temperature of 205 K as predicted by mean field calculations. The three materials are 2D metals with significant spin-orbit coupling, with $NbNiTe_2$ having a particularly interesting electronic structure as it shows a band anti-crossing exactly at the Fermi level, and one in its vicinity, which may possibly be tuned via defect physics. The gap at this so-called Dirac cone is of 6.6 meV. The band structure and non-magnetic nature of Nickel Niobium Telluride makes it a potential Topological material. In the future, we aim to investigate the materials through the lens of topological quantum chemistry. Additionally, we recognize that relative stability is not sufficient to argue that a material is absolutely stable, therefore dynamical stability is currently being studied within the framework of Density Functional Perturbation Theory. Additionally, Coulomb correlation effects are being investigated via DFT+U, where

U is a Hubbard-like potential. To truly characterize the magnetic properties of these materials and obtain predictive values for T_C, we aim to perform Monte Carlo simulations of the 2D Ising model on $NbFeTe_2$.

A : Supplemental information for Chapter 3

A.1: Hypothetical structures of Na_2MoSe_4

Table 6.1: The 21 candidate have been made publicly available on the https://materialsproject.org/. This table includes the numBer of candidate, structure predictor ID (SP-ID), the predicted Space Group and the number of sites within the unit cell.

No.	SP-ID	Space Group	Sites
1	851288	$Fd-3m$	14
2	851289	$Fddd$	14
3	851293	$Pnma$	28
4	851302	$C2/m$	14
5	851313	$R-3$	42
6	851319	$P3_2$	126
7	851324	$C2/m$	14
8	851349	$C2/c$	14
9	851350	$I4_1/amd$	56
10	851351	$R-3$	42
11	851354	$C2/m$	14
12	851355	$Cmcm$	14
13	851356	$Pnma$	28
14	851360	$Cmmm$	7
15	851361	$Pccn$	28
16	851362	$Fmmm$	7
17	851363	$Pbam$	14
18	851364	$Pbca$	28
19	851368	$Pbcn$	28
20	851369	$P21/c$	56
21	851376	$Pnma$	28

A.3: Optimized atomic positions of *oP* Na_2MoSe_4

Table 6.2: Atomic positions in crystal(fractional) coordinates of optimized Na_2MoSe_4 with lattice vectors: $a = 9.1199998856\hat{x}$, $b = 6.6931681633\hat{y}$, $c = 11.8195199966\hat{z}$. These values are taken from the Quantum ESPRESSO input file.

Atom	x	y	z
Na1	0.938425369	0.250000000	0.861179401
Na2	0.061574638	0.749999982	0.138820589
Na3	0.561574631	0.749999982	0.361179361
Na4	0.438425290	0.250000000	0.638820599
Na5	0.646825796	0.250000000	0.120218676
Na6	0.353174204	0.749999982	0.879781324
Na7	0.853174204	0.749999982	0.620218676
Na8	0.146825796	0.250000000	0.379781324
Mo1	0.238271427	0.250000000	0.057999873
Mo2	0.761728600	0.749999982	0.942000127
Mo3	0.261728573	0.749999982	0.557999833
Mo4	0.738271400	0.250000000	0.442000127
Se1	0.996194296	0.250000000	0.122790474
Se2	0.003805779	0.749999982	0.877209526
Se3	0.503805757	0.749999982	0.622790474
Se4	0.496194191	0.250000000	0.377209526
Se5	0.362791152	0.982838354	0.133865255
Se6	0.637208796	0.017161668	0.866134755
Se7	0.137208848	0.017161668	0.633865245
Se8	0.862791204	0.982838354	0.366134755
Se9	0.637208796	0.482838390	0.866134755
Se10	0.362791152	0.517161681	0.133865255
Se11	0.862791204	0.517161681	0.366134755
Se12	0.137208848	0.482838390	0.633865245
Se13	0.265255025	0.250000000	0.862531221
Se14	0.734744949	0.749999982	0.137468820
Se15	0.234744975	0.749999982	0.362531180
Se16	0.765255051	0.250000000	0.637468820

A.4: Additional band structures

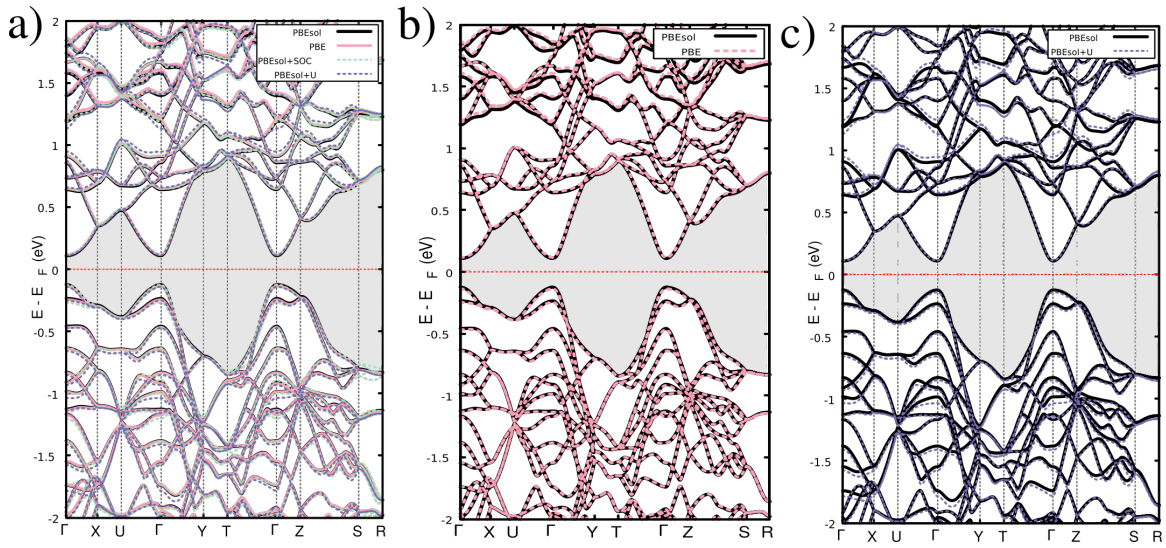

Figure 6.1: Electronic band structure of Na_2MoSe_4. Comparison between PBE, PBEsol, PBE+SOC and PBE+U in (a), separated intro PBE/PBEsol in (b) and PBEsol/PBEsol+U in (c).

Appendix B: Supplemental information for Chapter 5

B.1: Determination of magnetic ground states

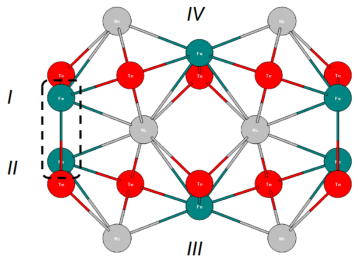

Figure 6.2: Cartoon top-view of $NbMTe_2$. We identify the M atoms I, II, III, and IV corresponding to the probed spin-state.

As mentioned in Chapter 5, multiple spin-states were studied to determine the magnetic ground state of the $NbMTe_2$ monolayers. In total, there exist sixteen (16) possible spin-states, but due to periodicity these can be reduced to eight unique spin-states or magnetic orderings. For the 8 magnetic orderings, we performed SCF total-energy calculations with the convergence criteria mentioned in the computational details section of Chapter 5.

The total energies in the former table 6.3 are in Rydberg constant units [Ry]. Here, in Figure 6.3, we explicitly show the system's E as a function of the spin-states in eV.

Table 6.3: Initial magnetic orderings (M.O.) probed used in total energy computations for each $NbMTe_2$ to determine the magnetic ground state. Total energies are truncated to the third significant digit, and are listed un Rydberg constants [Ry].

No.	M.O.	Label	$E(NbFeTe_2)$ [Ry]	$E(NbCoTe_2)$ [Ry]	$E(NbNiTe_2)$ [Ry]
1	↑↑↑↑	FM	-2129.610	-2276.847	-1514.861
2	↑↑↑↓	AFM1	-2129.578	-2276.847	-1514.861
3	↑↑↓↑	AFM2	-2129.579	-2276.839	-1514.861
4	↑↑↓↓	AFM3	-2129.590	-2276.848	-1514.861
5	↑↓↑↑	AFM4	-2129.590	-2276.848	-1514.861
6	↑↓↑↓	AFM5	-2129.590	-2276.848	-1514.861
7	↑↓↓↑	AFM6	-2129.590	-2276.848	-1514.861
8	↑↓↓↑	AFM7	-2129.577	-2276.840	-1514.861

B.2: Mean field calculation of Curie temperature

Physical constants: 1 Ry = 13.605 eV (let $\epsilon = 13.605$)$k_B = 8.617 \times 10^{-5} eV \cdot K^{-1}$

First, we obtain the FM and AFM energies from DFT in eV per formula unit [eV/f.u.]:

$$E_{FM} = E_0 + E_{ex} = (-2129.61082946/4) \times \epsilon \tag{6.1}$$

$$E_{AFM} = E_0 + E_{ex} = (-2129.59000762/4) \times \epsilon \tag{6.2}$$

$$\tag{6.3}$$

Then,

$$\Delta E = E_{FM} - E_{AFM}, \tag{6.4}$$

such that $E_{ex} = 1/2(E_{FM} - E_{AFM})$ =-0.03541 eV , while

$$E_{ex} = -2zJS^2 \tag{6.5}$$

where we define z and S as 1 and 2, respectively. Therefore, we solve for J as

$$J = -\frac{E_{ex}}{2zS^2}. \tag{6.6}$$

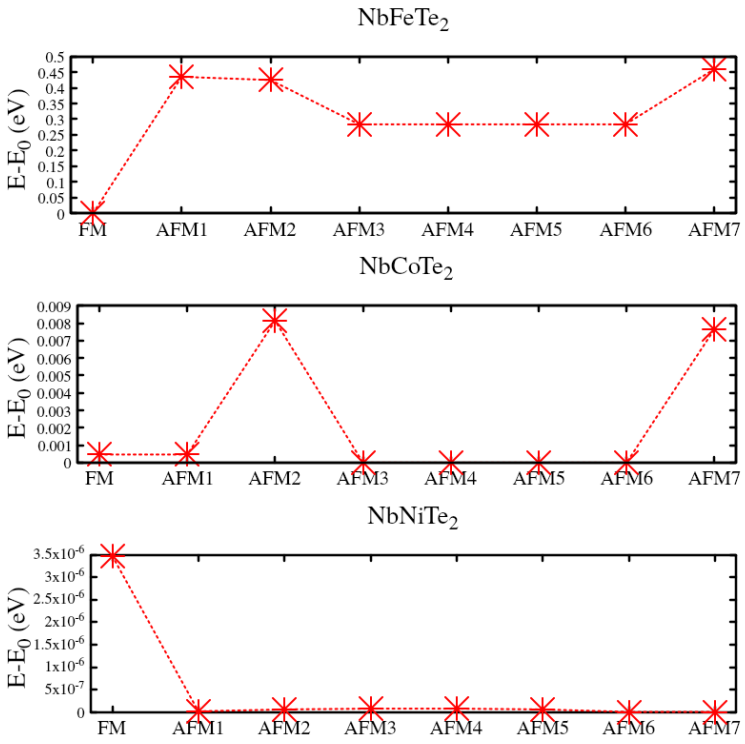

Figure 6.3: Total energy in eV per formula unit (f.u.) as a function of the magnetic configuration of the $NbMTe_2$ compunds. The iron, cobalt and nickel compounds are shown in (a), (b), and (c) respectively. The magnetic configurations are labeled according to Table 5.1.

Once we have J, ($J = 0.0044$ eV), we simply compute T_C via the equation

$$T_C = \frac{2zJ[S(S+1)]}{3k_B} \tag{6.7}$$

yielding a value of 205 K. The raw computations can be found in the python notebook uploaded to the author's github repository in [**46**].

Bibliography

[1] P.A.M. Dirac, "Quantum Mechanics of Many-electron Systems" , *Proc. R. Soc. Lond. A*, 1929, **123** (92) 714-733.

[2] F. Jellinek, "Transition Metal Chalcogenides: relationship between chemical composition, crystal structure and physical properties", *Reactivity of Solids*, 1988, **5**, 323-339.

[3] A.L. Allred, *Journal of Inorganic and Nuclear Chemistry*, 1961, 17 (3-4), 215–221.

[4] A.P. Tiwari, *et al*, "Layered Ternary and Quaternary Transition Metal Chalcogenide Based Catalysts for Water Splitting", *Catalysts*, 2018, **8**, (551) 1-29.

[5] A.Y. Lu, *et al*, "Janus monolayers of transition metal dichalcogenides", *Nature Nanotechnology*, 2017, **12**, 744-749.

[6] J. Wang, *et al*, "Intriguing electronic and optical properties of two-dimensional Janus transition metal dichalcogenides", *Phys. Chem. Chem. Phys*, 2018, **20**(27), 18571-18578.

[7] F.Zhan, *et al*, "Low-Temperature Synthesis of Cuboid Silver Tetrathiotungstate (A_2WS_4) as Electrocatalyst for Hydrogen Evolution Reaction", *Inorg. Chem.*, 2018, **57**(10), 5791-5800.

[8] J.M.D. Coey , *Magnetism and Magnetic Materials*, 2009, Cambridge University Press, Cambridge, UK.

[9] N.A. Spaldin, *Magnetic Materials: Fundamentals and Applications*, 2011, Cambridge University Press, Cambdridge, UK.

[10] A. Szabo & N.S. Ostlund, "Chapter 2: Many Electron Wave Functions as Operators", in *Modern Quantum Chemistry; introduction to advanced electronic structure theory*, 1989, Dover Publications Inc., Mineola, NY, pp. 3-55.

[11] W. Koch & M.C. Holthausen, *A Chemist's Guide to Density Functional Theory*, 2001, Wiley-VCH,Weinheim, Germany.

[12] D. Sholl & J. Steckel, *Density Functional Theory: a practical introduction*, 2009, John Wiley & Sons, New York, NY.

[13] D.J. Singh & L. Nordstrom, "Chapter 2: Density Functional Theory and Methods", in *Planewaves, Pseudopotentials and the LAPW Method*, 2005, Spinger US, New York, NY, pp. 5-20.

[14] P. Hohenberg and W. Kohn "Inhomogeneous Electron Gas", *Physical Review*, **136**(3B), B864-B871, (1964).

[15] W. Kohn and L.J. Sham., "Self-Consistent Equations Including Exchange and Correlation Effects", *Physical Review*, **140**(4A), A1133–A1138, (1965).

[16] D.J. Singh & L. Nordstrom, "Chapter 3: Planewave Pseudopotential Methods", in *Planewaves, Pseudopotentials and the LAPW Method*, 2005, Spinger US, New York, NY, pp. 21-36.

[17] C. Kittel, "Chapter 7: Energy Bands", in *Introduction to Solid State Physics, Eigth Ed.*, 2005, John Wiley & Sons, New York, NY, pp. 161-182.

[18] D.R. Hamann, M. Sclüter, C. Chiang, "Norm-Conserving Pseudopotentials", *Physical Review Letters*, **43** (20), 1494-1497, (1979).

[19] D. Vanderbilt, "Soft self-consistent pseudopotentials in a generalized eigenvalue formalism", Physical Review B, **41** (11), 7892–7895, (1990).

[20] Peter Schwerdtfeger, "Chapter 10: Relativistic Density Functional Theory", in *Relativistic Electronic Structure Theory: Part 1. Fundamentals*, 2002, ELSEVIER Science, Amsterdam, The Netherlands, pp. 523-622.

[21] G., Theurich, and N.A. Hill, N. A. "Self-consistent treatment of spin-orbit coupling in solids using relativistic fully separable *ab initio* pseudopotentials". *Physical Review B*, **64**(7), (2001).

[22] Z. Guo, F. Sun, and W. Yuan, "Chemical intercalations in layered transition metal chalcogenides:Syntheses, structures, and related properties, *Crystal Growth & Deisgn*, **17**, 2238 (2017).

[23] J. Rouxel, "Alkali metal intercalation compounds of transtition metal chalcogenides: TX_2, TX_3 and TX_4 chalcogenides", *Intercalated Layered Materials*, edited by F Lévy (Springer Netherlands, Dordrecht, 1979). pp. 201-250.

[24] D.W. Murphy, S.A. Sunshine, and S.M. Zahurak, "Preparation methods for alkali metal intercalation compounds of oxides and chalcogenides" *Chemical Physics of Intercalation*, edited by A.P. Legrendand and S. Floandrois (Springer US, Boston, MA, 1987) pp. 173-179

[25] C.D. Malliakas, D.Y. Chung, H. Claus, and M.G. Kanatzidis, "Superconductivity in the narrow-gap semiconductor $RbBi_{11/3}Te_6$", *J. Amer. Chem. Soc.*, **138,** 14694 (2016).

[26] H. CHen, H. Claus, J.K. Bao, C.C. Stoumpos, D.Y. Chung, W.K. Kwok, and M.G. Kanatzidis, "Superconductivity and structural conversion with na and K doping of the narrow-gap semiconductor $CsBi_4Te_6$, *Chem. Mater.* **30**, 5293 (2018).

[27] M. Sturza, C.D. Malliakas, D.E. Burgaris, F.Han, D.Y. Chung, and M.G. Kanatzidis, "$NaCu_6Se_4$: A layered compound with mixed valency and metallic properties. *Inorg. Chem.*, **53**, 1219 (2014).

[28] M. Sturza, D.E. Burgaris, C.D. Malliakas, F. Han, D.Y. Chung and M.G. Kanatzidis, "Mixed-valent $NaCu_4Se_3$: A two-dimensional metal, *Inorg. Chem.*, **55, 4884 (2016).**

[29] H. Chen, J.N.B. Rodrigues, A.J.E. Rettie, T.B. Song, D.G. Chica, X.Su, J.K. Bao, D.Y. Chung, W.K. Kwok, L.K. Wagner and M.G. Kanatzidis, "High hole mobility and nonsaturating giant magnetoresistance in the nrew 2D metal $NaCu_4Se_4$ synthesized by a unique pathway, *J. Amer. Chem. Soc.*, **141**, 635 (2019).

[30] Z. Xia, H. Fang, X. Zhang, m.S. Molokeev, R. Gautier, Q. Yan, S.H. Wei, and K.R. Poeppelmeier, "$CsCu_5Se_3$: A copper-rich ternary chalcogenide with nearly direct bandgap for photovoltaic application", *Chem. Mater.*, **30**, 1121 (2018).

[31] N. Ma, Y.Y. Li, L. Chen, L.M. Wu, $\alpha - CsCu_5Se_3$: Discovery of a low-cost bulk selenide with high thermoelectric performance, *J. Amer. Chem. Soc.* **142**, 5293 (2020).

[32] A. Stoliaroff, S. Jobic, and C. Latouche, "An *ab-initio* perspective on the key defects of $CsCuSe_3$, a possible material for optoelectronic applications," *J. Phys. Chem. C*, **124**, 4363 (2020).

[33] A. Stoliaroff, S. Jobic, and C. Latouche, "An *ab-initio* perspective on the key defects of $CsCuSe_3$, a possible material for optoelectronic applications," *J. Phys. Chem. C*, **124**, 4363 (2020).

[34] M. Buffiere, D.S. Dhwale, and F. El-Mellouhi, "Chalcogenide materials and derivatves for photovoltaic applications", *Energy Technology*, **7**, 1900819 (2019).

[35] K.Kuhar, A. Crovetto, M. Pandey, K.S. Thygesen, B.Seger, P.C.K. Vesborg, O.Hansen. I. Chorkendorff, and K.W. Jacobsen, "Sulfide pervovskites for solar energy conversion applications: computational screening and synthesis of the selected compund $LaYS_3$", *Energy Environ. Sci.*, **10**, 129 (2016).

[36] S. Perera, H. Hui, C. Zhao, H. Xue, F. Sun, C. Deng, N. Gross, C. Milleville, . Xu, D.F. Watson, B. Weinsetein, Y.Y. Sun, S. Zhang, and H. Zheng, "Chalcogenide perovskites - an emerging class of ionic semiconductors", *Nano Energy*, **22**, 129 (2016).

[37] S. Niu, H. Huyan, Y. Liu, M. Yeung, K. Ye, L. Blankemeier, T. Orvis, D. Sarkar, D.J. Singh, R. Kapadia, and J. Ravichandran, "Bandgap control via structural and chemical tuning of transition metal perovskite chalcogenides" *Advanced Materials*, **29**, 1604733, (2016).

[38] Q. Sun, H. Chen, and W.J. Yin, "Do chalcogenide double perovskites work as solar cell absorbers: a first principles study", *Chem. Mater.* **31**, 244 (2019).

[39] A. Swarnkar, W.J. Mir, R. CHakraborty, M.J. gradeeswararao, T. Sheikh, and A. Nag, "Are chalcogenide perovskites an emerging class of semiconductors for optoelectronic properties and solar cell?", *Chem. Mater.*, **31**, 565 (2019).

[40] National Center for Biotechnology Information. PubChem database. Sodium Molybdate, CID = 61424, URL: https://pubchem.ncbi.nlm.nih.gov/compound/Sodium-molybdate, accessed: 2020-19-04.

[41] National Center for Biotechnology Information. PubChem database. Dicaesium Tungstem Tetrasulfide, CID = 139072572, URL: https://pubchem.ncbi.nlm.nih.gov/compound/139072572, accessed: 2020-19-04.

[42] G. Hautier, C. Fischer, V. Erlacher, A. Jain, and G. Ceder, "Data mined ionic substitutions for the discovery of new compounds", *Inorg. Chem.*, **50**, 656 (2011).

[43] G. Hautier, C. Fischer, V. Erlacher, A. Jain, and G. Ceder, "Data mined ionic substitutions for the discovery of new compounds", *Inorg. Chem.*, **50**, 656 (2011).

[44] A. Narayan, A. Bhutani, S. Rubeck, J.N. Eckstein, D.P. Shoemaker and L.K. Wagner, "Computational and experimental investigation for new transition metal selenides and sulfides: The importance of experimental verification for stability" *Phys Rev B*, **94**, 045105, (2016).

[45] A.Jain, S. P. Ong, G. Hautier, W. Chen, W.D. Richards, S. Dacek, S. Cholia, D. Grunter, D. Skinner, G. Ceder and K.A. Persson, "The Materials Project: A materials genome approach to accelerating materials innovation" *APL Materials*, **1**, 011002, (2013).

[46] Repository: Na_2MoSe_4 crystal structures and data, URL: https://github.com/etiennepalos/Na2MoSe4, accessed: 200-19-04.

[47] P.Gianozzi, S. Baroni, N. Bonini, M. Calandra, R. Car,C. Cavazzoni, D. Ceresoli, G. L. Chiarotti, M. Cococ-cioni, I. Dabo, A. D. Corso, S. de Gironcoli, S. Fab-ris, G. Fratesi, R. Gebauer, U. Gerstmann, C. Gougous-sis, A. Kokalj, M. Lazzer, L. Martin-Samos, N. Marzari,F. Mauri, R. Mazzarello, S. Paolini, A. Pasquarello,L. Paulatto, C. Sbraccia, S. Scandolo, G. Sclauzero, A. P.Seitsonen, A. Smogunov, P. Umari, and R. M. Wentzcov-itch, "Quantum ESPRESSO: A modular and open-source software project for quantum simulations of materials", *J. Phys. Cond. Mat*, **21**, 395502 (2009).

[48] P.Gianozzi, S. Baroni, N. Bonini, M. Calandra, R. Car,C. Cavazzoni, D. Ceresoli, G. L. Chiarotti, M. Cococ-cioni, I. Dabo, A. D. Corso, S. de Gironcoli, S. Fab-ris, G. Fratesi, R. Gebauer, U. Gerstmann, C. Gougous-sis, A. Kokalj, M. Lazzer, L. Martin-Samos, N. Marzari,F. Mauri, R. Mazzarello, S. Paolini, A. Pasquarello,L. Paulatto, C. Sbraccia, S. Scandolo, G. Sclauzero, A. P.Seitsonen, A. Smogunov, P. Umari, and R. M. Wentzcov-itch, "Advanced capabilities for materials modelling with Quantum ESRPESSO", *J. Phys. Cond. Mat*, **29**, 656 (2017).

[49] J. Perdew, A. Ruzsinsky, G. Csonka, O.A. Vydov, G.E. Scuseria, L.A. Constantin, X. Zhou, and K. Burke, "Restoring the density-gradient expansion for exchange in solids and surfaces" , *Physical Review Letters*, **100**, 136406, (2009).

[50] G.D.Nguimdoand and D.P. Jourbert, "A density functional (PBE, PBEsol, HSE06) stufy of the structural, electronic and optical properties of the ternary compounds $AgAlX_2$ (X =S,Se,Te)" *European Physical Journal B*, **88**, 136406, (2014).

[51] M. Benam, N. Abdoshahi, and M.M. Sarmazdeh, "Ab-initio study of the effect of pressure on the structural and electronic properties of cubic $LaAlO_3$ by density functional theory using GGA, LDA and PBEsol exchange correlation potentials" *Physica B*, **446**,32 136406, (2014).

[52] M.D.L. Pierre, R. Orlando, L. Maschio, K. Doll,P. Uliengo, and R. Dovesi, "Performance of six functionals (LDA, PBE, PBEsol, B3LYP, PBE0, and WC1LYP) in the simulation of vibrational and dielectric properties of crystalline compounds. the case of forsterite mg2sio4" *J. Comput. Chem*, **32**, 1775-1784, (2011).

[53] A. Dal Corso, "Pseudopotentials periodic table: from *H* to *Pu*" *Comput. Mater. Sci.*, **95**, 337 (2014).

[54] S. Grimme, "Semiempirical GGA-type density functional constucted with a long-range dispersion correction" *J. Comput. Chem.*, **27**, 1787 (2006).

[55] H.J. Monkhorst and J.D. Pack, "Special points for brillouin-zone integrations" *Phys. Rev. B.*, **13**, 5188 (1976).

[56] F. Tran and P. Blaha, "Accurate band gaps of semiconductors and insulators with a semilocal exchange-correlation potential" *Phys. Rev. Lett.*, **102**, 226401 (2009).

[57] D. Waroquiers, A. Lherbier, A. Miglio, M. Stankovski, S. Poncé, M.J. Oliveira, M. Giantomassi, G.M. Rignanense, and X. Gonze, "Band widths and gaps from the Tran-Blaha functional: Comparison with many-body perturbation theory", *Phys. Rev. B.* **87**, 075121 (2013).

[58] P. Blaha, K. Schwarz, F. Tran, R. Laskowski, G.K.H. Madsen, and L.D. Marks, "Wien2K: an APW+lo program for calculating the properties of solids", *J. Chem. Phys* **152**, 074101 (2020).

[59] M.G. Goestenand, and R. Hoffmann, "Mirrors of bonding in metal halide perovskites", *J. Amer. Chem. Soc.*, **140**, 12996 (2018).

[60] M.A. Reynolds, and S.N. Milanm, "Process for producing a copper tiometallate or a selenometallate material", *US Patent*, 8940268, (2015).

[61] C.C. Fischer, K.J. Tibbetts, D. Morgan, and G. Ceder, "Predicting crystal structure by merging data mining with quantum mechanics", *Nature Materials* **5**, 641 (2006).

[62] G. Hautier, C.C. Fischer, A. Jain, T. Mueller, and G. Ceder, "Finding nature's missing ternary oxidecompounds using machine learning and density func-tional theory", *Chem. Mater.*, **22**, 3762 (2010).

[63] S. Atahan-Evrenkand and A. Aspuru-Guzik, "Prediction andcalculation of crystal structures", in Topics in "Current Chemistry", pp. 345 (2014).

[64] C. Raymond, R. Dorhout, and S. Miller, "Crystal structure of dicaesium tetramolybdate, Ce_2MoS_4", *Zeitschrift fut Kristallographie*, **210**, 775 (1995)

[65] C. Raymond, R. Dorhout, and S. Miller, "Crystal structure of dicaesium tetramolybdate, Ce_2MoS_4", *Zeitschrift fut Kristallographie*, **210**, 775 (1995)

[66] J. Ellermeier, C. Nather, and W. Bensch, Rb_2MoMoS_4, *Zeischrift fur Kristallographie*, **216**, 484, (2001).

[67] D. Rohnert, C. Nather, and W. Bensch, K_2MoWS_4, *Zeischrift fur Kristallographie*, **53**, 165, (1997).

[68] A. Muller and W. Sievert, "Rontgenographische unter-suchungen und strukturchemie von chalkogenomolybdaten und - wolframaten", *Zeitschrify fur Anorganische und Allegemie Chemie*, **403**, 251 (1974).

[69] B. R. Srinivasan, C. Näther, A. R. Naik, and W. Bensch, "Bis(methylammonium) tetrathiomolybdate(VI)", *Acta Crystallographica Section E*, **62**, 31635 (2006).

[70] W. Setyawan, and S. Curtarolo, "High-throughput elec-tronic band structure calculations: Challenges and tools", *Comput. Mater. Sci.*, **49**, 299 (2010).

[71] Y. Hinuma, G. Pizzi, Y. Kumagai, F. Oba, and I. Tanaka, "Band structure diagram paths based on crystallography", *Comput. Mater. Sci.*, **128**, 140 (2017).

[72] R. G. Burns, *Mineralogical Applications of Crystal Field Theory, Second Ed.* Cambridge University Press, (2005), pp. 22-30.

[73] A. K., S. J. H. Montoya, J. M. Gregoire, and K. A. Pers-son, "Robust and synthesizable photocatalysts for CO_2-reduction: a data-driven materials discovery", *Nature Communications*, **443**, 1 (2019).

[74] J. A. Camargo-Martínez and R. Baquero, "Performance ofthe modified Becke-Johnson potential for semiconductors" *Phys. Rev. B.*, **86**, 195106 (2012).

[75] H. Jiang, "Band gaps from the Tran-Blaha modified Becke-Johnson approach: A systematic investigation" *J. Chem. Phys.*, **138**, 134115 (2013).

[76] W. Feng, D. Xiao, Y. Zhang, and Y. Yao, "Half-heusler topological insulators: A first-principles study with the Tran-Blaha modified Becke-Johnson density functional", *Phys. Rev. B.*, **82**, 235121 (2010).

[77] H. Dixit, R. Saniz, S. Cotte, D. Lamonen, and B. Partoens, "Electronic Structure of transparent oxides with the Tran-Blaha modified Becke-Johnson potential", *J. Phys. Cond. Mat.* **24**, 205503 (2012).

[78] R.A. Jishi, O.B. Ta, and A.A. Sharif, "Modeling of lead halide perovskites for photovoltaic applications ", *J. Phys. Chem. C.* **118**, 28344 (2014).

[79] B. Traoré, G. Bouder, W. Lafargue-Dit-Hauret, X. Roc-quefelte, C. Katan, F. Tran, and M. Kepenekian, "Efficient and accurate calculation of band gaps of halide perovskites with the Tran-Blaha modified Becke-Johnson potential", *Phys. Rev. B.*, **99**, 03139 (2019).

[80] F. Tran and P. Blaha, "Importance of the kinetic energy density for band gap calculations in solids with density functional theory", *J. Phys. Chem. A.* **121**, 3318 (2017).

[81] F. Tran, J. Doumont, L. Kalantari, A. Huran, M. L.Marques, and P. Blaha, "Semilocal exchange-correlationpotentials for solid-state calculations: Current status andfuture directions", *J. Appl. Phys.* **126**, 110902 (2019).

[82] E. Palos, A. Reyes-Serrato, G. Alonso and J. Guerrero-Sánchez, "Modeling the Ternary Chalcogenide Na_2MoSe_4 from First-Principles". *J. Phys. Condens. Mat.* DOI: https://doi.org/10.1088/1361-648X/abaf91

[83] M. van Setten, M. Giantomassi, E. Bousquet, M. Ver-straete, D. Hamann, X. Gonze, and G.-M. Rignanese, "The PseudoDojo: Training and grading a 85 element optimized norm-conserving pseudopotential table", *Computer Physics Communications* **226**, 39 (2018).

[84] D. R. Hamann, "Optimized norm-conserving Vanderbilt pseudopotentials", *Phys. Rev. B* **88**, 085117 (2013).

[85] K. Bushick, K. Mengle, N. Sanders, and E. Kioupakis, "Band structure and carrier effective masses of boron arsenide: Effects of quastiparticle and spin-orbit coupling corrections", *Appl. Phys. Lett., **114**, 022101, (2019).*

[86] I. Zutic, J. Fabian, and S. Das Sarma "Spintronics: Fundamentals and Applications", *Rev. Mod. Phys, **76**, 323, (2004).*

[87] S. Baderand S. Parkin, "Spintronics", *Annual Review of Condensed Matter Physics* **1**, 71, (2010).

[88] A. K. A. Brataasand H. Ohno, "Current-induced torques in magnetic materials" *Nature Materials*, **11**, 372, (2012).

[89] C. Gong and X. Zhang, "Two-dimensional magnetic crystals and emergent heterostructure devices", *Science*, **363**, (2019).

[90] K. S. Novoselov, A. K. Geim, S. V. Morozov, D. Jiang,Y. Zhang, S. V. Dubonos, I. V. Grigorieva, and A. A.Firsov, "Electric field effect in atomically thin carbon films", *Science* **306**, 666 (2004).

[91] H. Liu, A.T. Neal, Z.Zhu, Z. Luo, X. Xu, D. Tomnek, and P. D. Ye, "Phosphorene: An unexplored 2D semiconductor with a high hole mobility", *ACS Nano* **8**, 4033 (2014).

[92] S. Cahangirov, M. Topsakal, E. Aktürk, H. Şahin, and S. Ciraci, "Two-and one-dimensional honeycomb structures of silicon and germanium." *Phys. Rev. Lett.*, **102**, 236804, (2009).

[93] P. Vogt, P. De Padova, C. Quaresima, J. Avila, E. Frantzeskakis, M.C. Asensio, A. Resta, B. Ealet, and G. Le Lay, "Silicene: Compelling experimental evidence for graphene-like two-dimensional silicon", *Phys. Rev. Lett.*, **108** 155501 (2012).

[94] M. Pumeraand Z. Sofer, 2d monoelemental arsenene, an-timonene, and bismuthene: Beyond black phosphorus,Advanced Materials29, 1605299 (2017).

[95] F. Matusalem, M. Marques, L. K. Teles, and F. Bechst-edt, Stability and electronic structure of two-dimensionalallotropes of group-iv materials, Phys. Rev. B92, 045436(2015).

[96] M. E. D avila, L. Xian, S. Cahangirov, A. Rubio, and G. L. Lay, Germanene: a novel two-dimensional germa-nium allotrope akin to graphene and silicene, New Journal of Physics16, 095002 (2014).

[97] A. J. Mannix, B. Kiraly, M. C. Hersam, and N. P.Guisinger, Synthesis and chemistry of elemental 2d ma-terials, Nature Reviews Chemistry16, 095002 (2017).

[98] O. Y. S. Manzeli, D. Ovchinnikovand A. Kis, 2D transition metal dichalcogenides, Nature Reviews Materials2,17033 (2017).

[99] T. D. Thanh, N. D. Chuong, H. V. Hien, T. Kshetri, L. H.Tuan, N. H. Kim, and J. H. Lee, Recent advances in two-dimensional transition metal dichalcogenides-graphene heterostructured materials for electrochemical applications, Progress in Materials Science96, 51 (2018)

[100] Z. Hu, Z. Wu, C. Han, J. He, Z. Ni, and W. Chen, Two-dimensional transition metal dichalcogenides: interfaceand defect engineering, Chem. Soc. Rev47, 3100 (2018).

[101] W. Choi, N. Choudhary, G. H. Han, J. Park, D. Ak-inwande, and Y. H. Lee, Recent development of two-dimensional transition metal dichalcogenides and theirapplications, *Materials Today* **96**, 116 (2017).

[102] Y.-T. Hsu, A. Vaezi, M. H. Fischer, and E.-A. Kim,Topological superconductivity in monolayer transitionmetal dichalcogenides, *Nature Communications*, **8**, 14985(2017).

[103] X. Zhang, T. Luo, X. Hu, J. Guo, G. Lin, Y. Li,Y. Liu, X. Li, J. Ge, Y. Xing, Z. Zhu, P. Gao,L. Sun, and J. Wang, Superconductivity and fermi surface anisotropy in transition metal dichalcogenide NbTe2, *Chinese Physics Letters*, **36**, 057402 (2019).

[104] L. Kou, Y. Ma, Z. Sun, T. Heine, and C. Chen,Two-dimensional topological insulators:Progress and prospects, *The Journal of Physical Chemistry Letters* **8**, 1905 (2017), pMID: 28394616,https://doi.org/10.1021/acs.jpclett.7b00222

[105] S. M. Youngand C. L. Kane, Dirac semimetals in twodimensions, Phys. Rev. Lett.115, 126803 (2015)

[106] N. Samarth, Magnetism in flatland, Nature546, 216(2017).

[107] B. Huang, G. Clark, E. Navarro-Moratalla, D. R. Klein,R. Cheng, K. L. Seyler, D. Zhong, E. Schmidgall, M. A.McGuire, D. H. Cobden, W. Yao, D. Xiao, P. Jarillo-Herrero, and X. Xu,

Layer-dependent ferromagnetism ina van der waals crystal down to the monolayer limit. *Nature* **546**, pages270–273, (2017).

[108] C. Gong, L. Li, Z. Li, H. Ji, A. Stern, Y. Xia, T. Cao,W. Bao, C. Wang, Y. Wang, Z. Qiu, R. Cava, S. G.Louie, J. Xia, and X. Zhang, Discovery of intrinsic fer-romagnetism in two-dimensional van der waals crystals,Nature546, 265 (2017).

[109] M. Bonilla, S. Kolekar, Y. Ma, H. C. Diaz, V. Kalappat-til, R. Das, T. Eggers, H. R. Gutierrez, M.-H. Phan, andM. Batzill, Strong room-temperature ferromagnetism invse2 monolayers on van der waals substrates, Nature546,289 (2018).

[110] X. Liand J. Yang, Crxte3 (x = si, ge) nanosheets: twodimensional intrinsic ferromagnetic semiconductors, J. Mater. Chem. C. 2, 7071 (2014).

[111] H. L. Zhuang, Y. Xie, P. R. C. Kent, and P. Ganesh,Computational discovery of ferromagnetic semiconduct-ing single-layer crsnte3, Phys. Rev. B92, 035407 (2015).

[112] H.-J. Deiseroth, K. Aleksandrov, C. Reiner, L. Kienle,and R. K. Kremer, Fe_3GeTe_2 and Ni_3GeTe_2 two new layered transition-metal compounds: Crystal structures, HR-TEM investigations, and magnetic and electrical properties, *European Journal of Inorganic Chemistry* (2006),1561.

[113] Zhuang, H. L., Kent, P. R. C., Hennig, R. G. Strong anisotropy and magnetostriction in the two-dimensional Stoner ferromagnet Fe3GeTe2. Physical Review B, 93(13). (2016).

[114] Deng, Y., Yu, Y., Song, Y., Zhang, J., Wang, N. Z., Sun, Z., ... Zhang, Y. Gate-tunable room-temperature ferromagnetism in two-dimensional Fe3GeTe2. Nature. (2018).

[115] Q.Li, M.Yang, C.Gong, R. V. Chopdekar, A.T.NDi-aye, J.Turner, G. Chen,A.Scholl, P. Shafer, E. Aren-holz, A.K. Schmid, S. Wang, K. Liu, N. Gao, A. S.Admasu, S.-W. Cheong, C. Hwang, J. Li, F. Wang,X. Zhang, and Z. Qiu, "Patterning-induced ferromag-netism of Fe3GeTe2 van der waals materials beyond roomtemperature", *Nano Letters* **18**, 5974 , (2018).

[116] M. Gibertini,M. Koperski, A. Morpurgo,and K. Novoselov, "Magnetic 2D materials and heterostructures", *Nature Nanotechnology* **14**, (2019).

[117] Wilson, J. A., Di Salvo, F. J., Mahajan, S. (1975). Charge-density waves and superlattices in the metallic layered transition metal dichalcogenides. Advances in Physics, 24(2), 117–201. doi:10.1080/00018737500101391

[118] Li, J., Badding, M. E., DiSalvo, F. J. (1992). Synthesis and structure of Nb3SiTe6, a new layered ternary niobium telluride compound. Journal of Alloys and Compounds, 184(2), 257–263. doi:10.1016/0925-8388(92)90499-y

[119] Hu, J., Liu, X., Yue, C. L., Liu, J. Y., Zhu, H. W., He, J. B., ... Natelson, D. (2015). Enhanced electron coherence in atomically thin Nb3SiTe 6 . Nature Physics, 11(6), 471–476.

[120] Li, Jing, Michael E. Badding, and F. J. DiSalvo. "New layered ternary niobium tellurides: synthesis, structure, and properties of niobium metal telluride, NbMTe2 (M= iron, cobalt)." Inorganic Chemistry 31.6 (1992): 1050-1054.

[121] Bai, Wei, et al. "Intrinsic Negative Magnetoresistance in Van Der Waals FeNbTe2 Single Crystals." Advanced Materials 31.18 (2019): 1900246.

[122] Wang, L.-L., Jo, N. H., Wu, Y., Wu, Q., Kaminski, A., Canfield, P. C., Johnson, D. D. (2017). Phonon-induced topological transition to a type-II Weyl semimetal. Physical Review B, 95(16).

[123] Neu, Jennifer, et al. "Orthorhombic to monoclinic phase transition in NbNiTe 2." Physical Review B 100.14 (2019): 144102.

[124] Shannon, R. D. "Revised ionic radii and systematic studies of interatomic distances in halides and chalcogenides", Acta Cryst., A32, 751-767. (1976).

[125] Pakhira, Srimanta, Kevin P. Lucht, and Jose L. Mendoza-Cortes. "Dirac cone in two dimensional bilayer graphene by intercalation with V, Nb, and Ta transition metals." The Journal of chemical physics 148.6 (2018)

[126] Pakhira, Srimanta, and Jose L. Mendoza-Cortes. "Tuning the Dirac cone of bilayer and bulk structure graphene by intercalating first row transition metals using first-principles calculations." The Journal of Physical Chemistry C 122.9 (2018): 4768-4782.

[127] Pablo-Pedro, Ricardo, et al. "Understanding disorder in 2D materials: the case of carbon doping of Silicene." *Nano Letters In Press* (2020).

[128] Kan, M., Adhikari, S., Sun, Q.(2014). Ferromagnetism in MnX2 (X = S, Se) monolayers. Physical Chemistry Chemical Physics,16(10), 4990.

[129] Chen, B., Yang, J., Wang, H., Imai, M., Ohta, H., Michioka, C., ... Fang, M. (2013). Magnetic Properties of Layered Itinerant Electron Ferromagnet Fe3GeTe2. Journal of the Physical Society of Japan, 82(12), 124711. doi:10.7566/jpsj.82.124711